The paleoenvironmental significance of evaporite–dolomite associations in two Spanish saline lakes

Willem Jan Blom

Master's Thesis Earth Sciences

Utrecht University

Faculty of Geosciences

Department of Earth Sciences

Master programme: Earth, Life and Climate

Supervisors:

Dr. Mariette Wolthers (Universiteit Utrecht)

Dr. Mónica Sanchez Román (Vrije Universiteit Amsterdam)

Abstract

Dolomite is a mineral which is abundant in the geological record, but its origin is poorly understood. At present, dolomite is mostly formed in saline and hypersaline environments, such as salt lakes, in which it is closely connected to evaporite minerals. This makes the relationship between dolomite formation and evaporite precipitation an important topic for understanding the conditions under which dolomite can form.

In this thesis, the evaporites in the sediment cores of two Spanish saline lakes (Laguna de Salinas (Alicante) and Laguna de Fuente de Piedra) are studied to understand the paleoenvironmental significance of evaporite layers. Petrographic, scanning electron microscopy and energy dispersive X-ray spectroscopy (SEM-EDS), inductively coupled plasma optical emission spectroscopy (ICP-OES), X-ray fluorescence (XRF) and sulphate and oxygen isotope analyses were performed and age models of both cores were constructed.

It was found that evaporites were formed under dry, evaporative conditions, which were formed when the oxygen concentration in the lakes was relatively low. This indicates that the oxygen production by photosynthetic bacteria was reduced. In Laguna de Salinas, these evaporative conditions remained stable for multiple years, during which selenite layers were formed, whereas evaporite laminae in Laguna de Fuente de Piedra alternate with dolomite laminae in annual couplets. A correlation between two sediment cores, which contain sediment from the last glacial period and the Holocene, and paleoclimatic reconstructions show that evaporites were mostly formed during cold periods.

Contents

1. Introduction

1.1. Introduction

Dolomite is a common mineral in the stratigraphic record but is almost absent in modern sedimentary environments. Even under conditions of extreme supersaturation with respect to dolomite in laboratory experiments, dolomite fails to precipitate (Land, 1998). This discrepancy is known as the “dolomite problem” and remains unsolved for more than 200 years.

One of the potential solutions to the dolomite problem is the precipitation of dolomite by microbial mediation (Vasconcelos & McKenzie, 1997). Several types of microorganisms are able to function as a catalyst for the precipitation of dolomite. These organisms are primarily found in saline and hypersaline environments, such as (hyper)saline lagoons and lakes. In these environments, dolomite is formed in close connection with evaporite minerals, which form as the result of supersaturation due to evaporation.

In order to understand the formation of dolomite by means of microbial mediation, it is necessary to understand the environmental conditions under which dolomite formation occurs, and also under what conditions dolomite formation is interrupted by evaporite precipitation. The latter topic has not been the subject of previous studies which try to elucidate the origin of microbially mediated dolomite. It is therefore the aim of this thesis to answer the question what the paleoenvironmental significance is of evaporite-dolomite associations in saline lakes. It will be investigated under what conditions evaporite layers within dolomite sediment were formed and how this relates to the conditions under which dolomite was formed.

For this, petrographic and geochemical analyses have been performed on the evaporite layers in two sediment cores. These evaporite layers are separated by dolomitic mud and

other carbonate sediment. The cores come from two Spanish salt lakes, Laguna de Salinas (Alicante) and Laguna de Fuente de Piedra. The similarities and differences between the evaporite-dolomite associations of these two lakes help to distinguish between the general characteristics of these associations and their specific actualizations.

In the remainder of this chapter, the dolomite problem will be further introduced and a general overview of the characteristics of lacustrine evaporite deposits will be given. The other chapters will discuss the methods, results, discussion and conclusion of the research that was performed for the writing of this thesis.

1.2. Background

1.2.1. The dolomite problem

Dolomite

Dolomite is the name for a group of rhombohedral magnesium carbonate minerals that are similar to the respect that they contain approximately equal amounts of calcium and magnesium (Warren, 2000). The chemical formula is therefore often expressed as $CaMg(CO_3)_2$, but the composition of dolomite can range from $Ca_{1.16}Mg_{0.94}(CO_3)_2$ to $Ca_{0.96}Mg_{1.04}(CO_3)_2$ (Warren, 2000). The mineral is similar to calcite ($CaCO_3$), except that it consists of alternating ordered layers of Ca^{2+} and Mg^{2+}.

The dolomite problem and its history

In 1957, Rhodes W. Fairbridge published a paper titled “The dolomite question” in which he poses two problems that should be raised with regards to the presence of dolomite in the sedimentary record (Fairbridge, 1957). The first question is why no modern sediments on the sea floor consist of dolomite, despite the fact that many ancient dolomites are of marine

origin. The second question is how dolomite could have been formed under normal sedimentary conditions, given the fact that is has proven to be very difficult to precipitate under these conditions. These two problems are together referred to as the "dolomite problem", which is still a major problem within sedimentology.

The origins of the dolomite problem go back to long before the classic paper of Fairbridge. The study of dolomite started at the end of the 18th century in the Southern Tyrol Alps by Giovanni Arduino and Déodat de Dolomieu, after whom the mineral was named (McKenzie & Vasconcelos, 2009). The original researchers, who were primarily concerned with the origin of the Dolomite mountains, suggested that the dolomite was the result of hydrothermal or volcanic alteration of limestone (McKenzie & Vasconcelos, 2009). Throughout the 19th century, several competing hypotheses were put forward, of which van Tuyl (1916) has given an overview.

Van Tuyl distinguishes three main categories of 'theories', each of which can be subdivided into multiple variants. The first category he names the "primary deposition theories", according to which dolomite has a primary origin, either through chemical precipitation, through organic production or as clastic sediments. The second category comprises the "alteration theories", according to which dolomite is a the product of diagenetic alteration of limestone, either under marine conditions or as the result of groundwater circulation. Another 'theory' within this category is the hypothesis that dolomite is a product of contact metamorphism. The third category comprises hypotheses that regard dolomite rocks as the result of leaching, when lime is taken into solution and dolomite is left behind as a residue.

By the time of van Tuyl (1916) both questions that comprise the dolomite problem had been noted, as experimental studies that tried to precipitate dolomite under normal pressure and temperature conditions had already been carried out in the 1850s by Gustav Bischof (Bischof, 1859, pp. 166-168) and others (Wang, 2021). From these experiments, it followed that carbonate could not precipitate with a 1:1 ratio of calcium and magnesium.

The 20th century saw two major additions to the discussion of the dolomite problem in the 19th century. First of all, Georgi Nadson managed to precipitate a small amount of dolomite in an experiment using sulphate-reducing bacteria (McKenzie & Vasconcelos, 2009). This was the beginning of microbiological experiments that demonstrated the possibility of dolomite precipitation under Earth surface conditions through microbial mediation, something which has gained considerable interest in the last decades of research into the dolomite problem (Li et al., 2021).

The second major discovery were several modern environments in which dolomite precipitation is currently occurring. These environments can be divided into sabkhas and tidal flats on the one hand, and (hyper)saline lakes on the other. Both types of environments and the formation of dolomite within them will be discussed in more detail below.

At present, the dolomite problem is still regarded as being unsolved. For example, Miao et al. (2023) call the genesis of sedimentary dolomite an "enigma", given the absence of large-scale dolomite formation in modern environments, and Wang (2021) notes that "there has never been a geological problem that has confused geologists for so long." Li et al. (2017) state that "there remains a long-running debate on whether most dolomite in the geological record formed during late burial diagenesis or syngenetically in the depositional environment." In other words, the first two categories of hypotheses presented by Van Tuyl (1916) as the result of the research in the 19th century are still discussed (Warren, 2000).

Dolomite in the sedimentary record

To understand the extent of the dolomite problem, it is necessary to review the presence of dolomite in the sedimentary record. Early calculations of dolomite abundance seemed to indicate that the percentage of dolomite in the total inventory of carbonate rocks increased with age during the Phanerozoic (Daly, 1909; Chilingar, 1956; Schmoker et al., 1985).

However, Given and Wilkinson (1987) argued that these earlier studies made several methodological mistakes. Their own reconstruction of dolomite abundance shows a strong correlation between dolomite abundance and global sea level, with peak abundances above 70 percent occurring during the Ordovician, Silurian and Late Cretaceous, whereas the abundance ranges between 10 and 20 percent for the Carboniferous, Permian and the entire Cenozoic.

Holland and Zimmerman (2000) in turn noted that the reconstruction of Given and Wilkinson was based on very limited data for some periods. When the points without statistical significance are removed, the same pattern emerges as in the earlier studies, in which there is a decline in dolomite abundance since at least 150 Ma. The weight percent of dolomite in carbonate rocks from the Proterozoic and Palaeozoic ranges between 40 and 75 percent, whereas the abundance of dolomite in Cenozoic carbonates drops below 10 percent. Holland and Zimmerman (2000) mention that the decline of dolomite during the Mesozoic and Cenozoic corresponds to several other changes that may serve as explanations, such as an increase of deep-sea carbonates which are less easily dolomitized and a change in ion exchange in silicates as a result of a declining CO_2 concentration, leading to the uptake of Mg^{2+} and the release of Ca^{2+}. If diagenesis is favoured as the explanation of the origin of dolomite, it may be argued that the decline in dolomite content is the result of the expiration of less time for diagenesis. However, Holland and Zimmerman (2000) deem this an unlikely explanation, as late-burial dolomites are limited in abundance and most dolomite have originated synsedimentary or early during burial.

More recently, Li et al. (2021) constructed a new dataset of dolomite abundance, taking the thickness of all dolomite beds with respect to the thickness of all carbonate beds as a measure of dolomite abundance. Their results show a more complex variation of dolomite abundance, ranging between 4 and 41 percent. The fluctuations show an inverse correlation with the diversity of marine benthic invertebrates. According to Li et al. (2021), this inverse

correlation can be explained by ocean anoxic events, during which the diversity of benthic animals declined and seafloor were dominated by microorganisms that facilitated the precipitation of dolomite.

Modern dolomite occurrences

Modern dolomite precipitation occurs in marine environments, such as sabkhas, mudflats and lagoons, as well as in (hyper)saline lakes (Warren, 2000). In sabkhas, dolomitization occurs in close connection with the precipitation of evaporite minerals (Warren, 1991). When seawater sinks into the sabkha, it evaporates, which leads to the precipitation of aragonite and then gypsum or anhydrite. The remaining water is enriched in Mg^{2+} relative to Ca^{2+}, as the latter ion is contained by the precipitated minerals. This Mg^{2+}-rich water then reacts with aragonite in the subsurface and leads to dolomitization. A second mechanism of dolomite formation in sabkha environments is the precipitation of dolomite within the extrapolymeric substances (EPS) of microbial mats (Bontognali et al., 2010). In this way, dolomite forms as a direct precipitate from seawater, instead of being an alteration of aragonite.

Other (hyper)saline water masses in which dolomite is formed are lagoons and lakes (Last, 1990; Nascimento et al., 2019). Last (1990) provides an overview of Quaternary dolomite occurrences in lacustrine environments. He observes that of the more than 40 modern dolomite occurrences, over 95% are found in salt lakes. The dolomite is generally interpreted as a primary precipitate. One of the first localities with lacustrine dolomite were the lakes of the Coorong region in Australia (Mawson, 1929). The primary dolomite that is formed in these lakes is very similar to the dolomite that is formed in sabkha environments (Warren, 2000). Like sabkha dolomite, lagoonal and lacustrine dolomite occurrences are often associated with microbial activity (Wright, 1999; Vasconcelos et al., 2006).

Dolomite precipitation experiments

As discussed above, already in the 19th century experiments were conducted that demonstrated that dolomite hardly precipitates from an oversaturated solution under Earth surface temperatures. Normal seawater is supersaturated with dolomite by two orders of magnitude (Warren, 2000), but dolomite does not precipitate. Even when the supersaturation was increased to a thousandfold, dolomite did precipitate in an experiment that took 32 years (Land, 1998). The only minerals that precipitate from oversaturated solutions are $CaCO_3$ and $MgCO_3$, but no ordered dolomite (Wang, 2021).

In contrast to experiments at low temperatures, high-temperature experiments have been successful in precipitating dolomite. Land (1967) conducted experiments in which dolomite precipitated at 300 °C. Using a $MgCl_2$ + $CaCl_2$ + NaCl solution, Baker and Kastner (1981) obtained dolomite in an experiment at 200 °C. Precipitation at even lower temperatures can be reached at high pCO_2 pressures (Medlin, 1959), and the dolomitization of carbonate material has been obtained at temperatures as low as 150 °C (Sibley et al., 1994).

Based on their high-temperature experiments, Sibley et al. (1994) conclude that dolomite formation occurs in three steps: (1) nucleation of very high-Mg calcite (VHMC) or nonstoichiometric dolomite, (2) an induction period in which post-nucleation growth of VHMC and/or nonstoichiometric or stoichiometric dolomite occurs and (3) replacement of (a) $CaCO_3$ by VHMC or nonstoichiometric dolomite and (b) $CaCO_3$, VHMC and nonstoichiometric dolomite by stoichiometric dolomite. Of these three steps, the induction period is very long, whereas the replacement takes place relatively rapidly. From this, Sibley et al. infer that the failure of obtaining dolomite in experiments can be explained by the long induction period, but that this does not mean that dolomite formation cannot occur under Earth surface conditions, given enough time and stable conditions. Based on this information, Arvidson and MacKenzie (1997) developed a kinetic model that yielded successful results when applied to several case studies. However, models like these are based on the

extrapolation of high-temperature data to low-temperature conditions, without experimental confirmation of low-temperature dolomite formation.

A recent contribution to our understanding of dolomite precipitation has been made by Kim et al. (2023). They reported the growth of a dolomite crystal at 80 °C by rapidly changing the saturation of the solution. In this way, disordered Ca-Mg carbonate that prohibited the precipitation of dolomite was rapidly redissolved again. This leads to an acceleration of dolomite formation. However, ambient temperatures were still not reached in this experiment and the temperature at the location of dolomite growth could have been even higher by the energy of the electron beam that was shot at the crystal. Additionally, the experiment started with a preexisting dolomite crystal and is therefore no instance of direct dolomite precipitation from a solution.

The very slow formation of dolomite under Earth surface pressure and temperature suggests that there is more to the origin of massive dolomite formations in the sedimentary record than precipitation from an oversaturated solution. If there are additional environmental conditions or a catalyst that can increase the rate of dolomite production, this would provide a more realistic model of the formation of dolomite deposits. Therefore, Brady et al. (1996) state that the “trick” to unravel the dolomite problem is the identification of a catalyst and a demonstration that the availability of this catalyst has varied over geological time in correspondence with the formation of dolomite.

Microbially induced dolomite

Over the past few decades, the major advance in the understanding of dolomite formation has been an increasing interest in the role of microorganisms in the precipitation of dolomite. Microorganisms can be the catalyst that needs to be sought on the basis of the precipitation experiments discussed above.

The focus on microbial mediation of dolomite precipitation started in the 1990s on the basis of SEM analysis of dolomite. Folk (1993) observed abundant microbial structures in both modern and ancient carbonates, including dolomites. He suggested that microorganisms had played a role in the formation of these sediments. The same was suggested for the dolomite sediments of Lagoa Vermelha and Brejo do Espinho, coastal lagoons in Brazil, where dolomite was found in the presence of sulphate-reducing bacteria (Vasconcelos, 1994; Vasconcelos & McKenzie, 1997; Sánchez-Román et al., 2009).

On the basis of these observations, Vasconcelos et al. (1995) performed a laboratory experiment in which they grew sulphate-reducing bacteria of the *Desulfovibrio* group in a lagoonal sludge samples under anoxic conditions. TEM analysis showed that these bacteria had become encrusted with a layer of nanocrystals of dolomite, which had precipitated on the outer surface of the cells. This demonstrated that bacteria played a role in the precipitation of dolomite. In a more controlled experiment, using a growth medium and one specific strain of sulphate-reducing bacteria, the same result was found (Warthmann et al., 2000). Later experiments yielded the same results under aerobic conditions with different strains of bacteria (Sánchez-Román et al., 2008, 2009).

Bacteria stimulate the precipitation of dolomite in two ways: (1) altering the water chemistry and (2) providing loci for nucleation. The water chemistry is altered by the decomposition of organic material. This can be done via sulphate reduction under anaerobic conditions (Vasconcelos et al., 1995; Warthmann et al., 2000; Petrash et al., 2017) or via the metabolism of nitrogenated organic material under aerobic conditions (Sánchez-Román et al., 2009). In both cases, the pH and alkalinity of the solution increase, leading to more favourable conditions for dolomite precipitation.

Loci for nucleation are provided by the secretion of extracellular polymeric substance (EPS). Degrading organic molecules in the EPS attract cations such as Mg^{2+} and Ca^{2+}, which are then linked together with carbonate anions to form dolomite nuclei which then can lead

to further dolomite crystallization (Petrash et al., 2017). In this way, EPS functions as a catalyst.

1.2.2. Evaporite environments

Evaporite-dolomite associations

As discussed in paragraph 1.2.1, almost all modern dolomite is present in saline or hypersaline environments. Since these are also the environments in which evaporite minerals form, there is a close relationship between evaporite minerals and dolomite, both in modern and in ancient environments.

In the intertidal zone of Arabian sabkhas, cyanobacterial mats in which authigenic dolomite has formed are buried between several tens of centimetres of 'gypsum mush', which has precipitated in the water column (Bontognali et al., 2010). Desiccation of bacterial mats leads to desiccation cracks which are then filled with lenticular gypsum crystals (Warren, 2016a, p. 221).

Lacustrine gypsum facies

Lacustrine gypsum lithofacies are described in most detail by Magee (1991) and Mees et al. (2012). Magee (1991) studied laminated gypsum-deposits of the Australian Prungle lakes. Gypsum laminae are described as approximately 1 mm thick wavy laminae of white sugary gypsum. They are alternating with thinner detrital clay laminae. Magee (1991) interpreted these gypsum-clay couplets as varves, consisting of a period of sediment discharge in the lake during spring resulting in the clay lamina and gypsum precipitation in the water column during summer.

Gypsum crystals in these couplets are prismatic and show reverse grading, which is interpreted as initial rapid nucleation followed by slower growth as equilibrium is reached.

Similar reversely graded gypsum laminae, this time alternating with dolomite, were described by Gibert et al. (2007) and interpreted in the same way. Mees et al. (2012) likewise consider the occurrence of (reverse) grading as a characteristic of synsedimentary gypsum, which never occurs in diagenetic gypsum. Other characteristics they note are horizontal alignment of crystals and the presence of non-lenticular crystal morphologies, such as prismatic and tabular crystals. Horizontal alignment can also be produced in aeolian gypsum, but this lithofacies is characterized by rounded grains. Another characteristic of synsedimentary gypsum is the presence of celestite in the gypsum laminae (Magee, 1991).

When bottom waters become supersaturated, gypsum growth can continue at the bottom. This can lead either to bottom overgrowth of microcrystalline crystals which were formed in the water column or, when evaporative conditions prevail, to the growth of coarse-crystalline gypsum (selenite) (Bąbel, 2004).

Diagenetic gypsum in lacustrine deposits is characterized by crystal shapes that are influenced by the matrix in which the growth of gypsum has taken place. This leads to lenticular gypsum crystals (Magee, 1991; Mees et al., 2012). Experiments performed by Cody (1979) have shown that the lenticular shape is particularly influenced by the presence of organic material under alkaline conditions. Under acid conditions, crystals become elongated, but not lenticular. The gypsum crystals are often separated from each other by the matrix, indicating non-competitive growth (Ortí et al., 2014a). Another indication of diagenetic growth is the occurrence of zoning, in which gypsum crystal contain bands of the sedimentary matrix; this typically occurs when gypsum crystals form from the evaporation of interstitial brines, although it sometimes occurs during subaqueous intrasediment growth (Mees et al., 2012).

2. Materials and Methods

2.1. Study areas

For this project, the evaporite-bearing intervals of two sedimentary cores were studied. These cores were obtained from two different hypersaline lakes in Spain. The first core was derived from Laguna de Salinas (LdS), near Salinas (Alicante) in southwest Spain. The second core was derived from Laguna de Fuente de Piedra (LFP) in southern Spain, about 50 kilometres northwest of Málaga. Figure 2.1 shows the geographical locations of both cores in yellow, as well as the locations of two sediment cores whose data will be used for comparison in red.

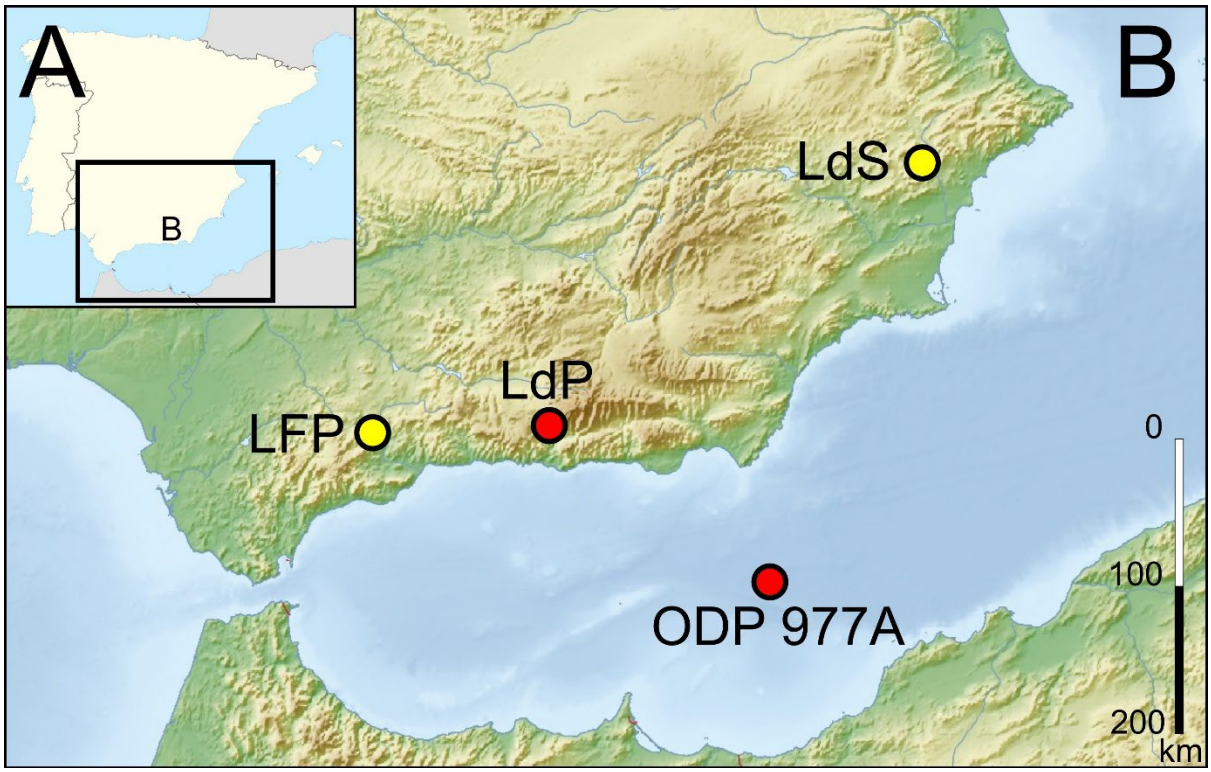

Figure 2.1. The locations of Laguna de Salinas (LdS) and Laguna de Fuente de Piedra (LFP) in southeastern and southern Spain, respectively. The locations of Laguna de Padul (LdP) (Camuera et al., 2022) and ODP 977A (Martrat et al., 2004) are indicated as well.

Figure 2.2 shows the locations of the two cores that were drilled in the lakes, as well as the locations of the cores which were analysed in other studied and are used for comparison.

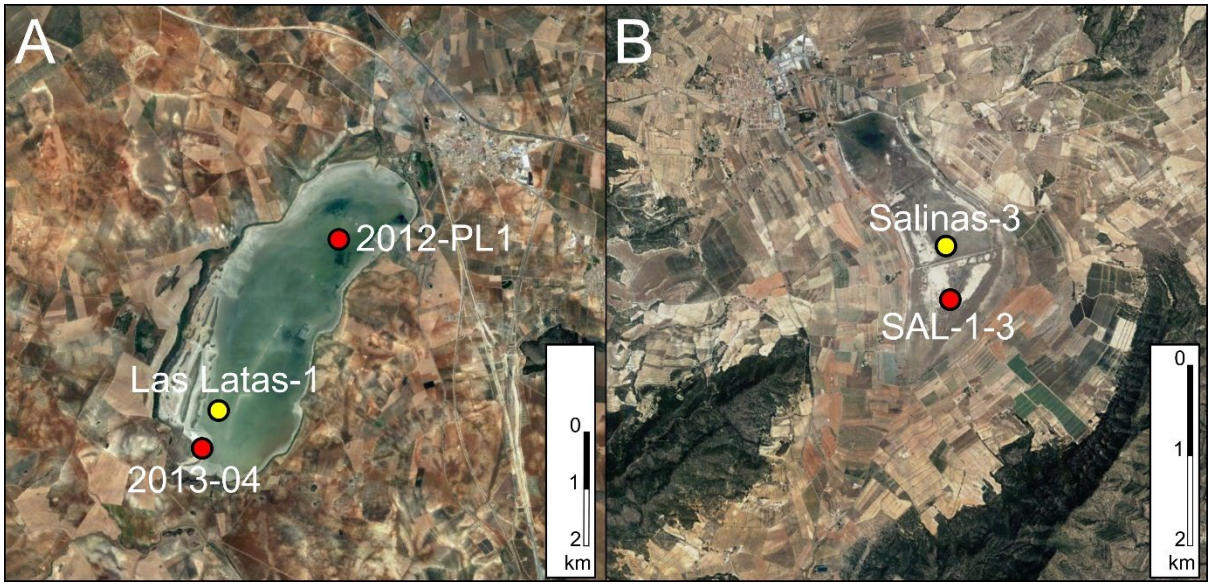

Figure 2.2. Satellite images of the two lakes, obtained from Google Earth. (A) Overview of Laguna de Fuente de Piedra, with the location of the core that was studied in for this thesis (Las Latas-1) indicated in yellow. The locations of two of the cores that were studied by Höbig et al. (2016) are indicated in red. (B) Overview of Laguna de Salinas, with the location of the core that was studied in for this thesis (Salinas-3) indicated in yellow. The location as indicated by Giralt et al. (1999) from which three cores (SAL-1 to SAL-3) were derived is indicated in red.

2.1.1. Laguna de Salinas

The Laguna de Salinas (known in Catalan as Llacuna de Salines) near Salinas (Alicante) is a playa lake of 3 by 2 km with a surface area of approximately 1.6 km^2. The lake is situated at the eastern end of the Alpine Betic Chain, about 40 km northwest of Alicante, and has a catchment area of about 71 km^2 (Giralt et al., 1999). It lies at approximately 475 m above sea level (Burjachs et al., 2016).

The lake lies in a basin that is covered by Quaternary alluvial sediments. To the northwest, there is a small mountain range called Serra de les Salines, reaching a maximum height of 1240 m above sea level. This mountain range consists primarily of limestone and dolomite units. A second mountain range, with a maximum height of 762 m above sea level, is present to the southeast. These mountains consist primarily of limestone units. To the north, there are areas with outcrops of the Triassic Keuper Formation, which consists of gypsum-bearing sediments.

The lake is fed by runoff and groundwater; the mean annual precipitation in the area is 350 mm and the annual evapotranspiration is 1500 mm (Giralt et al., 1999). Due to groundwater exploitation, the lake is only filled during rainy periods, when it contains high-salinity water. Na^+, Mg^{2+} and Ca^{2+} are the dominant cations and SO_4^{2-} and Cl^- are the dominant anions (Giralt, 1998). Although no detailed hydrochemical data are available, it can be assumed that the salt in the lake mainly derives from the Keuper Formation, the only evaporite-bearing formation in the catchment area. The lake is covered and surrounded by halophytic vegetation (Pepiol-Salom et al., 1999).

2.1.2. Laguna de Fuente de Piedra

The Laguna de Fuente de Piedra is a playa lake of 6.8 by 2.5 km with an elliptical shape and a surface area of 13.5 km^2, which makes it the largest saline lake in Spain (Girela & Martos, 1998; Höbig et al., 2016). It is located approximately 55 km northwest of Málaga. At 408 metres above sea level, it is the hydrological sink of an endorheic basin of 150 km^2 (Rodríguez-Rodríguez et al., 2016). The lake itself is seasonal, desiccating during summer and reaching a maximum water depth of 1.76 m at high stands. The lake margin is surrounded by halophytic vegetation and hosts the only breeding colony of flamingos on the Iberian Peninsula, as well as a variety of other birds (Girela & Martos, 1998).

Laguna de Fuente de Piedra is surrounded by a variety of different geological units which are part of the Chaotic Subbetic Complex, which forms a synorogenic mélange unit consisting primarily of Triassic clays and evaporites that incorporate Jurassic, Cretaceous and Cenozoic blocks (Pedrera et al., 2016). To the south and northeast, Triassic rocks, belonging to the Keuper Formation and consisting of marls and gypsum, crop out. There are two blocks of Jurassic dolomite and limestone to the east and northeast, which form low mountain ranges that surround the lake basin (Rodríguez-Rodríguez et al., 2016). The other sediments are

Paleogene in age or younger and consist primarily of marls, calcarenites and sands. These sediments cover the underlying Triassic Keuper Formation and are thinning towards the south.

The hydrology of the Laguna de Fuente de Piedra region has been a source of many studies because of its importance to the regional population and environment. An overview of these studies has been given by Rodríguez-Rodríguez et al. (2016). Although the lake is fed by precipitation and several ephemeral streams, the main contribution comes from groundwater.

Kohfahl et al. (2008) identified two principal flow systems: one flow system of primarily meteoric freshwater towards the lake which can become saline through interaction with outcropping evaporite rocks. A second flow system develops below the lake in the form of convection cells which recycle brines. Rodríguez-Rodríguez et al. (2016) name this model "the most accepted conceptual model" for the Laguna de Fuente de Piedra hydrological system.

In contrast to this model, Heredia et al. (2004; 2010) propose a model in which there are three principal groundwater flow systems. One flow system is shallow and is situated in the outcropping Miocene and Quaternary rocks. A second flow system is of intermediate depth and is developed in the marly and gypsiferous sediments in the subsurface. Third, there is a deep karst system which is larger than the Fuente de Piedra basin.

The dissolution of Triassic evaporites by groundwater and surface water leads to a high salinity of the lake water. The lake water chemistry is dominated by Na^+, with Mg^{2+} and Ca^{2+} as secondary cations, and the dominant anion is Cl^- with SO_4^{2-} as secondary anion (Rodríguez-Rodríguez et al., 2005). The surface water of the lake is supersaturated with respect to aragonite, calcite and dolomite; all other minerals are undersaturated (Rodríguez-Rodríguez et al., 2005).

2.2. Materials

2.2.1. Salinas-3 (Laguna de Salinas)

The Salinas-3 (from now on referred to in the text by the informal name 'Alicante') core from Laguna de Salinas has a total length of 31.0 m and a diameter of 8 cm. The core was taken from the middle of the lake, about 500 m from the shore, where the long axis of the lake bends from a northwestern direction to a southwestern direction (Figure 2.2B). For several intervals, no data were available for the research of this thesis. These are indicated in Figure 2.6. The core consists mostly of homogeneous intervals of carbonate sediments (including dolomite) of green, brown and grey colours. These intervals are separated by mud and evaporite layers. Most evaporite layers consist of selenite crystals and are up to 20 cm thick. In Figure 2.3, one of these layers is shown. Often, these selenite layers are impure, as the crystals are covered and mixed with carbonate sediment.

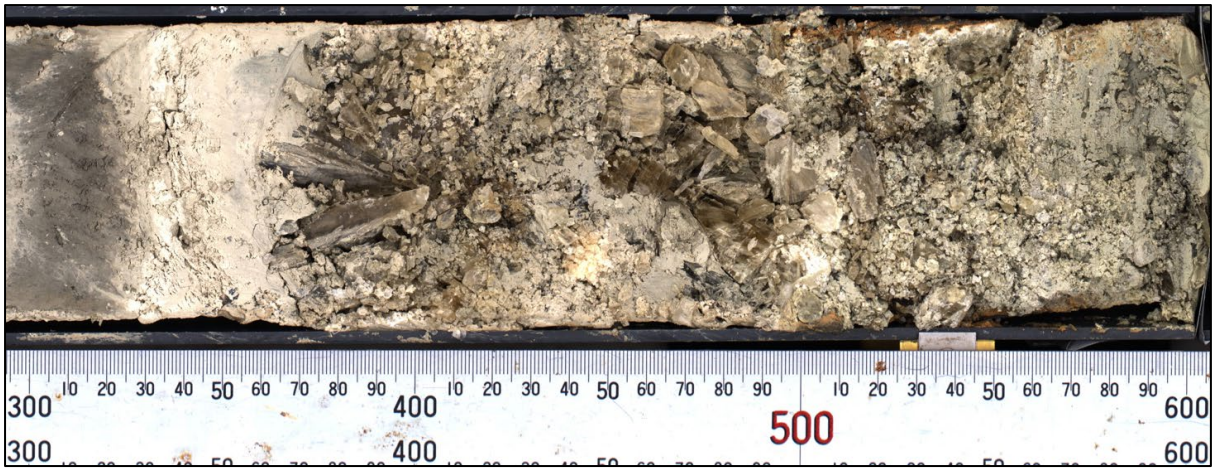

Figure 2.3. Example of a selenite layer in the Salinas-3 core. The picture shows the interval between 930 and 960 cm depth. The scale bar is in mm.

The stratigraphy of Alicante is presented in Figure 2.6. Selenite layers are mostly present in two intervals of the core. Between 5.40 and 16.00 m, there are multiple selenite layers present, especially between 11.80 and 16.00 m. Below 16.00 m, there is an interval without any evaporite layers that extends to 27.50 m. In the lower part of the core, between 27.50 and 30.30 m, there are again some selenite layers. The non-selenitic intervals consist mostly of

homogeneous carbonate mud, with colour changes on decimetre to metre scale. An exception is the interval between 1.90 and 5.00 m, which is strongly laminated. A part of this laminated interval is shown in Figure 2.4. In other sections of the core, laminae are rare, although they are present in a section around 24.30 m.

Figure 2.4. Part of the laminated interval of the Salinas-3 core. The picture shows the interval between 200 and 230 cm depth. The scale bar is in mm.

2.2.2. Las Latas-1 (Laguna de Fuente de Piedra)

The sedimentary succession of Laguna de Fuente de Piedra was studied on the basis of the Las Latas-1 sediment core (from now on referred to in the text by the informal name 'Las Latas'). The core has a length of 46.20 m and a diameter of 8 cm. The core was drilled in the southwestern part of the lake (Figure 2.2A), approximately 600 m from the shore.

The first 7.20 m of the core has been recovered by percussion, which has led to a distortion of the laminae which were the target of this study. Therefore, this section of the core has not been used, except for the construction of the stratigraphy and XRF analysis. For one interval, between 1500 and 1560 cm, no data were available for the research of this thesis. This interval is indicated in Figure 2.6.

The core consists mostly of carbonate sediment of a green-grey colour. Homogeneous intervals of carbonate sediments can extend to multiple metres. These intervals are separated by mud or evaporite laminae. Evaporite laminae are generally a few millimetres thick, with a

maximum of 2 cm. They consist of microcrystals with a bright white colour, giving the laminae a sugar-like appearance. In some cases, multiple laminae form an evaporite-rich interval by alternating with dolomite laminae. In other instances, single laminae are present in an interval of homogeneous dolomite. Figure 2.5 shows an example of the alternation between evaporite laminae and dolomite.

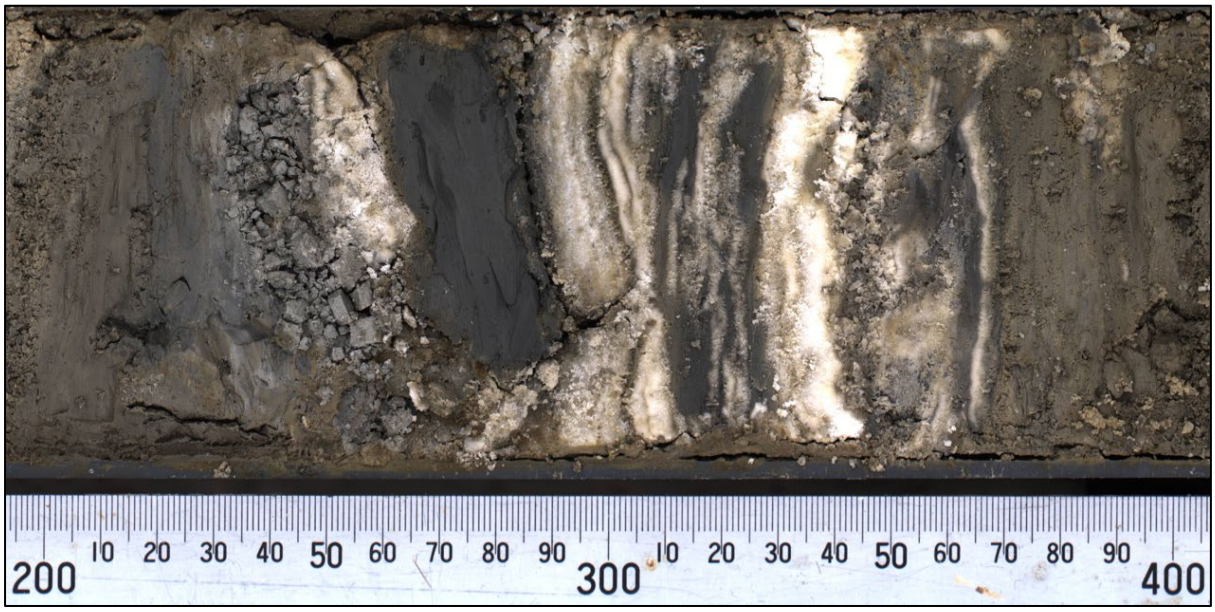

Figure 2.5. Microcrystalline evaporite laminae with a dolomite interval in the Las Latas-1 core. The picture shows the interval between 2540 and 2560 cm depth. The scale bar is in mm.

The stratigraphy of Las Latas is presented in Figure 2.6. Evaporite laminae are mostly present in the bottom of the core, and their frequency declines gradually from bottom to top. Moreover, many evaporite laminae appear to form bundles, which are separated by intervals with evaporite laminae. However, there is no clearly distinguishable regularity in the thickness of these bundles, the number of laminae they consist of, and the depth by which they are separated from other bundles.

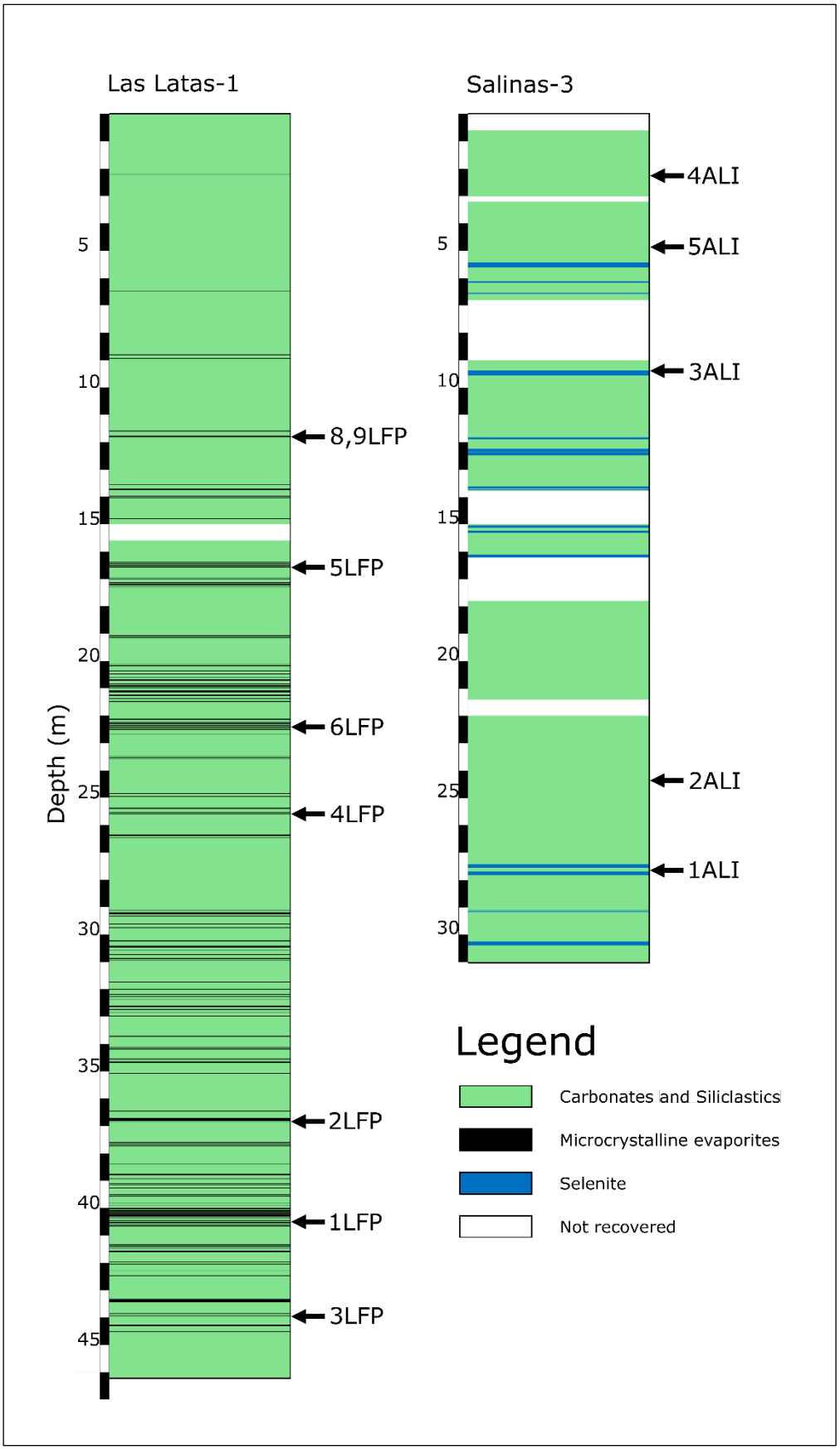

Figure 2.6. The stratigraphy of Las Latas-1 (left) and Salinas-3 (right). 'Not recovered' implies that no picture of the core or other material was available.

2.2.3. Sampling

Five samples from each core were selected for thin section, elemental and isotopic analysis (Figure 2.6 and Table 2.1). The samples from the Alicante core were named 1ALI to 5ALI and the samples from the Las Latas core were named 1LFP to 5LFP. For sulphur and oxygen isotope analysis, three additional samples were taken from the Las Latas core to get statistically more reliable results (6LFP, 8LFP and 9LFP). Since these samples have not been part of the other analyses, references to 'ten samples' in the discussion of the other analyses refer to samples 1 to 5ALI and 1 to 5LFP.

To get a representative view of each core, the samples were taken from different sections of the cores. Additionally, samples were selected in such a way that evaporite layers with different morphologies were. The selenite layers from the Alicante core proved hard to sample for thin section preparation. Therefore, only one of such layers, in a part where the selenite crystals were relatively small, was sampled (3ALI).

The exact locations of the samples that were taken for the preparation of thin sections are shown in Figure 2.7 (Alicante) and Figure 2.8 (Las Latas).

For the measurement of element concentrations and isotope ratios, care was taken to select as little dolomite as possible. However, since most evaporite laminae were very thin and were intercalated with dolomitic mud, it was not possible to avoid dolomite entirely. This was also evident from the presence of residual carbonate traces, as will be discussed below.

Table 2.1. List of the samples that were selected for analysis.

Sample name	Core	Depth (m)
1ALI	Salinas-3	27.65
2ALI	Salinas-3	24.30
3ALI	Salinas-3	9.40
4ALI	Salinas-3	2.20
5ALI	Salinas-3	4.90
1LFP	Las Latas-1	40.50
2LFP	Las Latas-1	36.80
3LFP	Las Latas-1	43.95
4LFP	Las Latas-1	25.50
5LFP	Las Latas-1	16.55
6LFP	Las Latas-1	22.44
8LFP	Las Latas-1	11.95
9LFP	Las Latas-1	11.92

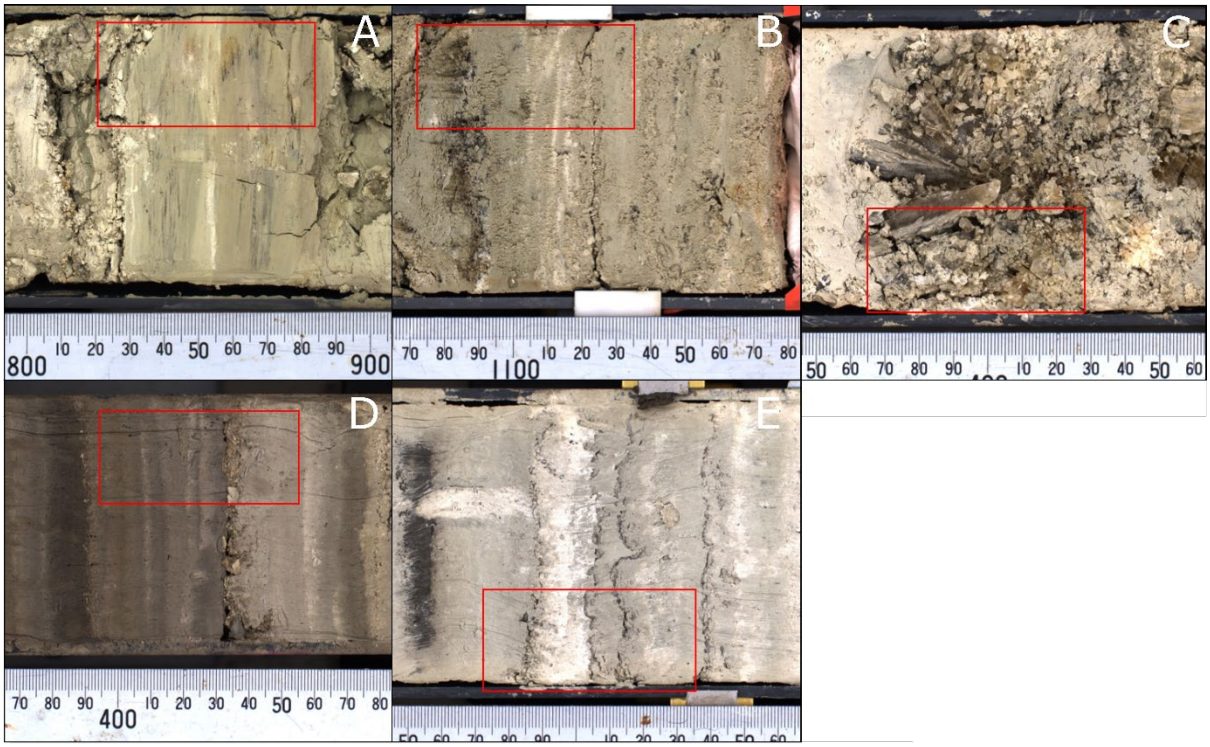

Figure 2.7. The exact locations, indicated by a red rectangle, of the samples that were taken for the preparation of thin sections of 1ALI (A), 2ALI (B), 3ALI (C), 4ALI (D) and 5ALI (E). Scale bars are in mm.

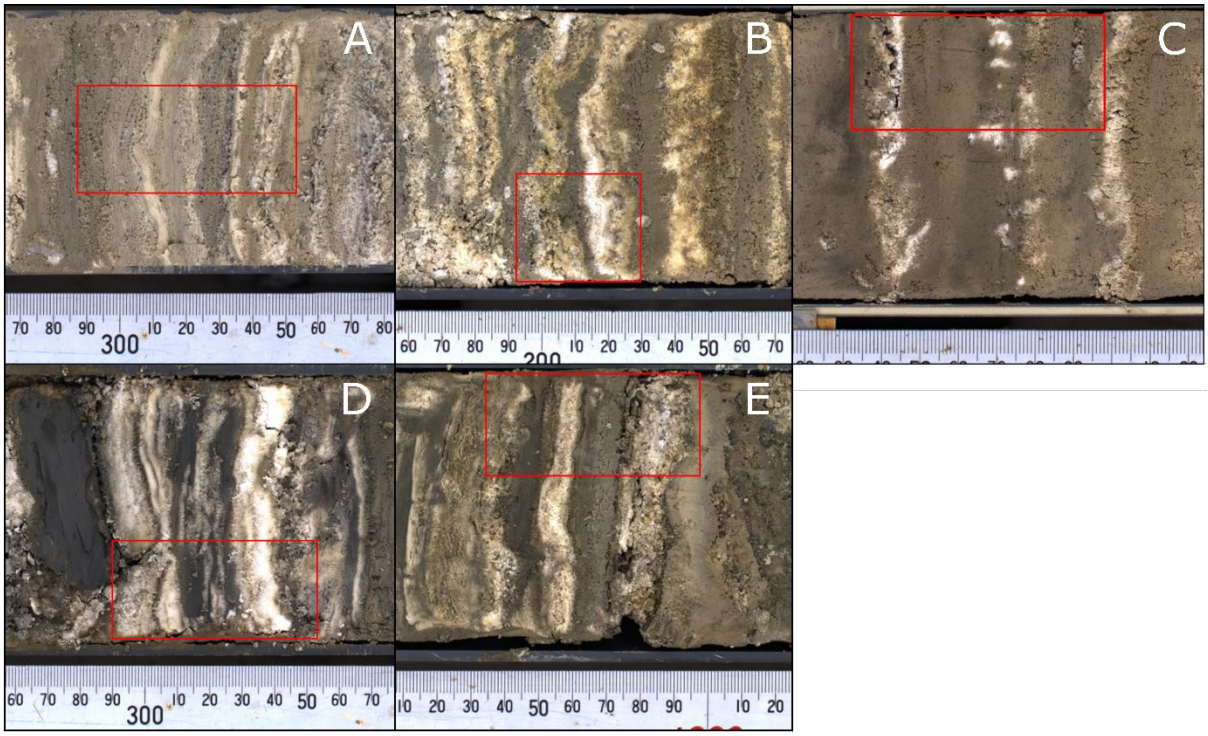

Figure 2.8. The exact locations, indicated by a red rectangle, of the samples that were taken for the preparation of the thin sections of 1LFP (A), 2LFP (B), 3LFP (C), 4LFP (D) and 5LFP (E). Scale bars are in mm.

2.3. Methods

The research of this thesis consists of two parts. In the first part (2.3.1 to 2.3.5), petrographic and geochemical analyses were performed to reconstruct the paleoenvironmental conditions under which the evaporite layers in both cores were formed. For comparison to the dolomite intervals of the core, additional inductively coupled plasma optical emission spectroscopy (ICP-OES) and X-ray diffraction (XRD) data were available that are yet unpublished. In the second part (2.3.6), the data from the first part are included in a chronological framework to relate sedimentary changes in the cores to paleoclimatic variability.

2.3.1. Thin section analysis

Of each sample, a thin section was prepared by an external company (Petrographica Westerbork). Blocks of sediment were impregnated with blue epoxy resin using vacuum

pressure impregnation. After that, the blocks were attached to a glass slide of 27 by 46 mm, sawn and polished.

A high-resolution overview picture of each thin section was made with a Zeiss microscope and associated software. These overview pictures were made with 5x magnification using reflected light. More detailed analyses were made using a Nikon Eclipse 50iPOL optical microscope with associated software. This microscope had lenses with a magnification of 2x, 4x, 10x, 20x and 100x. Both transmitted and polarised light were used.

2.3.2. SEM-EDS

Based on the thin section analysis, one sample (2ALI) was selected for scanning electron microscopy combined with energy dispersive X-ray spectroscopy (SEM-EDS) to determine the differences in elemental composition between gypsum, dolomite, and dark spots on the gypsum crystals that were visible in the thin section. Since the thin section itself was covered with glass, the sawn-off counterparts of the thin sections were used for this analysis.

The scanning electron microscope used for the analysis was a JEOL JCM-6000. To avoid image distortion by electromagnetic interference, the sample was covered with a graphite coating. The view of the sample was magnified 100 to 540 times, in such a way that the entire view consisted of only one specific target (i.e., gypsum, dolomite or a dark spot). After that, EDS was performed on the entire visible area.

2.3.3. Elemental analysis

Sample preparation

Elemental concentrations of gypsum were measured on ten samples using inductively coupled plasma optical emission spectroscopy (ICP-OES). After the acquisition of the samples

from the core, these samples were dried in an oven at 40 °C. Next, the sediment was crushed into powder by means of a pestle and mortar. For each sample, about 11 mL of Milli-Q Ultrapure Water was added to 100 to 400 µg of powder in a test tube. The test tubes were shaken for about 18 hours to get optimal dissolution of gypsum.

After that, the gypsum solution was separated from the residue by centrifuging the samples at a rate of 3500 rotations per minute and pipetting the solution into other tubes. The solution was then dried on a hotplate for ten days between 70 and 95 °C. Next, a few drops (<1 mL) of 15 M nitric acid (HNO_3) were added, which were dried on a hotplate in 5 hours. 3 mL of 3 M nitric acid were added to dissolve the gypsum. To this solution, MilliQ was added in such a proportion as to obtain a dilution factor of 10,000. Otherwise, the concentration of the major elements would likely be above the detection limit of the spectrometer. 10 mL of this final solution was used of each sample for ICP-OES analysis.

ICP-OES analysis

The elemental concentrations were measured using a Varian 720-ES ICP Optical Emission Spectrometer. The ten samples were analysed, as well as magnesium-calcium and multiple element matrix-matched standard solutions of different concentrations. In addition, certified standard reference material, limestone and dolomite (JDo, 88b, CRM512 and CRM513), were measured with the sample batch. The results were processed by determining for each wavelength whether the measured element concentration fits with the expected value of the standards. If this was the case, this wavelength was considered accurate and the accompanying element concentration was reported.

2.3.4. XRF analysis

XRF data that were obtained with the Avaatech XRF core scanner at the Dutch Institute for Sea Research (NIOZ) from scanning the cores with an interval of 1 cm were analysed. The XRF datasets comprised both the Las Latas core and the Alicante core. For both datasets, the following procedure was followed.

First, all XRF measurements at which the argon counts yielded a positive value were excluded. The measurement of argon indicates that air was measured, which would mean that the scanner was separated from the sediment. When argon positive data were excluded, there were no depths at which the number of counts was exceptionally lower than on average, something which could indicate that instead of sediment, something else was measured.

Next, five core pictures were selected to compare fluctuations in element counts and element ratios on the one hand and mineralogical changes on the other. The aim of this was to determine which element counts or element ratios formed the best indicator of the presence of evaporites. The five core pictures contained the intervals 1560-1680 cm, 1680-1800 cm and 3660-3780 cm from Las Latas and 440-560 cm and 900-1020 cm from Alicante. The XRF graphs of nine elements (Mg, Ca, Al, S, Si, Ti, K, Cl and Br) and eight element ratios (log(Ca/Sr), log(Ca/Ti), log(Fe/Al), log(Fe/Ca), log(Mn/Ti), log(Mn/Ca), Sr/Ti and S/Fe) were compared to determine which best indicated the presence of evaporite intervals.

When these were selected, a MATLAB script was written to create a stack of core pictures by means of which the changes in the selected elements and ratios could be compared to mineralogical changes.

Next, the other elements (Mg, Ca, Al, Si, Ti, K, Cl and Br) and element ratios (log(Ca/Sr), log(Ca/Ti), log(Fe/Al), log(Fe/Ca), log(Mn/Ti), log(Mn/Ca) and Sr/Ti) that were potentially environmentally significant were compared to the element and element ratio most indicative of evaporites.

Lastly, principal component analyses (PCAs) were performed on the XRF data to observe patterns and variations within the elemental data by determining which elements formed clusters together. Additionally, XRD data that were previously obtained for carbonate samples were included in the PCA of Alicante to determine the relationship between elements and minerals.

2.3.5. Sulphur and isotope analysis

2 g of sediment per sample was selected for sulphur ($\delta^{34}S$) and oxygen isotopes ($\delta^{18}O$). These samples were sent to the University of Barcelona where the isotope measurements were performed by using a Finnigan DELTAplus XP isotope ratio mass spectrometer of Thermo Fisher Scientific.

2.3.6. Age model

^{14}C data

Age models were constructed for both cores on the basis of ^{14}C dates. For both the Las Latas and the Alicante core, four dolomite samples were ^{14}C dated by the Poznań Radiocarbon Laboratory (Table 2.2). For the Alicante core, eight additional ^{14}C dates were obtained from Giralt (1998) (Table 2.3). The samples that were dated were obtained from a different core, but the stratigraphic description and photographs from the core showed that the stratigraphy of both cores is very similar. To account for small differences in stratigraphically equivalent depth, the depth measured by Giralt (1998) in the core used by him was assumed to be no more than 20 centimetres different from the stratigraphically equivalent depth in the Alicante core.

Table 2.2. ^{14}C ages of the eight samples that were selected from the cores for this purpose.

Sample	**Core**	**Depth (m)**	**^{14}C age (yr BP)**	**Std. Dev. (yr)**
Las Latas B3-S	Las Latas-1	13.4	37,200	800
Las Latas 65	Las Latas-1	18.1	28,810	300
Las Latas RC-33.6	Las Latas-1	33.6	29,740	330
Las Latas RC-45.87	Las Latas-1	45.87	43,000	2200
Alicante 6	Salinas-3	2.17	8,570	50
Alicante 27	Salinas-3	11.78	20,410	160
Alicante 60	Salinas-3	18.13	34,900	600
Alicante 80	Salinas-3	25.99	21,210	170

Table 2.3. ^{14}C ages obtained by Giralt (1998) from the SAL-1 to SAL-3 cores from Laguna de Salinas. The column 'Depth in Salinas-3 core (m)' shows the inferred stratigraphically equivalent position to the depth in the cores studied by Giralt.

Sample	**Measured depth (m)**	**Depth in Salinas-3 core (m)**	**14C age (yr BP)**	**Std. Dev. (yr)**	**Type**
SAL-1a	0.88	0.68 – 1.08	2,830	60	Pollen
SAL-1b	1.65	1.45 – 1.85	7,400	60	Pollen
SAL-2a	1.75	1.55 – 1.95	7,660	50	Carbonate
SAL-3	2.71	2.51 – 2.91	8,570	70	Wood
SAL-1c	3.44	3.24 – 3.64	8,810	60	Pollen
SAL-1d	4.30	4.10 – 4.50	10,120	60	Carbonate
SAL-2b	5.10	4.90 – 5.30	11,540	110	Pollen
SAL-1e	8.70	8.50 – 8.90	24,590	250	Pollen

Age model construction

The age models were constructed with the programme *Undatable* (Lougheed & Obrochta, 2019). In this programme, the dolomite samples were entered as '14C sediment' and the pollen and wood samples as '14C terrestrial fossil'. IntCal13 was chosen as calibration, without reservoir age. All samples were included in the bootstrapping process. It was assumed that the top of the core corresponds to the present; therefore, an age of 0 years at 0 m was added as a tie point. The process of finding a fit of the data was iterated 100,000 times.

Alicante age models

Three age models were constructed for the Alicante core, based on different choices with respect to the reliability of the data. These age models will be named AM1, AM2 and AM3.

AM1 is the age model that is generated by *Undatable* when all data Table 2.2 and 2.3 are included (Figure 2.9). In this model, the data points at 8.50-8.90 m, 11.78 m and 18.13 m are not included in the fit, which means that they are older samples that are reworked. However, this age model is not ideal, for two reasons. First, it leads to a very dramatic shift (an approximately fourfold decrease) in sedimentation rate around 13 ka / 5.0 m in order to include the sample at 25.99 m. Although such a shift is not impossible, it seems more natural to include the sample at 11.78 m, which would imply a more gradual change in sedimentation rate. As will be discussed below, there is a mineralogical shift around 5.0 m in the form of an absence of selenite layers above this level. However, selenite layers form only a minor fraction of all parts of the core, so their presence or absence should not change the average sedimentation dramatically. In other respects, there are no clear differences between the sediment above 5.0 m and below this level, which is inconsistent with the hypothesis of a large shift in sedimentation rate. Second, AM1 has to exclude three data points, whereas other possible age models can fit more data points.

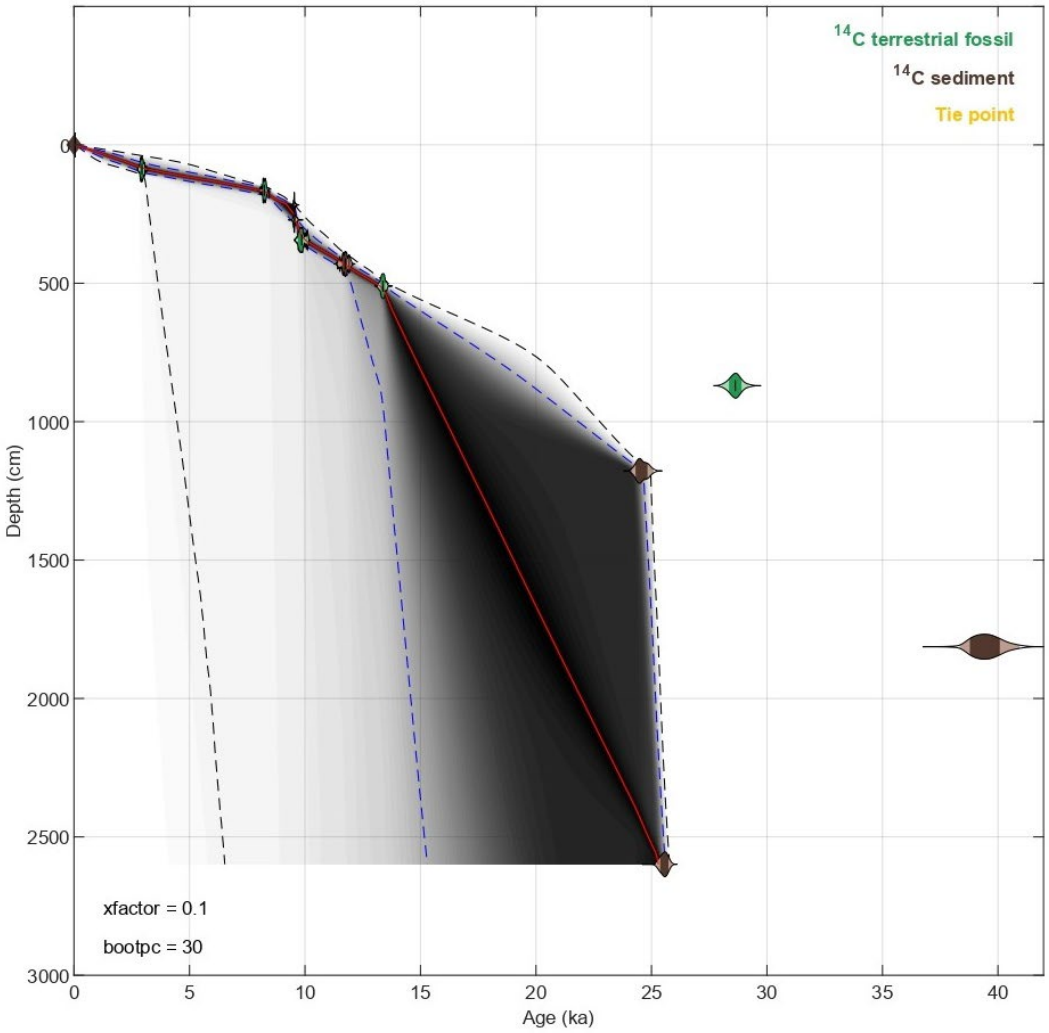

Figure 2.9. Depth-age model of Salinas-3 in AM1. The red line indicates the most probable fit. The black lines represent all iterations.

AM2 (Figure 2.10) is the age model that is generated by *Undatable* when the data point at 25.99 m is excluded. In this age model, only two data points (at 25.99 m (not shown in the figure) and at 8.50-8.90 m) are excluded. The sedimentation rate does not show any remarkable shift, and the data point at 11.78 m fits nicely between the data points at 4.90-5.30 m and 18.13 m, indicating a very stable sedimentation rate between 40 and 10 ka.

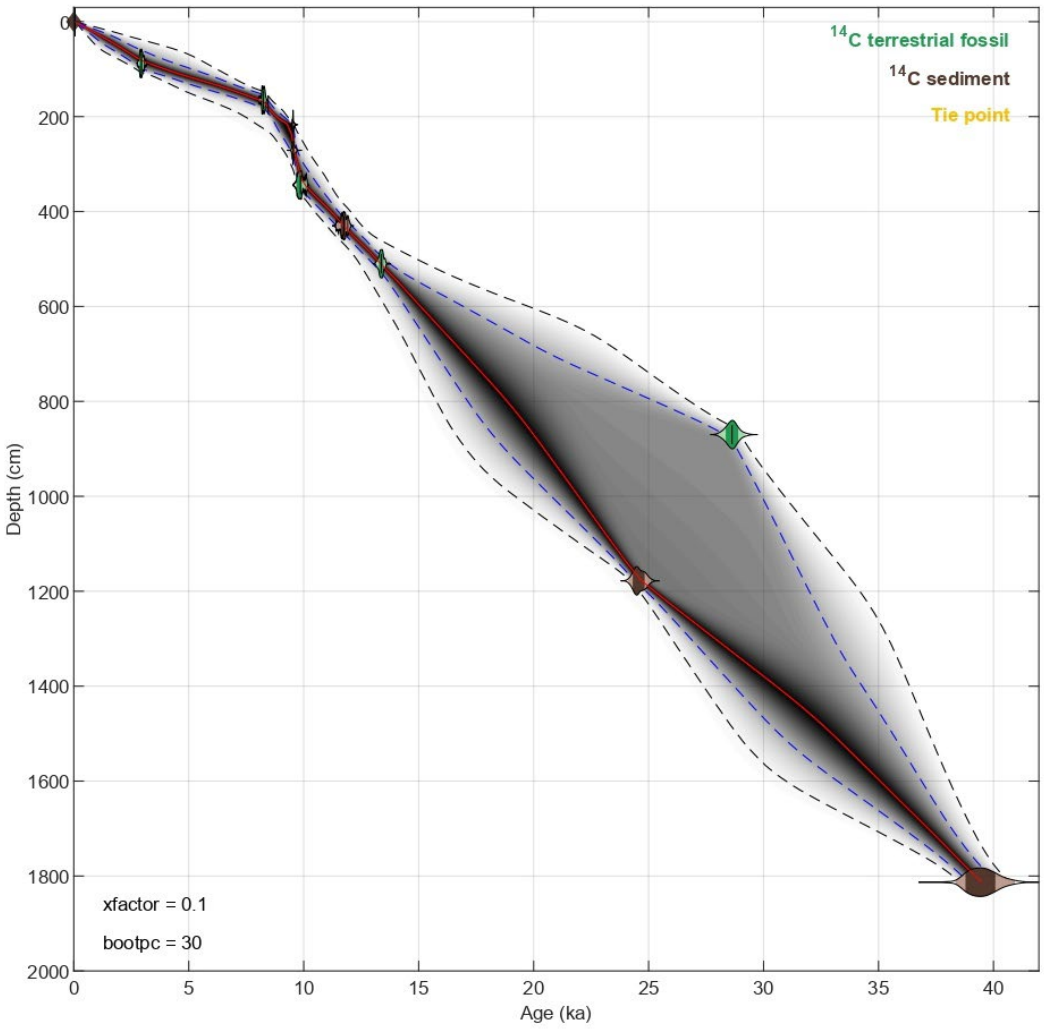

Figure 2.10. Depth-age model of Salinas-3 in AM2. The red line indicates the most probable fit. The black lines represent all iterations.

AM3 (Figure 2.11) is the age model in which it is assumed that if any samples are reworked, they have been transported to a stratigraphically lower position. Therefore, the age model is based on the oldest dates possible. This means that two data points (at 25.99 m and at 11.78 m) were excluded. In this respect, the model does not provide a fit with the data that is worse than AM2. However, the sedimentation rate shows more variance than in AM2, without mineralogical differences that indicate that shifts in sedimentation rate indeed took place.

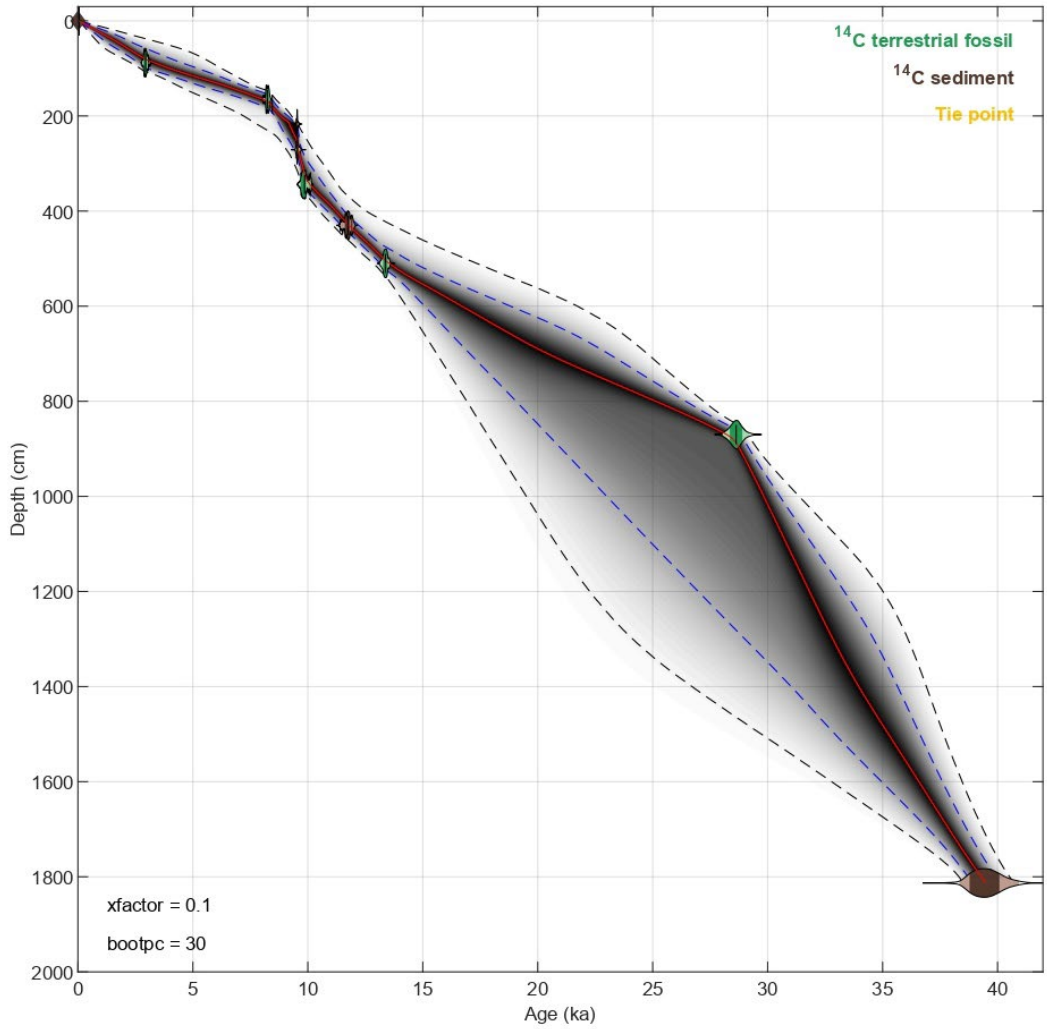

Figure 2.11. Depth-age model of Salinas-3 in AM3. The red line indicates the most probable fit. The black lines represent all iterations.

Of the three age models, AM2 provides the most plausible fit of the data points. Since reworking in lacustrine environments can shift sediment both to higher and lower stratigraphic positions (Höbig et al., 2016), there is no particular reason to choose AM1 or AM2 because of the pattern of reworking in these models. Therefore, AM2 will be used as the best age model.

To obtain an age model for the entire core, the average accumulation rate in the 100 cm above the lowest data point (at 1813 cm depth) was extrapolated to the bottom of the core. Although this extrapolation is necessarily accompanied by uncertainty, it can serve for illustrative purposes how the bottom part of the core is connected to age. The final age model

that was used by combining the mean age of AM2 and the extrapolation for the bottom part of the core is shown in Figure 2.12.

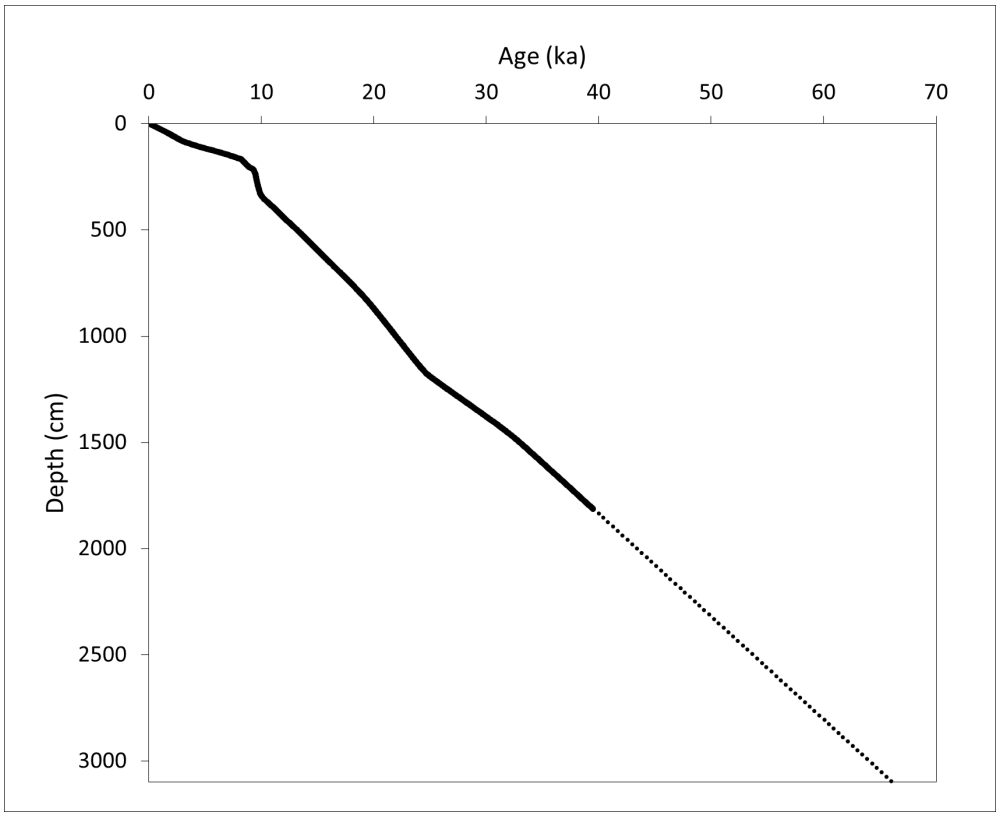

Figure 2.12. Depth-age model of Salinas-3 in AM2, which was selected for analysis of the data. The dotted line is the extrapolated part of the age model.

Las Latas age model

Figure 2.13 shows that the data points for Las Latas are too inconsistent to create a reliable age model. The data point at 13.40 m has a higher age than the data point at 18.10 m, so at least one of them must be the result of reworking. The data points at 18.10 and 33.60 m have almost the same age, despite the fact that they are 15.50 m apart, leading to an unrealistically high average sedimentation rate in this interval. Therefore, little can be said about the best age model for Las Latas on these data alone.

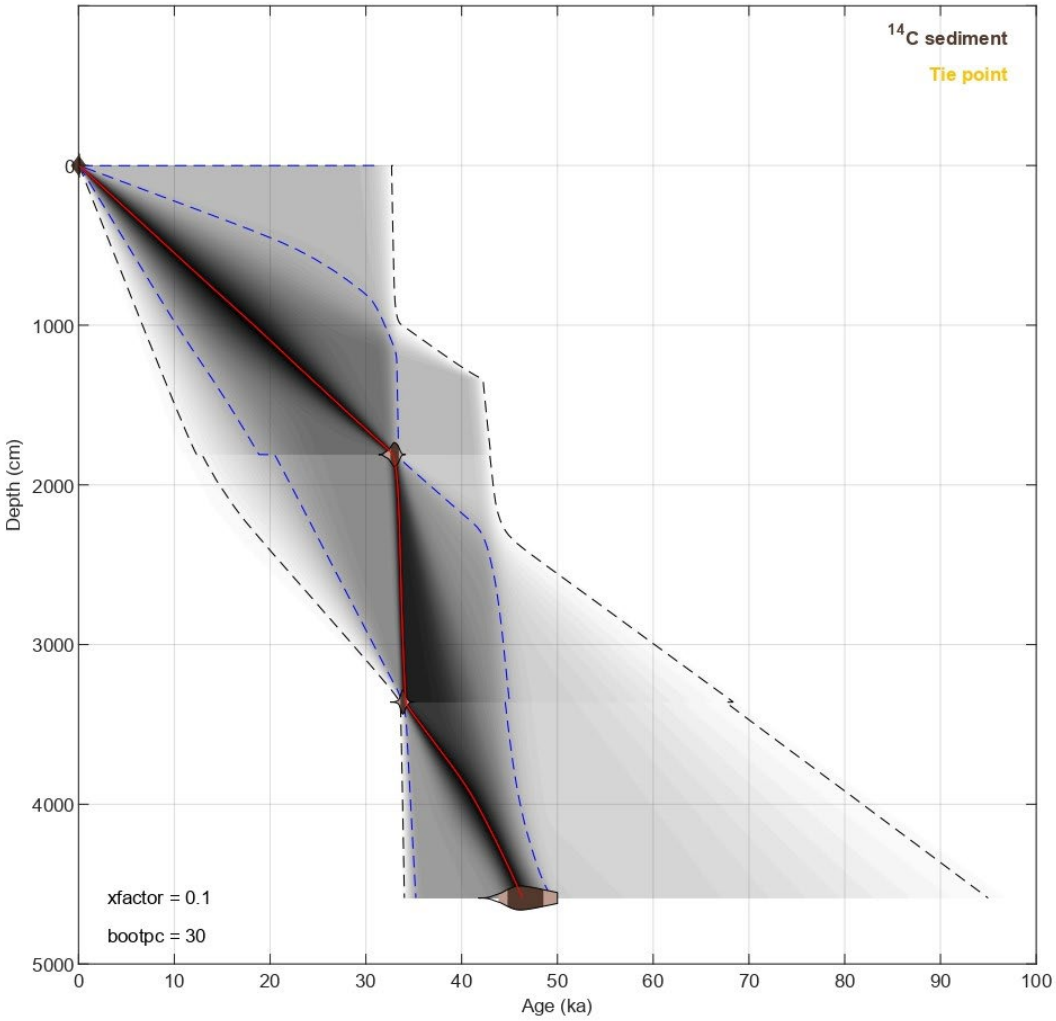

Figure 2.13. Resulting depth-age model when all data from Las Latas-1 are included. The red line indicates the most probable fit. The black lines represent all iterations.

An age model of a different core (2013-04, see Figure 2.2A) from Laguna de Fuente de Piedra was provided by Höbig et al. (2016). Their paper does not provide enough information to make an accurate stratigraphic correlation between the core of their study and the Las Latas core. Therefore, it cannot be taken for granted that both cores are stratigraphically similar, as the clastic input rate and the precipitation rate of authigenic minerals could differ. However, the two cores come from the same part (the southwestern part) of the lake, and a comparison of the age model of Höbig et al. (2016) with the data points of the Las Latas core showed that the data from both points can provide a coherent age model. Therefore, the four data points from Höbig et al. (2016) were included in the calculation of the age model, and

the data point at 33.60 m was excluded, since it could not be matched with the data point at 18.60 m.

The resulting age model (Figure 2.14) shows a plausible fit between age and depth. Therefore, this age model was selected to compare the results from the Las Latas core with age, although the assumption of a stratigraphic equivalence between the Las Latas core and core 2013-04 makes the age model tentative. The final age model, including an extrapolation from the lowest data point (at 45.87 m) to the bottom of the core (at 46.20 m), is presented in Figure 2.15.

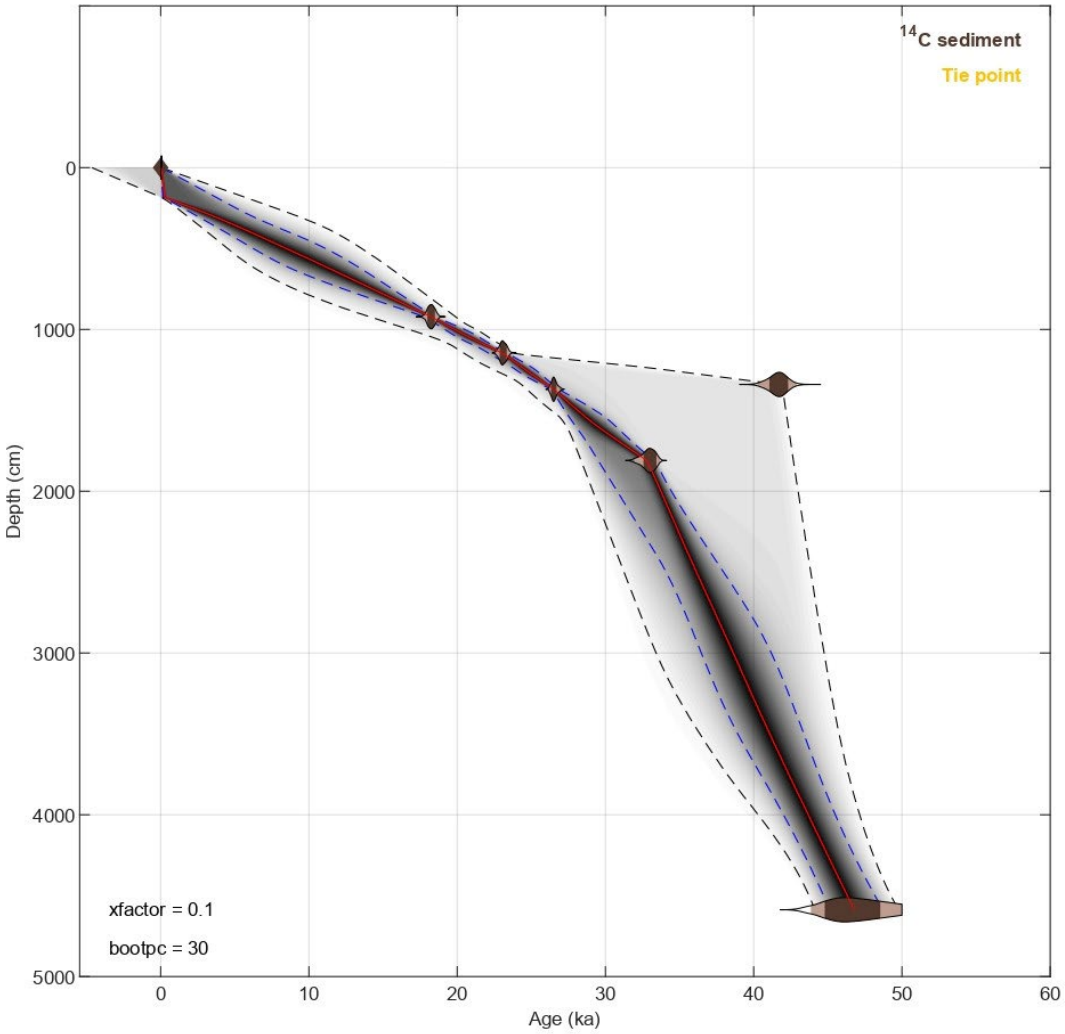

Figure 2.14. Depth-age model of Las Latas-1 when the data point at 33.60 m depth is excluded and four data points from Höbig et al. (2016) are included. The red line indicates the most probable fit. The black lines represent all iterations.

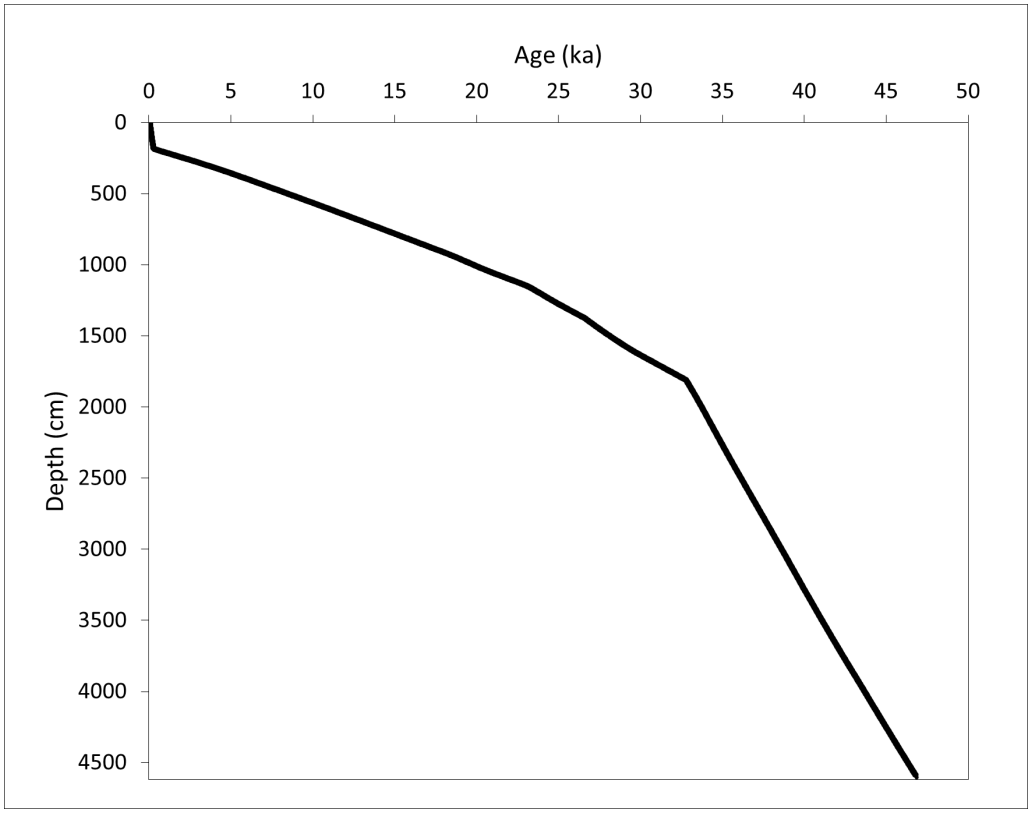

Figure 2.15. Depth-age model of Las Latas-1, which was selected for analysis of the data.

3. Results

3.1. Thin section analysis

3.1.1. 1ALI

Description

This thin section (Figure 3.1) consists mostly of dolomitic mud. Within the matrix of dolomite, there are some levels in which gypsum crystals are present. The dolomite itself is micritic, consisting of very small (<2 μm) globular grains. The dolomite has a brown colour of different brightness in different parts of the thin section. These characteristics of dolomite are similar in all thin sections. There are some levels with black particles which seem to be organic matter. Some sponge spicules could also be found in the dolomite (Figure 3.2).

There are two prominent levels with gypsum crystals at the bottom of the thin section and one in the upper half. These levels lead to a vague lamination of the thin section, but really distinct laminae are absent. Gypsum crystals are mostly between 20 and 150 μm in size and have irregular shapes; a minority of crystals are rounded.

At different locations, there are patches of homogeneous gypsum of a few mm in size, which are associated with a region of lighter material, consisting of irregular patches of gypsum and dolomite.

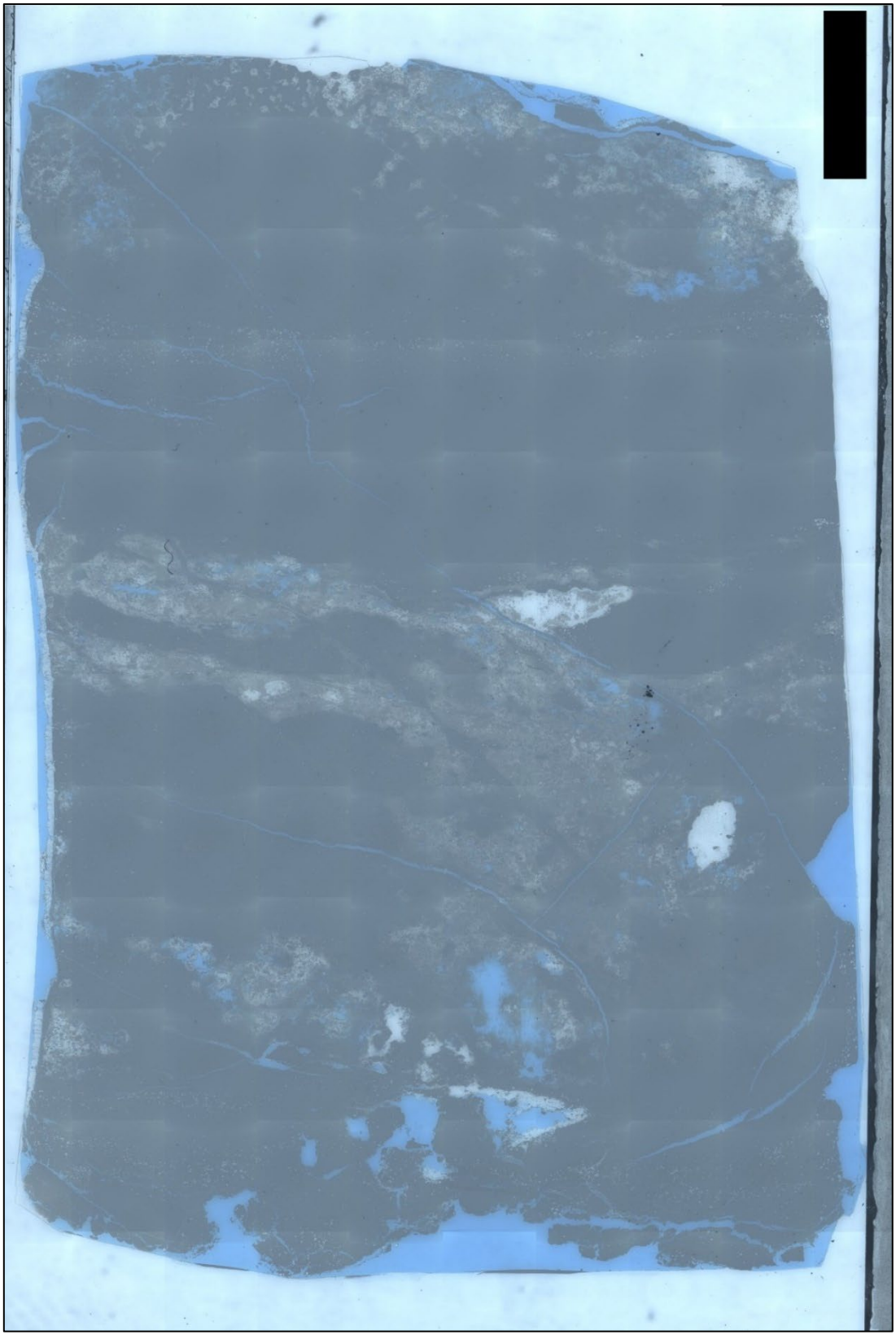

Figure 3.1. Thin section of 1ALI. Scale bar is 5 mm.

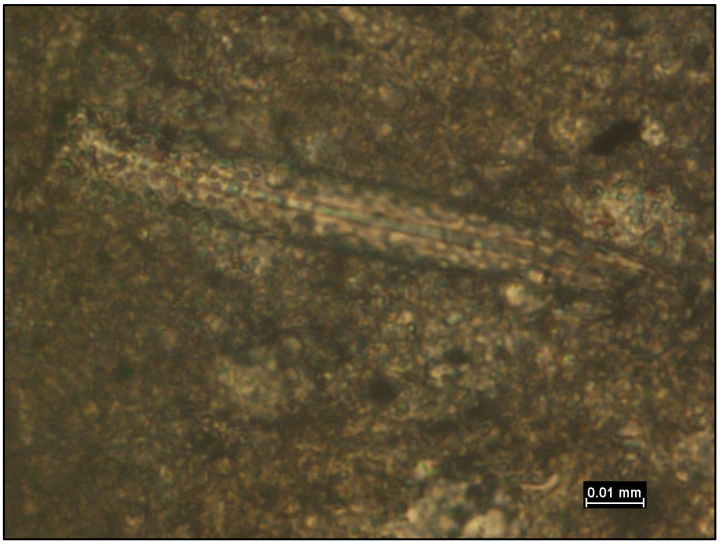

Figure 3.2. Sponge spicule in dolomite (1ALI).

Interpretation

The gypsum crystals within the dolomite matrix are most readily explained as early diagenetic gypsum that has originated from precipitation in interstitial water. The irregular distribution of the gypsum crystals over the thin section and the distance between them is inconsistent with primary precipitation.

The patches of homogeneous gypsum are best interpreted as pore infillings. They are evidence that the accumulation of dolomite has incidentally created voids of a few mm in size, which were then filled with gypsum. These voids can have multiple origins, such as the decomposition of organic matter or the generation of gas bubbles from microbial activity (Aref et al., 2020). Since the sediment is not lithified, the infilling must have occurred before compaction was possible.

It can be concluded that this thin section does not contain any synsedimentary gypsum, but only gypsum that has precipitated from interstitial and ground water within the sediment.

3.1.2. 2ALI

Description

This thin section (Figure 3.3) is well laminated and is composed of gypsum and dolomite in approximately equal proportions. Most laminae are between 0.5 and 1.5 mm thick. The laminae are in most cases not easily separable, as the thin section consists of dolomite laminae which are alternatingly gypsum-rich and gypsum-poor, or which differ by the size of the gypsum crystals in the lamina. The gypsum crystal size ranges between 10 and 40 μm in some laminae and between 70 and 400 μm in others, or in between these extremes. Most crystals have irregular, angular and non-elongated shapes. Aside from gypsum and dolomite, the thin section contains clastic grains and foraminifera (Figure 3.4).

Some laminae consist of pure gypsum. Near the bottom of the thin section, there is a thick (1.45 mm) lamina consisting of relatively large crystals (up to 350 μm). There is reverse grading visible in this lamina. In the upper part of the thin section, there are four laminae of pure gypsum, in which most gypsum crystals are relatively small (between 20 and 70 μm), lenticular and elongated. The thickness of these laminae are variable (on average 300 μm) and the crystals in them show a horizontal orientation.

In the middle of the thin section, there is a discontinuous layer of pure, massive gypsum of about 2.5 mm thickness. This massive gypsum contains at some spots a black stain, especially at the top of the layer (Figure 3.5). Another patch of pure gypsum is present near the top of the thin section. Some gypsum crystals in other parts of the thin section contain a black stain as well.

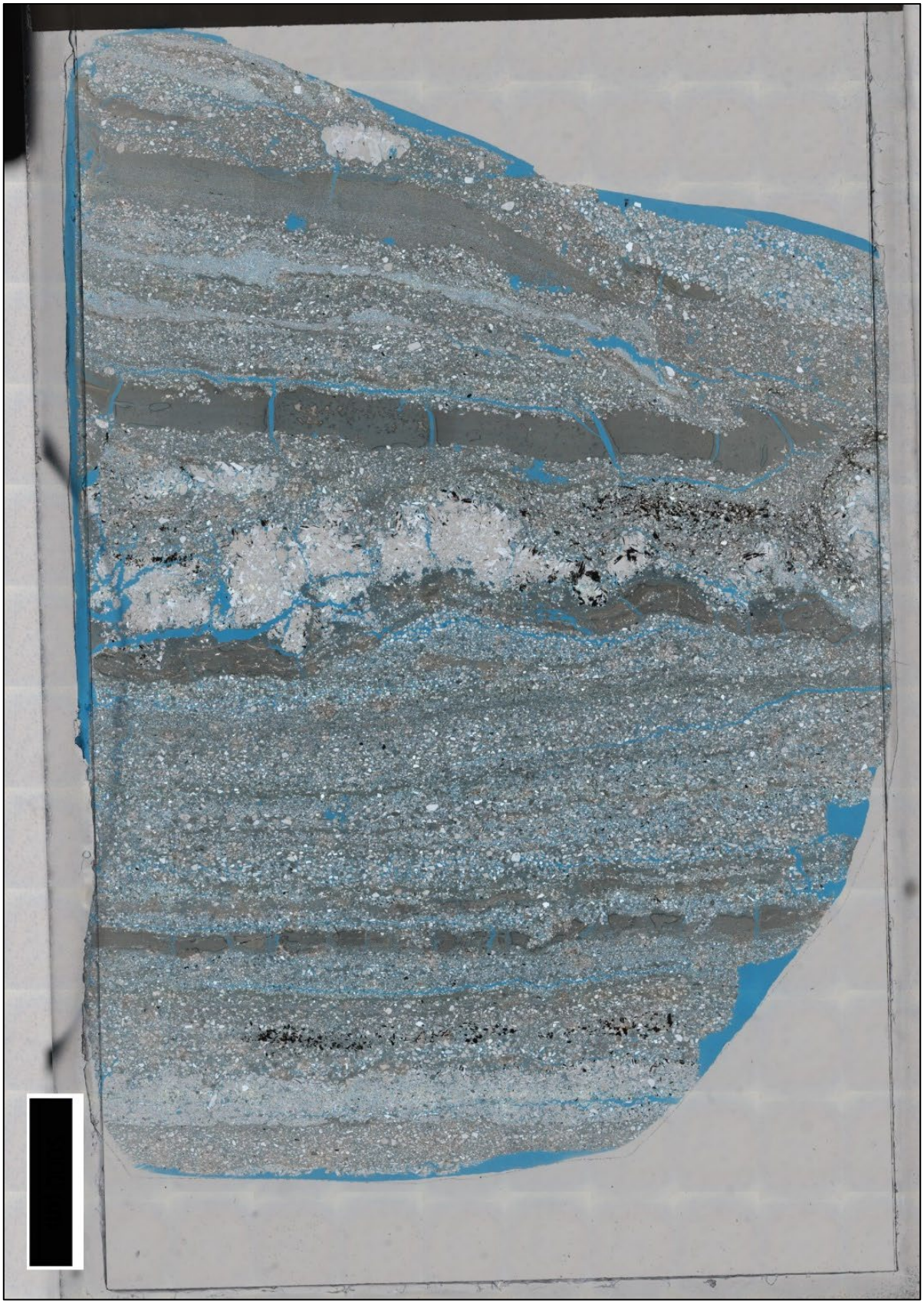

Figure 3.3. Thin section of 2ALI. Scale bar is 5 mm.

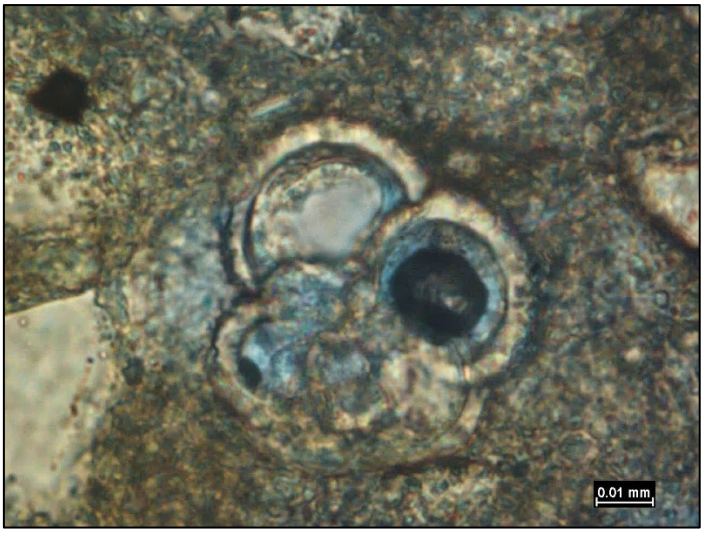

Figure 3.4. Foraminifera (species unknown) in dolomite matrix (2ALI).

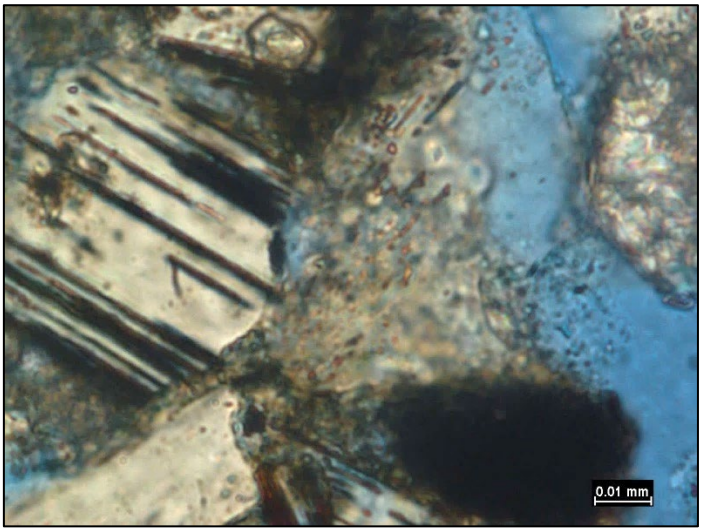

Figure 3.5. Gypsum crystals with black stripes (2ALI).

Interpretation

The lamination that is present in this thin section suggests that the precipitation of gypsum was part of regular (probably annual) sedimentary cycles. The fact that most gypsum is present within a dolomite matrix without showing competitive growth, indicates that the gypsum formed from interstitial brines rather than in the water column. The gypsum is therefore early diagenetic, forming within the dolomite soon after precipitation, when the dolomite mud was still porous and could easily give space to gypsum crystals. The discontinuous layer of pure, massive gypsum is probably the infilling of a large void.

The presence of clastic grains indicates some water input from runoff during the period of deposition. The foraminifera that are present might be species that were able to thrive in the lake, or else reworked specimens that were transported.

The laminae of pure gypsum are evidence of incidental synsedimentary gypsum formation. The very small crystals in the laminae of the upper part of the section may be related to the formation of a 'gypsum crust' which formed after complete desiccation.

The black stains that are present in some gypsum crystals are similar to black stains observed by Magee (1991), who interpreted them as iron oxides formed by the activity of sulphate-reducing bacteria. To confirm this interpretation, SEM-EDS analysis was performed, the results of which will be presented in the next paragraph.

3.1.3. 3ALI

Description

This thin section (Figure 3.6) is the representative of the levels in the core that consist of large selenite crystals. The thin section shows some of these crystals. They consist of massive gypsum crystals that are horizontally fractured. It might be the case that these fractures originated during the preparation of the thin section, as the crystals that were observed in situ did not show such a fracturing. Within the crystals, elongated fluid inclusions are present that are horizontally aligned. The size of these fluid inclusions ranges between 10 and 40 μm. Within the crystals, there are series of vertical or subvertical filaments of micritic dolomite (Figure 3.7).

The selenite crystals are encased in a dolomite matrix which contains small gypsum crystals. In the lower right corner, gypsum crystals are particularly abundant, but in other areas, they are relatively sparse. The dolomite is micritic and dark green, with occasional star-shaped lighter discolorations. Most gypsum crystals in the dolomite matrix are slightly

rounded and range between 10 and 50 μm. There is no clear lamination visible in this thin section.

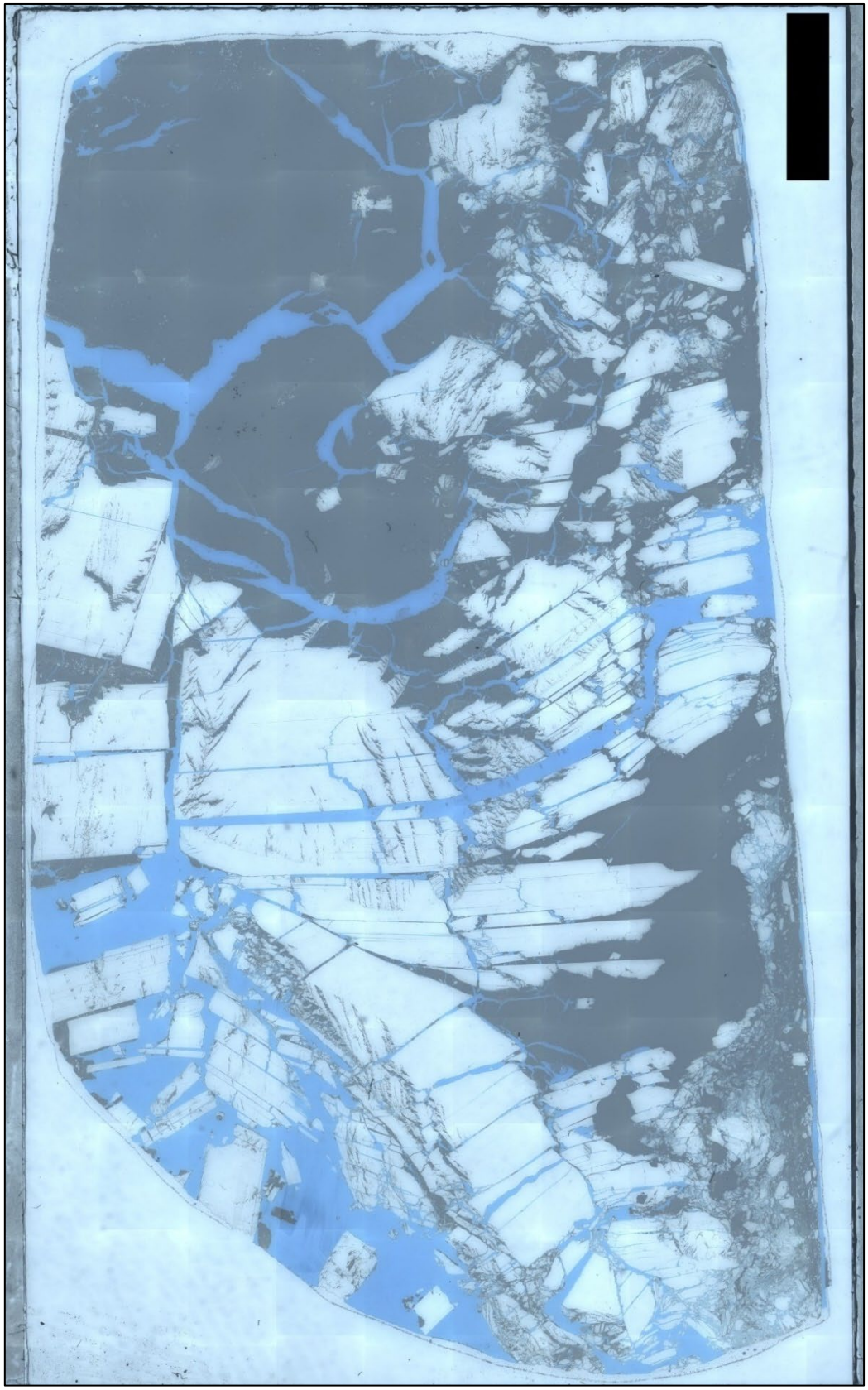

Figure 3.6. Thin section of 3ALI. Scale bar is 5 mm.

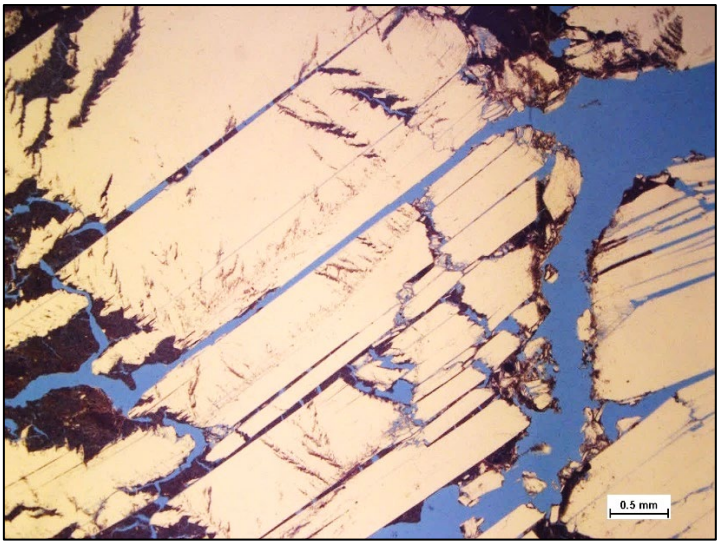

Figure 3.7. Closeup of a part of a selenite crystal, showing filaments of dolomite within the gypsum (3ALI).

Interpretation

The formation of selenite crystals, some of which are several centimetres in size, indicates long-term stable evaporative conditions. Therefore, these selenite crystals must have formed during periods in which the water level was relatively high and crystal growth was not inhibited by dolomite formation. The small traces of dolomite within the selenite crystals indicate that dolomite formation had not entirely stopped.

The uninhibited growth of selenite crystals, without interference of dolomite production, is generally interpreted as an indication of high salinity, which leads to unfavourable conditions for microorganisms (Bąbel, 2004). This means that the selenite intervals in the Alicante core are indicative of hypersaline conditions, even though the water level was still high enough for selenite formation.

The gypsum crystals within the dolomite matrix are best interpreted as early diagenetic gypsum. The fact that they are very rare in the dolomite at the top of the thin section indicates that this dolomite formed under low salinity conditions.

3.1.4. 4ALI

Description

This thin section (Figure 3.8) consists almost entirely of dolomite which consists of vague laminae. Within the dolomite matrix, a large amount of grains of various colours is present, including gypsum crystals ranging from 20 to 70 μm. Aside from gypsum crystals, there are dark grains which are probably of organic material, foraminifera (Figure 3.9), clusters of translucent globular structures of 5-10 μm (Figure 3.10) and clastic grains.

In the bottom half of the thin section, there are some irregular veins that are filled with a white mineral that is possibly gypsum (Figure 3.11). Most veins are horizontal, parallel to the bedding, but there are vertical or oblique veins connecting the others. The mineral in the veins is homogeneous, but separated by thin layers of dolomite. In the upper half of the thin section, there is a level at which a network of thin gypsum laminae together with dolomite form a single layer.

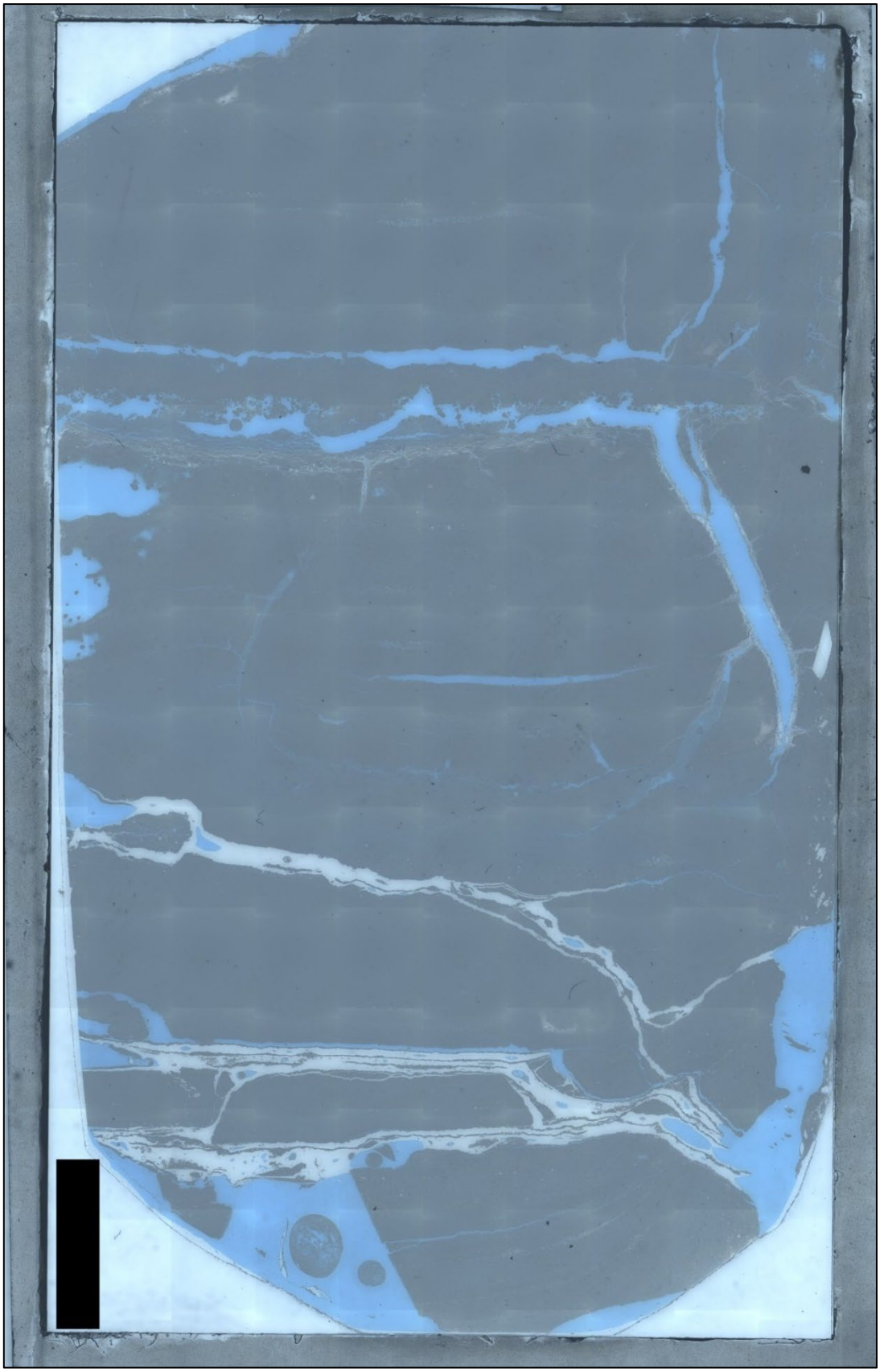

Figure 3.8. Thin section of 4ALI. Scale bar is 5 mm.

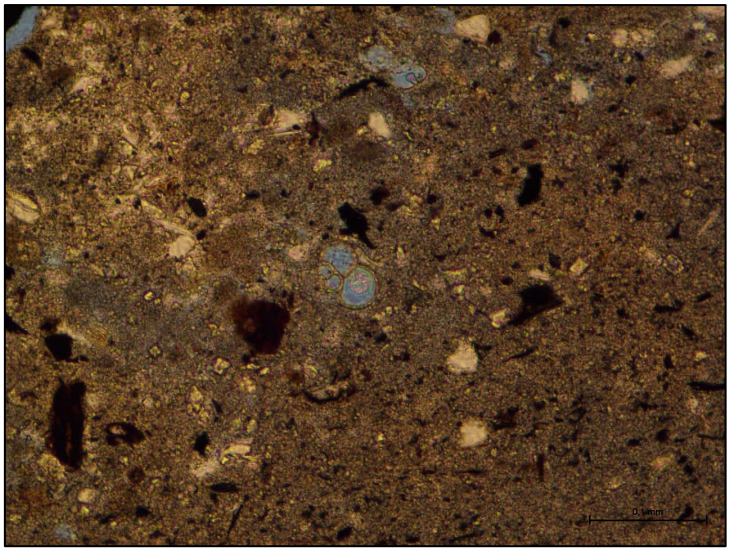

Figure 3.9. Foraminifera (species unknown) in dolomite matrix (4ALI).

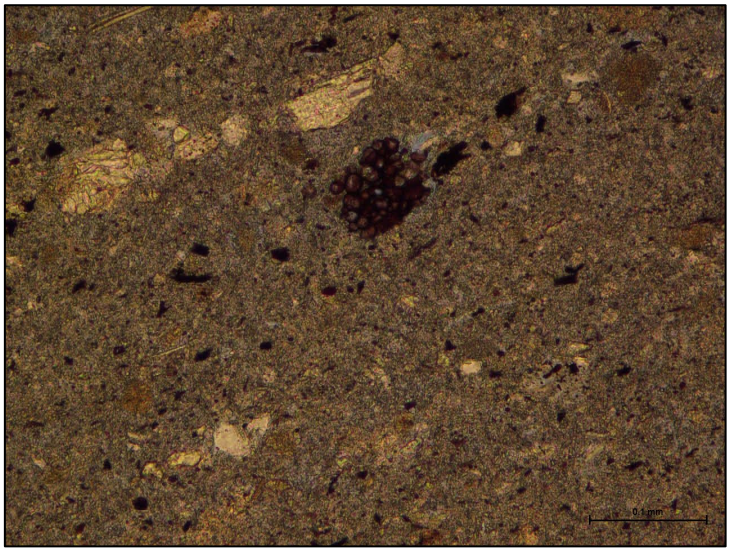

Figure 3.10. A cluster of translucent globular structures (4ALI).

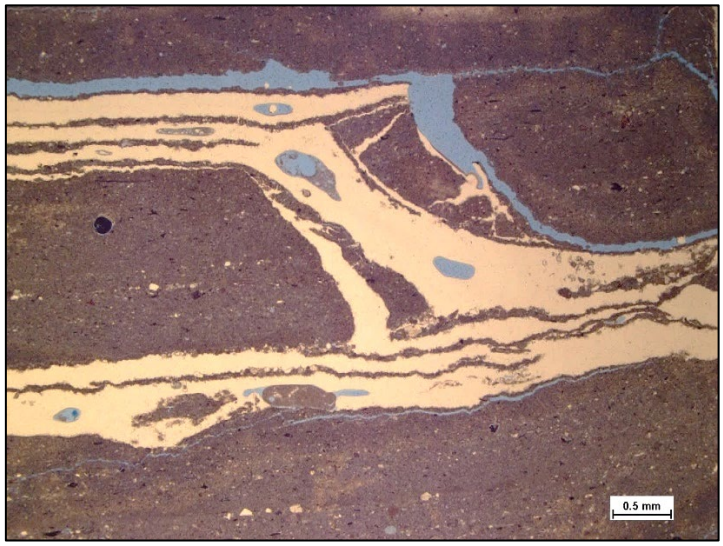

Figure 3.11. Closeup of veins filled with a white mineral (4ALI).

Interpretation

The gypsum crystals within the dolomite matrix are, as in the other thin sections from Alicante, most readily interpreted as early diagenetic gypsum. Given the high amount of clastic input and the fact that some crystals appear rounded, it might even be the case that most of the gypsum is of clastic origin.

The veins are clearly the result of infillings. The zoned character shows that this infilling occurred in multiple stages. The fact that the cracks are mostly horizontal rather than vertical shows that these are not desiccation cracks. Horizontal cracks in sediment can be produced by salinity fluctuations or by microbial activity (McMahon et al., 2017), which are both plausible mechanisms in the environment of Alicante. Another explanation is that the veins are gypsum infillings of root channels (Poch et al., 2018). Whether the mineral that occupies the veins is gypsum, cannot be established with certainty. The elemental analyses discussed below show that this sample is an outlier compared to the other samples in several respects, which could be explained by the presence of another soluble mineral.

The conglomeration of globular structures in the dolomite can be interpreted as a colony of cocci. As in the case of 2ALI, it cannot be established whether the foraminifera that are present in the dolomite sediment are reworked or not.

3.1.5. 5ALI

Description

This thin section (Figure 3.12) consists largely of dolomite with two types of gypsum being present. The first type consists of irregularly shaped laminae or patches of pure gypsum. These patches and laminae consist mostly of small prismatic crystals (40 to 140 μm in size) that do not show rounding or elongation. In the upper part of the thin section, several of these patches with a lenticular shape are separated by very thin dolomite laminae to form together

one larger lamina. Another distinctive gypsum lamina is present in the lower half of the thin section.

The second type consists of large tabular-lenticular crystals (up till 3 mm) which have all the peculiar characteristic of displaying multiple growth stages, with bands of darker material (probably dolomite) separating them (zoning) (Figure 3.13). Gypsum crystals of this second type are dispersed throughout the thin section. Some are connected closely to the lenticular patches of microcrystalline gypsum in the upper part of the section.

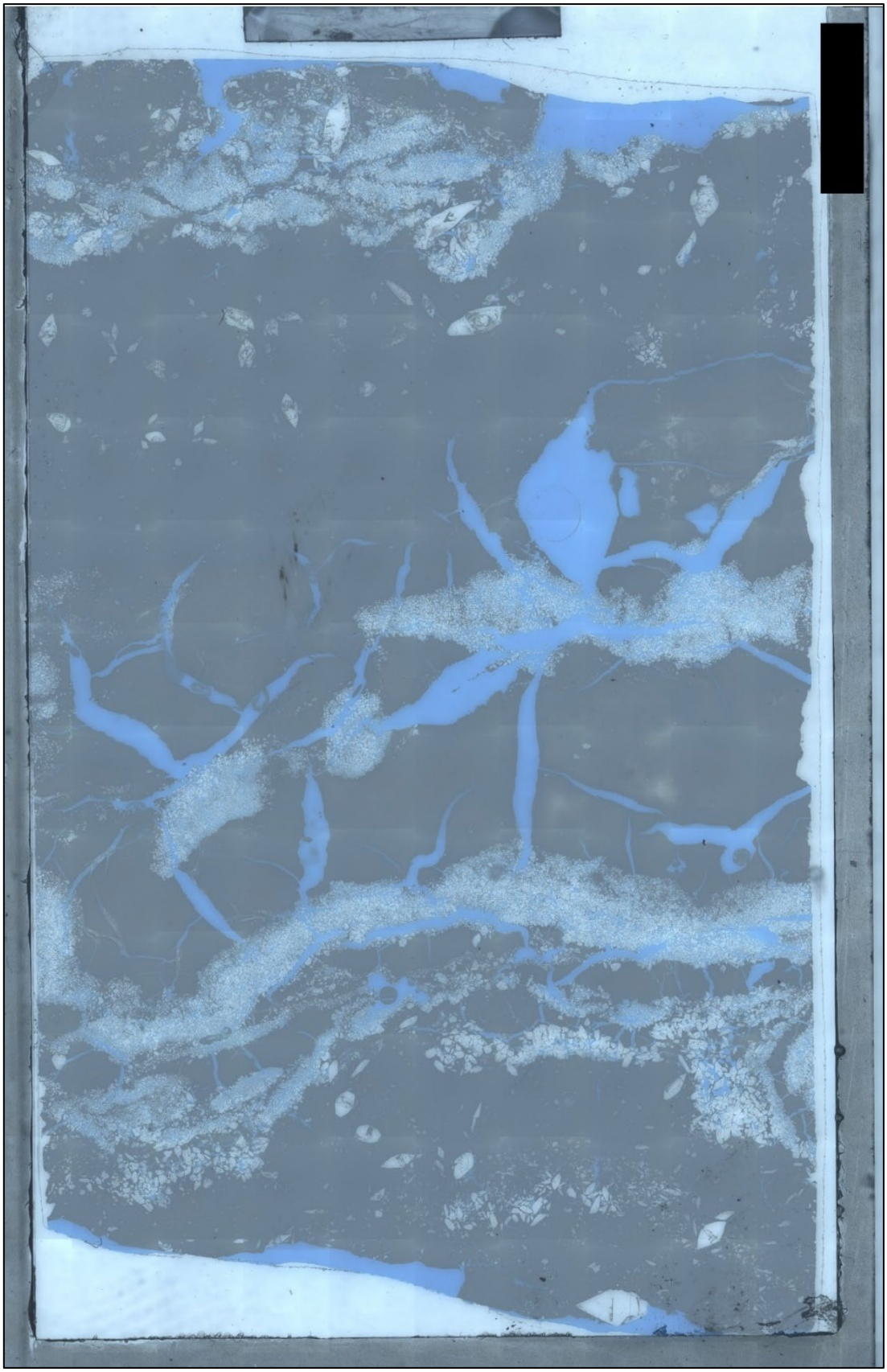

Figure 3.12. Thin section of 5ALI. Scale bar is 5 mm.

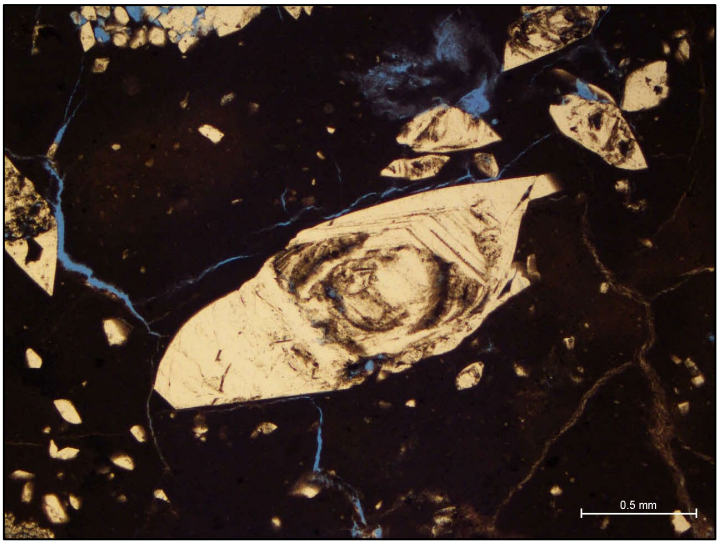

Figure 3.13. Closeup of one of the crystals with multiple growth stages (5ALI).

Interpretation

Both types of gypsum in this thin section are unique among all thin sections. The gypsum patches stand out by being microcrystalline and very pure on the one hand, but not forming continuous laminae on the other hand. The large tabular-lenticular crystals are unique in having very clearly distinguishable growth bands.

The shape of the gypsum patches is similar to the shape of large lenticular crystals. Comparable patches of microcrystalline gypsum are generally interpreted as *in situ* alteration of previous gypseous materials, occurring in soils (Artieda, 2013; Poch et al., 2018). If this is correct, the microcrystalline patches are the remnants of some very large crystals (up to 1 cm). The largest crystals that are present in the thin section are about 2 mm in length. The zoning of the larger crystals in the section are clearly the result of diagenetic growth. Zoning can occur in multiple environments (Mees et al., 2012), but is particularly common in pedogenic gypsum (Magee, 1991). Therefore, both types of gypsum are best interpreted as gypsum that has formed pedogenically.

3.1.6. 1LFP

Description

This thin section (Figure 3.14) is well laminated. In the lower half of the thin section, the lamination is not continuous: the boundaries between the laminae are unsharp, as gypsum laminae change into dolomite laminae via laminae composed of gypsum crystals within a dolomite matrix. The gypsum laminae are 3 to 5 mm thick at the thickest point and dolomite laminae are between 1 and 3 mm in thickness, but these thicknesses vary strongly laterally.

Gypsum crystals do not show a preferred orientation in any of the laminae, and vary strongly in size, with crystals as small as 20 μm filling up the spaces between crystals with sizes up to 600 μm. The dominant crystal type is tabular-prismatic, but many crystals have an irregular shape, some having one or more rounded faces and being rather tabular-lenticular. The largest crystals also have irregular shapes and seem to be an aggregate of smaller crystals.

At the right hand side of the thin section, the laminae are draped downwards and converging by the vertical expansion of one dolomite-rich lamina, which reaches a thickness of about 1.3 cm at the edge of the thin section. This lamina consists mostly of dolomite with a horizon of gypsum crystals in the middle. As the lamina extends towards the left, the gypsum horizon does not become thicker but curves downwards. The gypsum crystals in this horizon are tabular to tabular-lenticular, show a horizontal orientation and are elongated.

The upper half of the thin section consists of relatively thick gypsum laminae with a thickness of 3 to 5 mm that alternate sharply with thin dolomite laminae of 0.5 to 1.5 mm thickness. The laminae are horizontal but slightly wavy. Most of them show a clear reverse grading (coarsing-upwards) sequence (Figure 3.15). For example, in one of the laminae, the largest crystals in the lower part of the lamina are between 100 and 200 μm, whereas the largest crystals in the upper part are between 250 and 400 μm. The form of the crystals in the upper part is very similar to those in the lower part of the thin section.

Figure 3.14. Thin section of 1LFP. Scale bar is 5 mm.

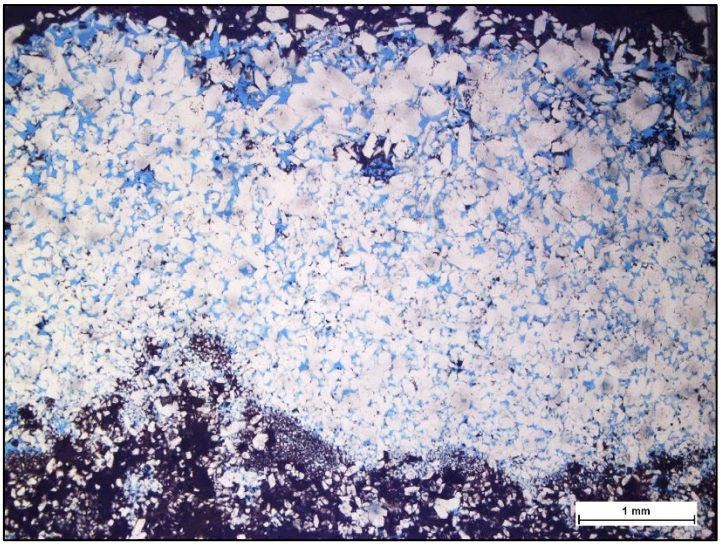

Figure 3.15. Closeup of a gypsum lamina which shows inverse grading (1LFP).

Interpretation

The gypsum in the top part of this thin section contains all characteristics that point to a primary, synsedimentary origin. The gypsum-dolomite couplets can be interpreted as annual cycles of dolomite formation during conditions with relatively low salinity (during the wet season), followed by gypsum formation during evaporative conditions. The reverse grading is the result of crystal overgrowth when salinity increases during the dry season (Gibert et al., 2007).

The wavy character of the laminae is consistent with the hypothesis that the gypsum in the thin section was formed as part of a microbial mat. Comparable modern analogues were described by Aref and Taj (2013) from solar salt works in Egypt, showing that microbial mats that formed under hypersaline conditions are laminated and consist of microbial mat-gypsum couplets.

The gypsum in the lower part is more consistent with diagenetic gypsum growth, since most gypsum crystals are enclosed in a dolomite matrix. The high density of gypsum crystals indicates that these crystals formed during a transition period from diagenetic growth in interstitial waters to primary precipitation from the lake brine.

3.1.7. 2LFP

Description

This thin section (Figure 3.16) consists of a patch of dolomite at the bottom around which multiple laminae of pure gypsum interspersed with thin dolomite laminae are warped. The upper part of the thin section consists of gypsum crystals in a dolomite matrix, with occasional patches of pure gypsum. In this part, gypsum crystals vary strongly in size between 30 and 600 µm. Gypsum crystals in the lower part show a reverse grading (Figure 3.17), both with each lamina as well as over multiple laminae, until they reach a maximum size of 2 mm.

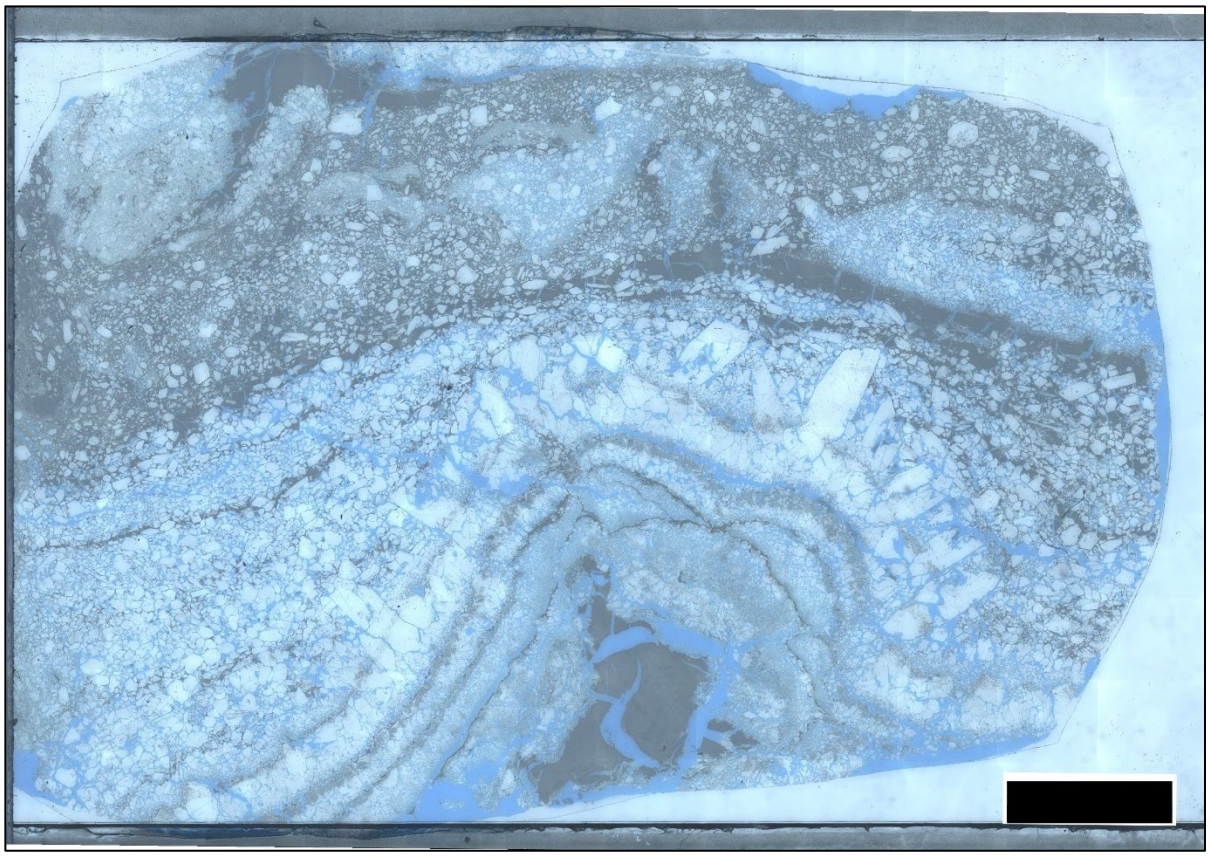

Figure 3.16. Thin section of 2LFP. Scale bar is 5 mm.

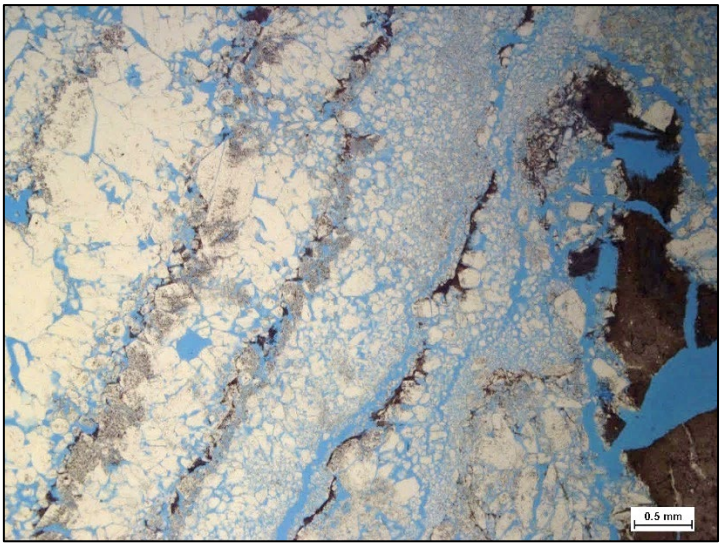

Figure 3.17. Closeup of multiple gypsum laminae showing reverse grading.

Interpretation

The characteristics of this thin section are very similar to those of 1LFP. The bottom part is more strongly curved, but this is very well possible when the gypsum-dolomite couplets formed as a part of a microbial mat (Aref & Taj, 2013).

3.1.8. 3LFP

Description

The gypsum in this thin section (Figure 3.18) does not form clear and distinct laminae, except at the very bottom of the thin section. The gypsum crystals in that lamina are spherical and sometimes rounded and range between 40 and 120 μm in size. Most other gypsum crystals are to be found in the middle of the thin section, although they can be find throughout the entire thin section, where they are embedded in dolomite. A remarkable characteristic of these gypsum crystals is that most of them are elongated tabular-lenticular or lenticular crystals, most of them between 400 and 700 μm. Some of these are covered by black dots (Figure 3.19).

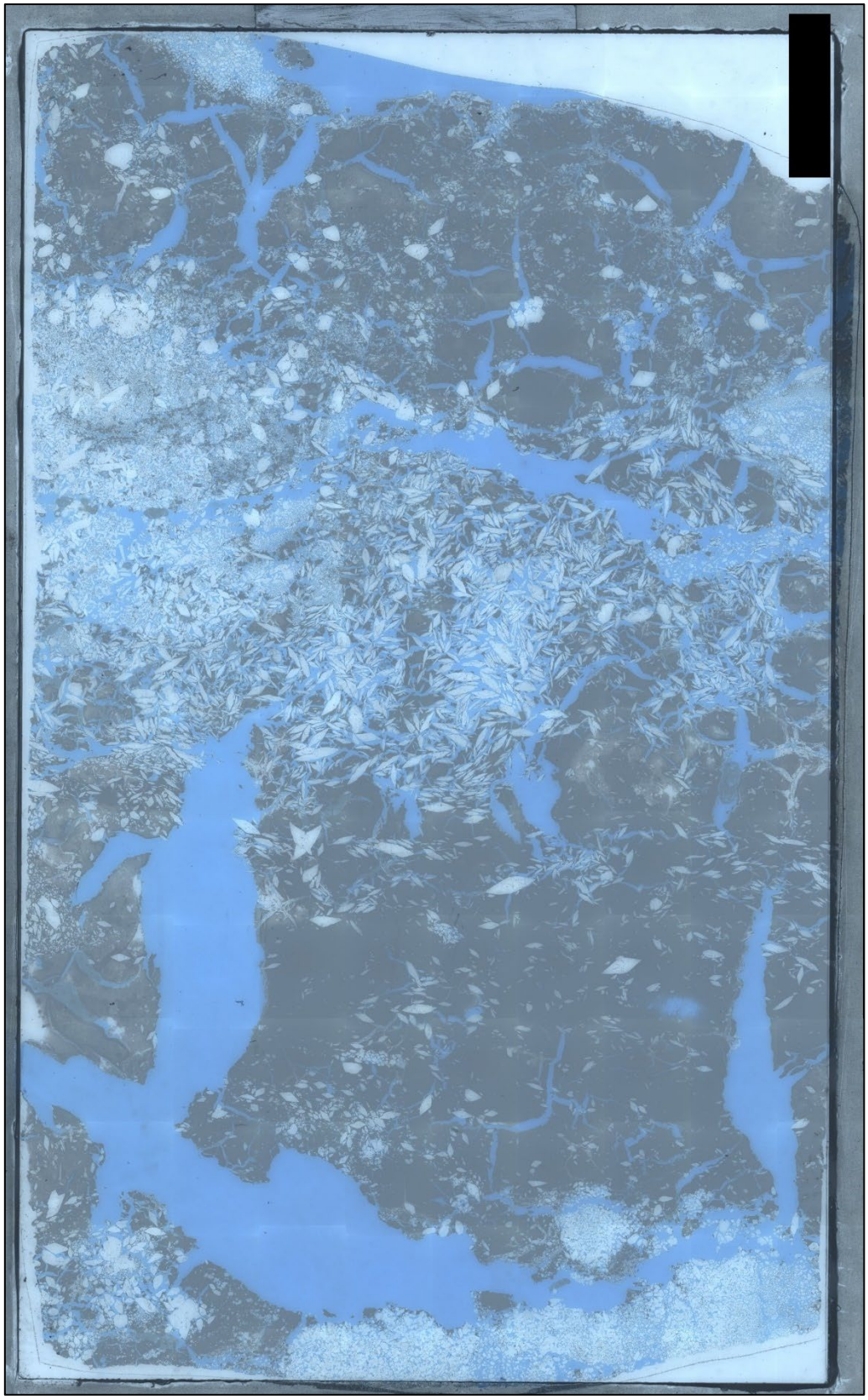

Figure 3.18. Thin section of 3LFP. Scale bar is 5 mm.

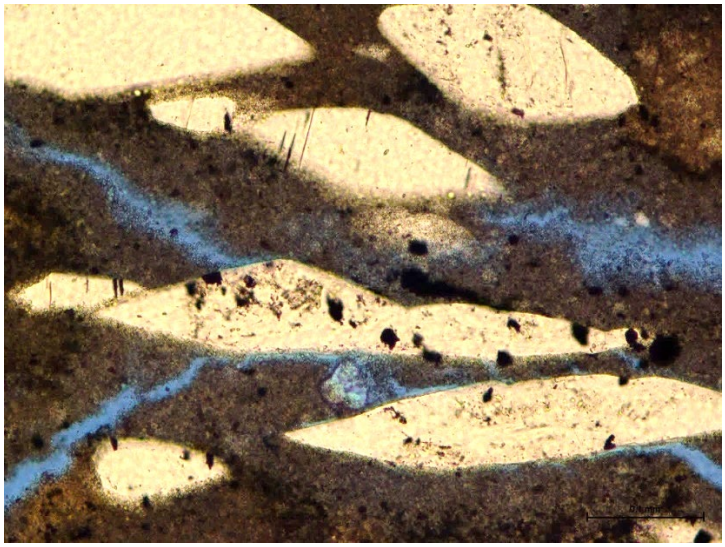

Figure 3.19. Closeup of lenticular gypsum crystals, covered by black dots, in a dolomite matrix (3LFP).

Interpretation

This is probably the only thin section from Las Latas in which the gypsum is best to be interpreted as diagenetic. The absence of distinguishable laminae and the fact that most crystals are embedded in a dolomite matrix point to this. The lenticular nature of most crystals distinguishes this diagenetic gypsum from the diagenetic gypsum in the samples from Alicante. The black dots are probably organic material, which may have contributed to the formation of lenticular gypsum (Cody, 1979). However, since organic material has been available in both lakes (as is shown by the presence of microbially mediated dolomite), this cannot be the full explanation. Likewise, present-day values of alkalinity do not show that Laguna de Fuente de Piedra is more alkaline than Laguna de Salinas, which could have been an explanation of the difference in morphology (Cody, 1979; Giralt, 1998; Kohfahl et al., 2008).

The most likely explanation for the difference is therefore that the gypsum of Laguna de Fuente de Piedra formed under higher temperatures, something which can stimulate lenticular growth (Cody & Cody, 1988).

3.1.9 4LFP

Description

This thin section (Figure 3.20) consists mostly of thick curved gypsum laminae that are separated by thin dolomite laminae. Within each lamina, there are strong variations in crystal size in which no clear pattern is visible, although there are often patches of crystals with about the same size. In some patches, the crystal size ranges between 20 and 60 μm, whereas other parts consist of tabular-prismatic crystals with sizes up to 700 μm. Within the dolomite that is present at the right side of the thin section, pollen are observable (Figure 3.21). In this region of the thin section, halite crystals are observable as well (Figure 3.22). These are degraded crystals without clear cubic form and growth lines with primary fluid inclusions.

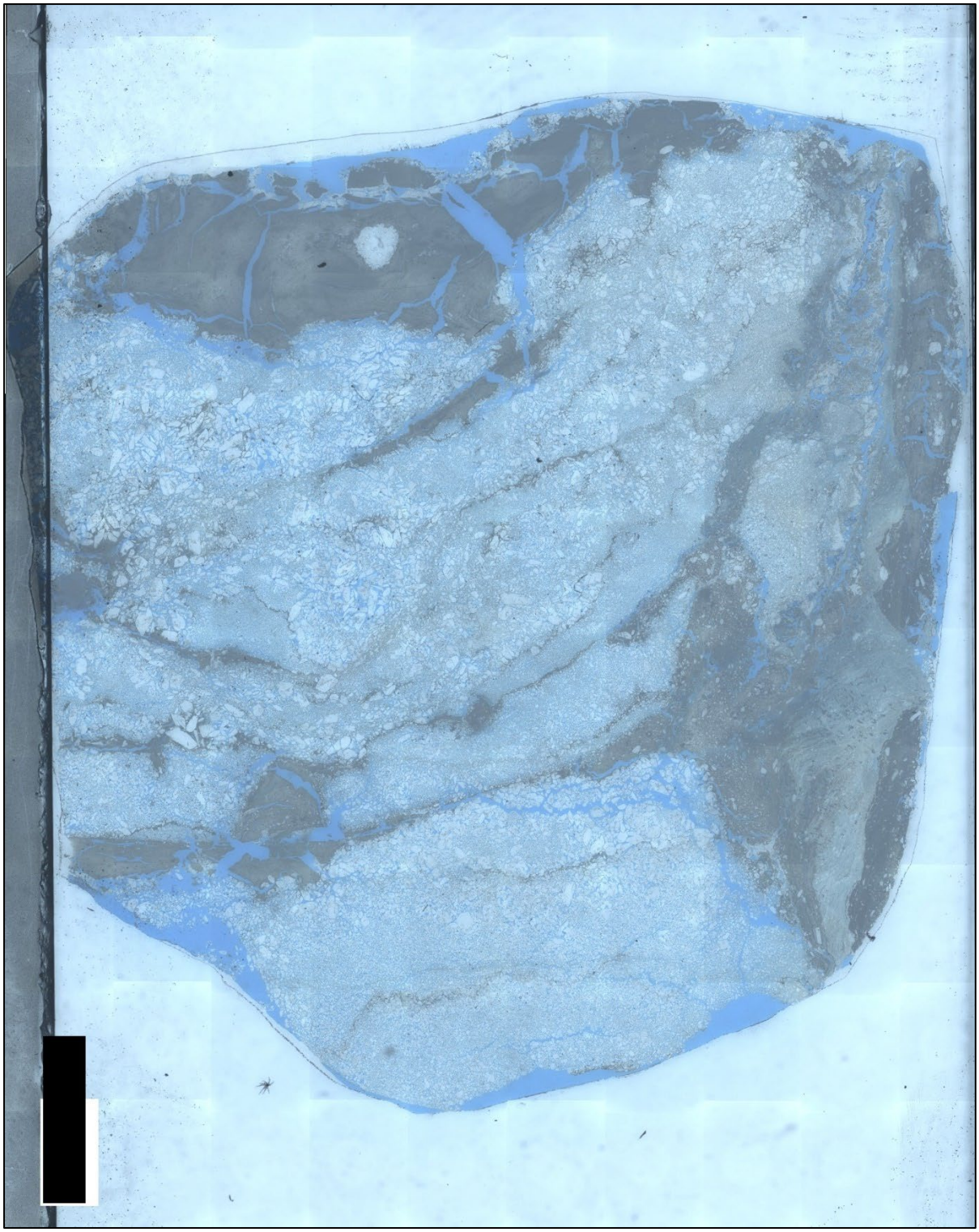

Figure 3.20. Thin section of 4LFP. Scale bar is 5 mm.

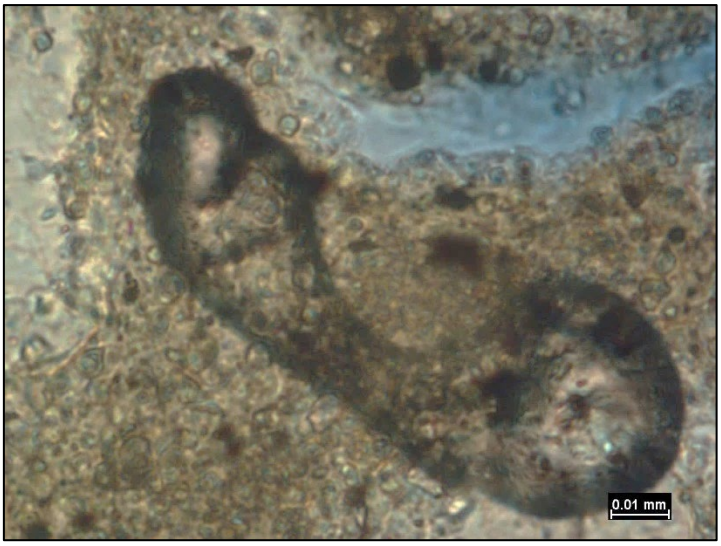

Figure 3.21. Bisaccate pollen in dolomite (4LFP).

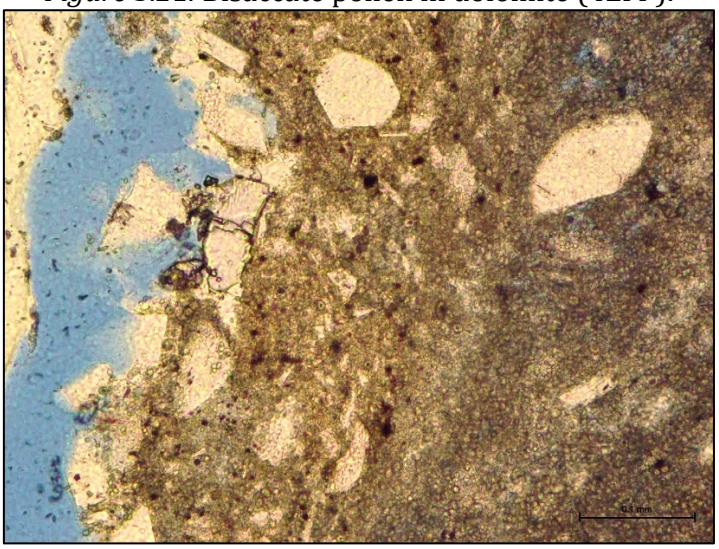

Figure 3.22. Halite crystals, enclosed by dolomite and gypsum (4LFP).

Interpretation

Although the laminae are not as clear as in some other thin sections, they are probably best explained as the result of primary precipitation. The curved nature of the laminae is comparable to 2LFP, leading to the same interpretation that this is the result of an origin as a gypsified microbial mat. The nature of the halite crystals shows that these are not primary precipitates from a brine, but cemented and recrystallized halite, that has precipitated from interstitial waters and been altered by later interactions with groundwater (Hardie et al., 1985). Otherwise, the crystals would have shown the characteristics of primary precipitation mentioned above.

3.1.10. 5LFP

Description

A well-laminated thin section (Figure 3.23) consisting of a lower part of pure gypsum laminae interspersed with dolomite laminae and an upper part in which most gypsum crystals are embedded in a matrix of dolomite. Several laminae show reverse grading.

In the middle of the section, there is one lamina with reverse grading which has relatively large crystals at the top of the lamina (Figure 3.24). On top of this, separated by a very thin dolomite lamina, lies another gypsum lamina with normal grading, having similar large crystals at the bottom of the lamina.

In some cases, horizontal orientation of gypsum crystals is visible, especially in the upper part of the thin section. The larger crystals (up to 1.5 mm) are generally tabular-prismatic and elongated. At some horizons, lenticular crystals are abundant.

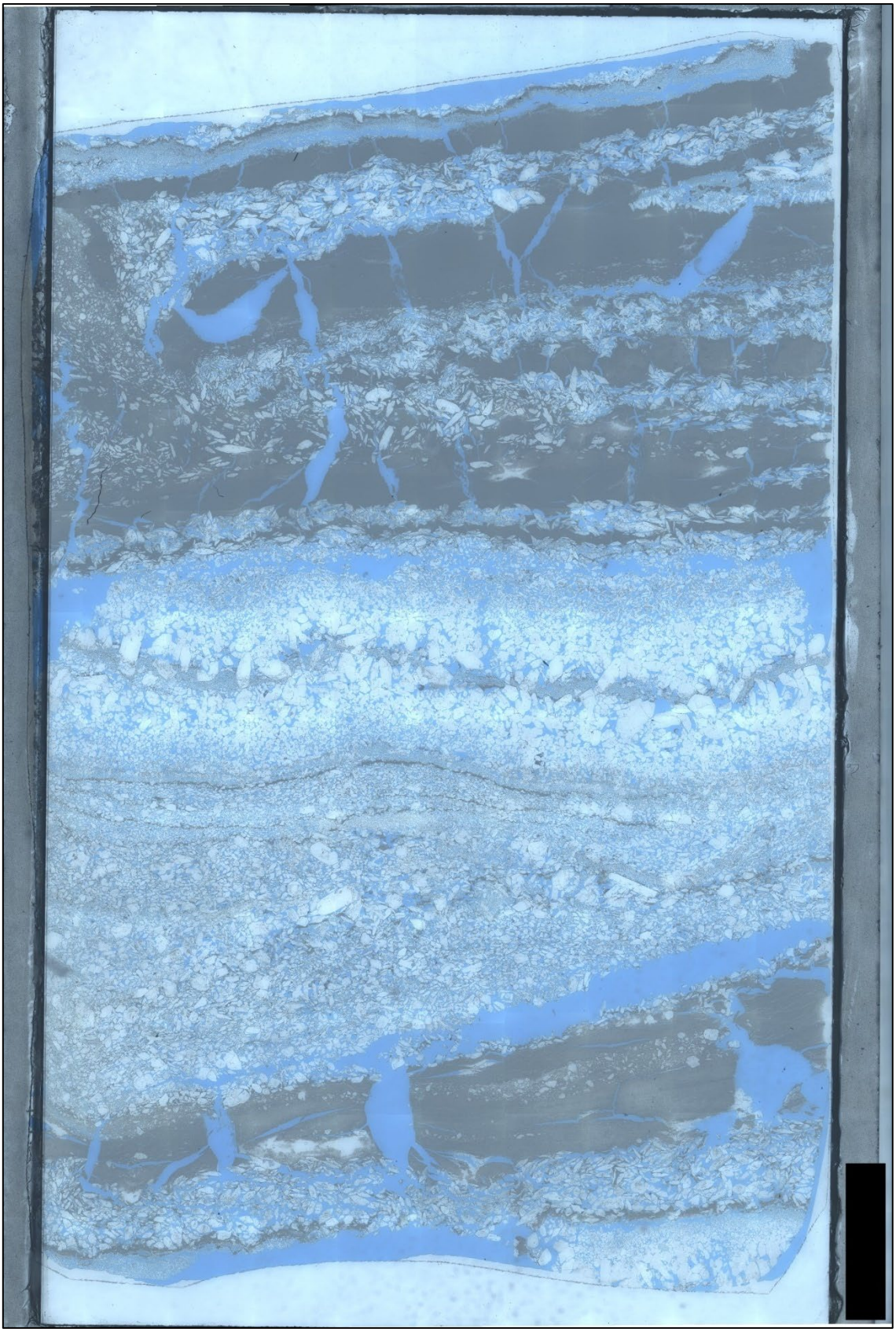

Figure 3.23. Thin section of 5LFP. Scale bar is 5 mm.

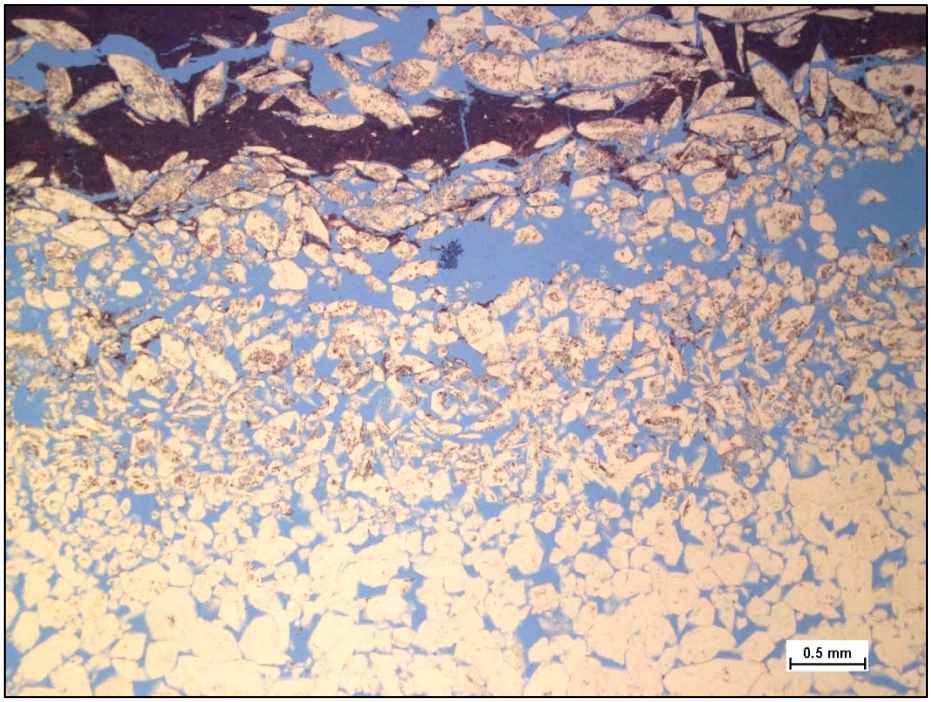

Figure 3.24. Gypsum lamina with normal grading (5LFP).

Interpretation

This thin section is very similar to 1LFP, and therefore the same interpretation is to be given. The only characteristic which is unique to this thin section is the presence of a normally graded lamina. Normal grading is normally interpreted as the result of clastic sedimentation (Bąbel, 1999; Gibert et al., 2007), but given the similarity to the other laminae and the absence of other sedimentary features, a chemical origin is more likely. Ortí et al. (2014a) interpret normal grading as the precipitation of gypsum at the end of the dry period, which would indicate that the lamina formed under slightly more humid conditions, when the lake did not desiccate.

3.2. SEM-EDS

To determine the nature of the black stripes and spots that were present on some gypsum crystals in the thin section of 2ALI (3.1.2, Figure 3.5), SEM-EDS was performed. Figure 3.25

shows the SEM picture of an area of the sample which consists of gypsum. Figure 3.26 shows the accompanying EDS spectrum. Table 3.1 lists the percentages of elements and oxides that are present in the spectrum as calculated by the EDS software. The spectrum shows that the targeted area consists primarily of oxygen, calcium and sulphur, with minor amounts of silicon and aluminium. This is consistent with gypsum as the dominant mineral, with siliciclastic minerals as minor constituents.

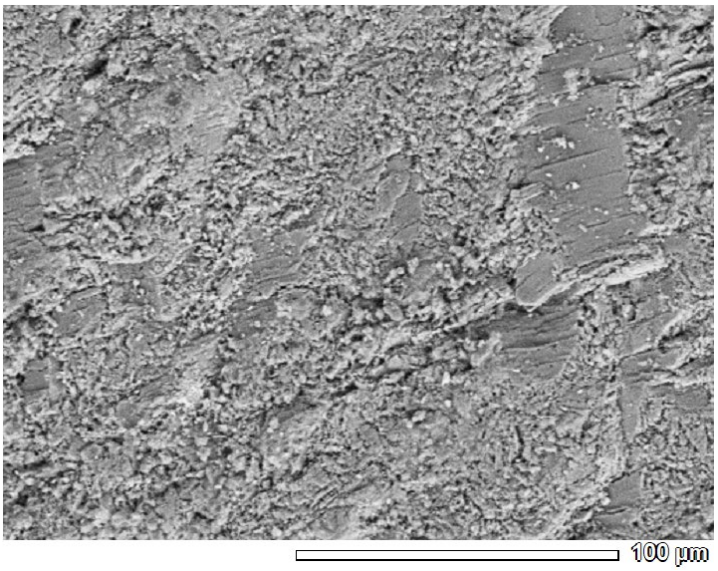

Figure 3.25. SEM picture of gypsum.

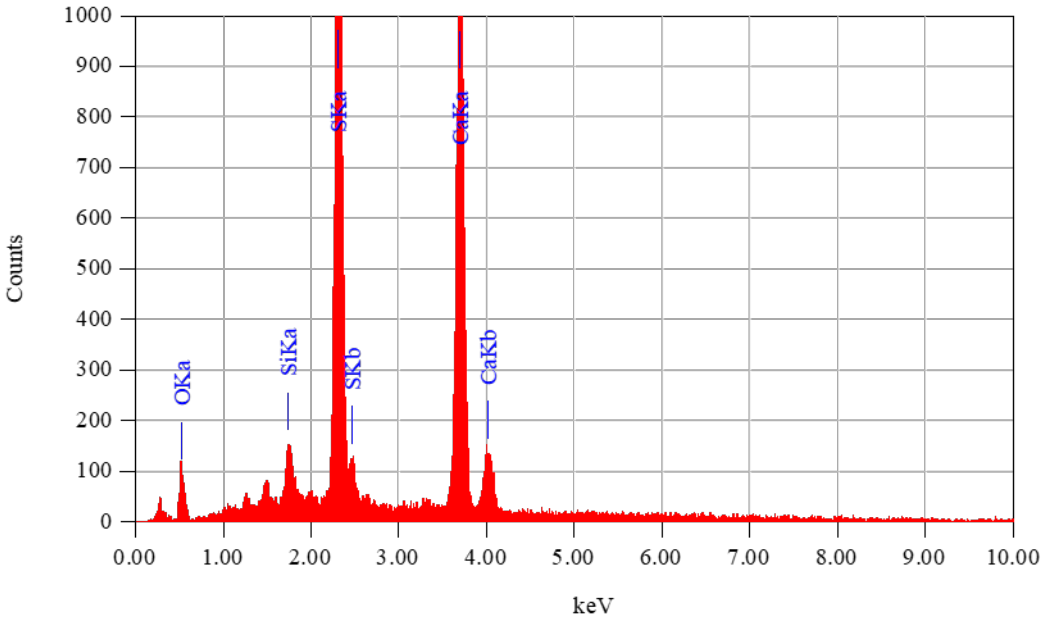

Figure 3.26. EDS spectrum accompanying Figure 3.25.

Table 3.1. Percentages of elements and oxides as calculated by the EDS software from the spectrum of Figure 3.26.

Element	(keV)	Mass%	Sigma	Mol%	Compound	Mass%	Cation	K
O		46.9						
Ca K	3.69	25.7	0.74	43.13	CaO	35.96	5.25	55.0457
S K	2.307	17.34	0.84	36.38	SO_3	43.3	4.43	31.6737
Si K	1.739	6.93	0.6	16.59	SiO_2	14.82	2.02	9.73
Al K	1.486	3.13	0.42	3.9	Al_2O_3	5.91	0.95	3.5505
Total		100		100		100	12.65	

Figure 3.27 shows an area on the section that contains dolomite and Figure 3.28 shows the accompanying spectrum. Table 3.2 lists the percentages of elements and oxides that are present in the spectrum as calculated by the EDS software. The spectrum shows a high amount of silicon, as well as calcium and magnesium, the two cations of dolomite. Sodium, potassium and chloride are present as well. This indicates that the dolomite sediment contains significant amounts of siliciclastic material. The presence of sodium and chloride can be interpreted as cemented halite, as was found in the thin section of 4LFP (3.1.9, Figure 3.22).

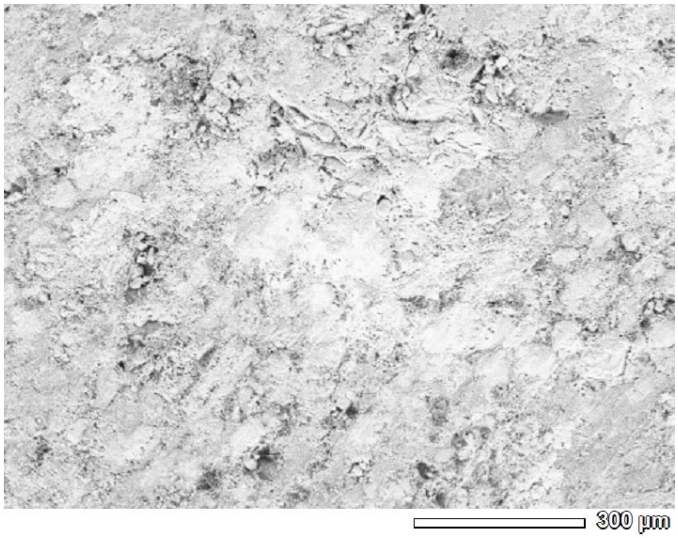

Figure 3.27. SEM picture of dolomite.

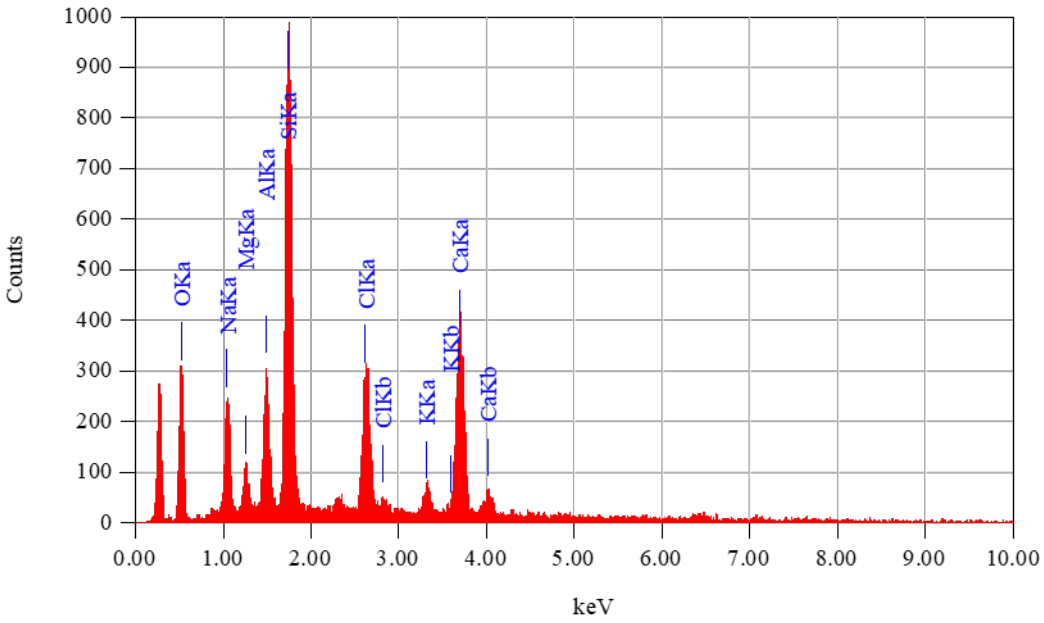

Figure 3.28. EDS spectrum accompanying Figure 3.28.

Table 3.2. Percentages of elements and oxides as calculated by the EDS software from the spectrum of Figure 3.28.

Element	**(keV)**	**Mass%**	**Sigma**	**Mol%**	**Compound**	**Mass%**	**Cation**	**K**
O	38.93							
Si K	1.739	20.6	0.55	42.49	SiO_2	44.08	7.24	29.9447
Ca K	3.69	14.42	0.32	20.84	CaO	20.18	3.55	33.2314
Na K	1.041	7.76	0.25	9.77	Na_2O	10.46	3.33	7.6908
Al K	1.486	5.6	0.28	6.01	Al_2O_3	10.59	2.05	6.8253
Mg K	1.253	2.48	0.2	5.91	MgO	4.11	1.01	2.3757
K K	3.312	1.89	0.11	1.4	K_2O	2.28	0.48	4.0135
Cl K	2.621	8.31	0.15	13.57	Cl	8.31	0	15.9186
Total		100		100		100	17.64	

Figure 3.29 shows an area on the section that contains dolomite and Figure 3.30 shows the accompanying spectrum. The picture has been distorted by electromagnetic interference. Table 3.3 lists the percentages of elements and oxides that are present in the spectrum as calculated by the EDS software. The spectrum is most consistent with the mineral glauberite ($Na_2Ca(SO_4)_2$).

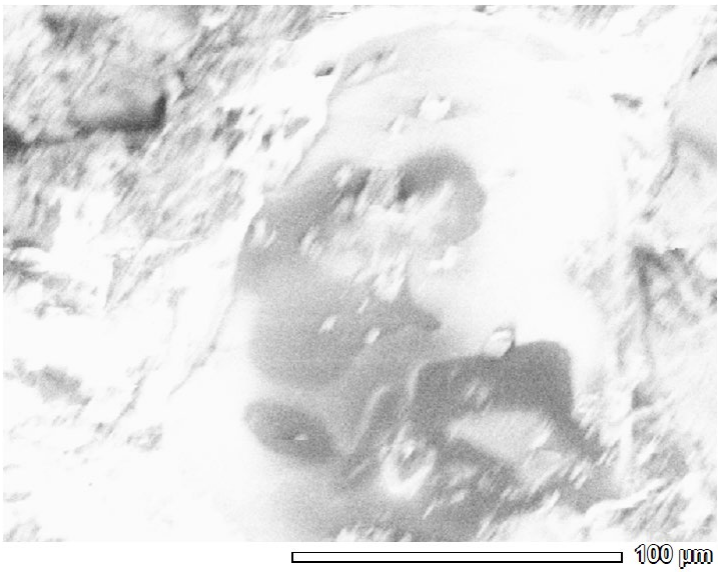

Figure 3.29. SEM picture of a dark spot.

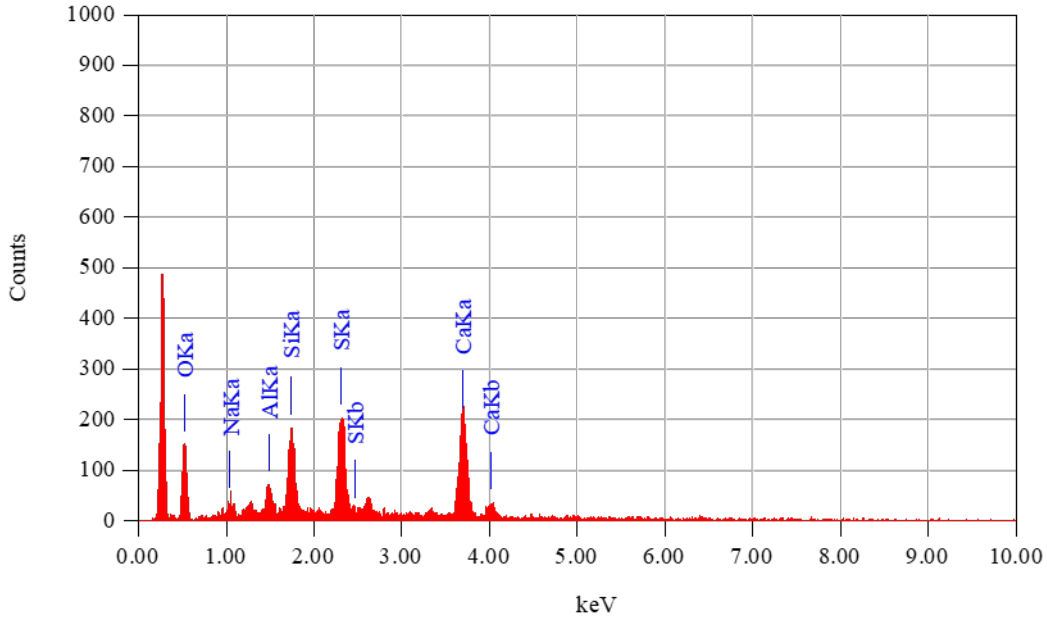

Figure 3.30. EDS spectrum accompanying Figure 3.29.

Table 3.3. Percentages of elements and oxides as calculated by the EDS software from the spectrum of Figure 3.30.

Element	**(keV)**	**Mass%**	**Sigma**	**Mol%**	**Compound**	**Mass%**	**Cation**	**K**
O		46.37						
Ca K	3.69	21.8	0.66	36.22	CaO	30.5	4.5	50.4752
S K	2.307	14.42	0.77	29.96	SO_3	36.02	3.73	27.0763
Si K	1.739	10.17	0.68	24.12	SiO_2	21.76	3	15.0903
Na K	1.041	3.6	0.36	5.22	Na_2O	4.86	1.3	2.9829
Al K	1.486	3.63	0.42	4.48	Al_2O_3	6.87	1.12	4.3753
Total		100		100		100	13.64	

3.3. Elemental analysis

Table 3.4 shows the concentrations of 14 elements that were measured on the ten samples from the cores. Table 3.5 shows the concentrations of the same elements as measured in five standards during the same run. An absent value means that the concentration was too low to be measured. In the case of Mg, Ca, Si and Sr, all ten samples contained measurable concentrations of these elements. In the case of Al, Fe, Mn, Cu, Zn, Ni and Mo, some samples has measurable concentrations of these elements and some had not. In the case of Cr, Cd and V, none of the samples had concentrations above the detection limit.

For all elements that were measured in samples from both cores (Mg, Ca, Si, Al, Fe, Mn, Sr, Cu and Zn), the average concentrations from both cores are in the same order of magnitude. Compared to the average concentrations of the samples from Alicante, the Las Latas samples have average concentrations that are between 46 percent lower and 114 percent higher. The strongest differences between the two cores are present in the range of concentrations of Si (Alicante: 181 to 329 ppm; Las Latas: 52 to 254 ppm) and Mn (Alicante: not detectable to 14 ppm; Las Latas: 12 to 21 ppm).

Table 3.4. Concentrations of elements in samples as measured by ICP-OES.

Sample	**Mg**	**Ca**	**Si**	**Al**	**Fe**	**Mn**	**Sr**
(Wavelength)	**280.27**	**317.933**	**288.158**	**396.152**	**238.204**	**259.372**	**421.552**
1ALI	3002	249667	230	81.7	21.5	13.4	278
2ALI	4010	223006	223	75.8			1557
3ALI	4494	224574	329	69.7			1376
4ALI	35244	45260	182		11.3		4821
5ALI	11824	170729	281	43.0		3.5	1391
1LFP	12937	177886	52.3	61.9	33.8	18.6	2577
2LFP	5452	229177	114	55.8		12.1	2687
3LFP	13315	196991	254	56.3	4.3	14.6	2014
4LFP	7810	219985	154	97.5	88.8	20.5	1030
5LFP	9856	108734	95.1	57.4	13.8	18.0	1617
Sample	**Cu**	**Cr**	**Zn**	**Cd**	**Ni**	**V**	**Mo**
(Wavelength)	**327.395**	**205.56**	**206.2**	**214.439**	**216.555**	**292.401**	**204.598**
1ALI	9.6				104		
2ALI							
3ALI							
4ALI			4.4				188
5ALI							
1LFP	8.9						
2LFP			5.7				
3LFP							
4LFP							
5LFP							

Table 3.5. Concentrations of elements in standards as measured by ICP-OES.

Sample	**Mg**	**Ca**	**Si**	**Al**	**Fe**	**Mn**	**Sr**
(Wavelength)	**280.27**	**317.933**	**288.158**	**396.152**	**238.204**	**259.372**	**421.552**
88b_a	130229	220331	642	489	1800	124	65
88b_b	130089	220024	635	490	1793	124	65
CRM_512	145001	251648	1225	198	154	28	232
CRM_513	981	331781	475	465	130	61	117
JDo_a	117950	252395	95	105	129	49	124
Sample	**Cu**	**Cr**	**Zn**	**Cd**	**Ni**	**V**	**Mo**
(Wavelength)	**327.395**	**205.56**	**206.2**	**214.439**	**216.555**	**292.401**	**204.598**
88b_a					11.9		
88b_b	5.4		11.9				
CRM_512			13.0				
CRM_513				2.9			
JDo_a			43.1				

The results could further be compared to ICP-OES measurements on dolomite samples from both cores. A comparison between the dolomite samples and gypsum samples from both Alicante and Las Latas is presented in Figure 3.31. The figure shows that Mg, Fe and Mn

concentrations in dolomite are higher than in gypsum, whereas the concentration of Sr is higher in gypsum than in dolomite, although in the case of Alicante, there is significant overlap (444 ± 316 ppm in dolomite vs. 1885 ± 1537 ppm in gypsum). The concentrations of Ca are overlapping.

For Alicante, Si and Al concentrations were available as well. The average concentration of Si in the eight dolomite samples of which the data could be used is 952 ± 516 ppm, and the average concentration of Al is 470 ± 168 ppm. This is significantly higher than the average concentrations of these elements in both the samples from Alicante (Si: 249 ± 51 ppm; Al: 68 ± 15 ppm, plus one sample below detection limit) and Las Latas (Si: 134 ± 68 ppm; Al: 66 ± 16 ppm).

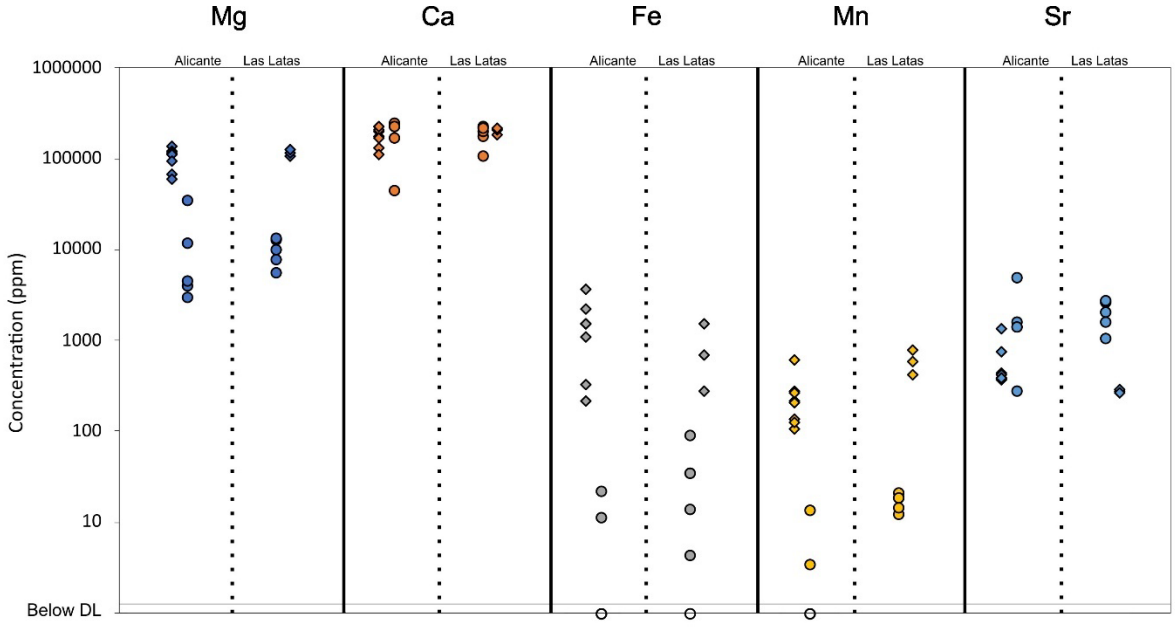

Figure 3.31. Comparison between dolomite (diamonds) and gypsum (circles) samples from Alicante and Las Latas. Open circles indicate samples with concentrations below the detection limit.

When the individual gypsum samples are compared with each other (Figure 3.32), it shows that 4ALI is an outlier among the samples from Alicante. It has much higher Mg and Sr concentrations, and a much lower Ca concentration than the other samples. Moreover, it is the only sample from Alicante in which Zn and Mo were measured (Table 3.4).

Among the samples from Las Latas, 4LFP is an outlier. It has a much higher Fe concentration than the other samples, and the highest Mn concentration as well. It also has the lowest Sr concentration.

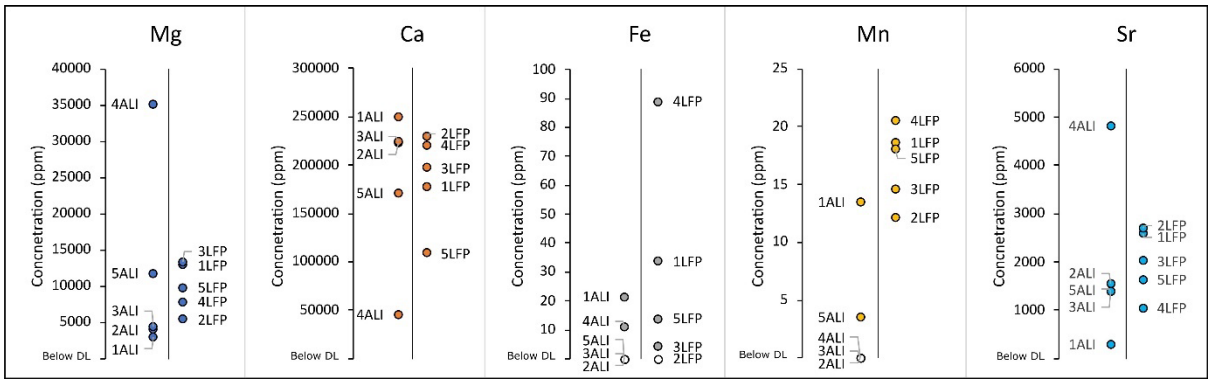

Figure 3.32. ICP-OES results of the five major elements in the samples from Alicante (left side of each graph) and Las Latas (right side of each graph). Open circles indicate samples with concentrations below the detection limit.

3.4. XRF analysis

3.4.1. Indicators of evaporites

It was found that S and S/Fe were the best indicators of the presence of evaporite layers. Figures 3.33 and 3.34 show the fluctuations of this element and element ratio in the representative intervals. In the evaporite intervals from Las Latas, S and S/Fe are almost always higher than in the non-evaporitic intervals. Only in the case of S, there are some small peaks in dark layers (Figure 3.33c), which can be explained by the presence of sulphur in organic matter. Since these dark layers have also relative high amounts of iron, dividing S by Fe leads to the reduction of these peaks (Figure 3.34c).

In the case of the intervals from Alicante, S and S/Fe do not always show peaks in selenite layers, or the peaks are not higher than in the non-evaporitic parts of the core. This means that S and S/Fe are less reliable indicators of the presence or absence of evaporite intervals in the case of Alicante than in the case of Las Latas.

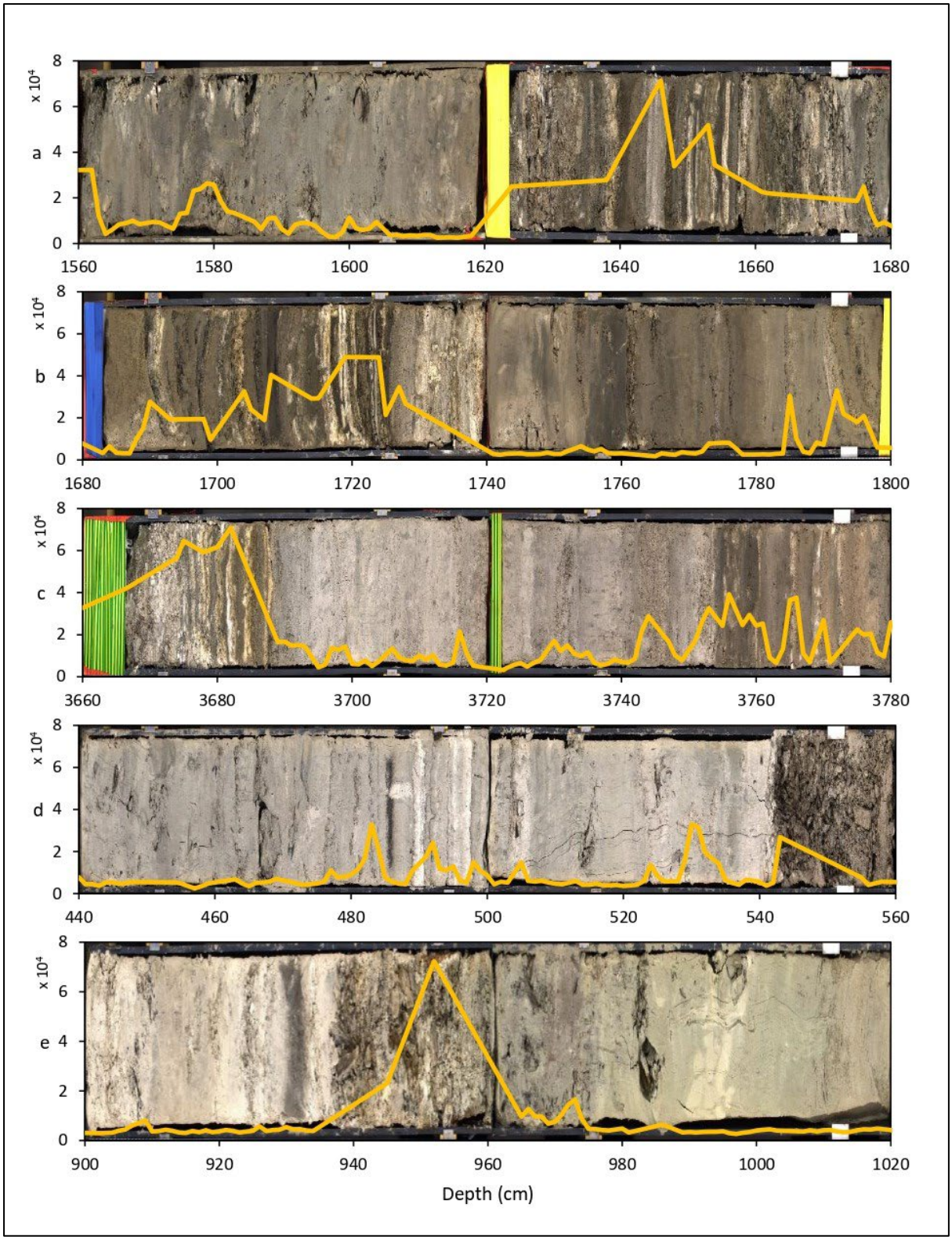

Figure 3.33. Fluctuations in S counts for the five representative intervals from Las Latas (a – c) and Alicante (d – e).

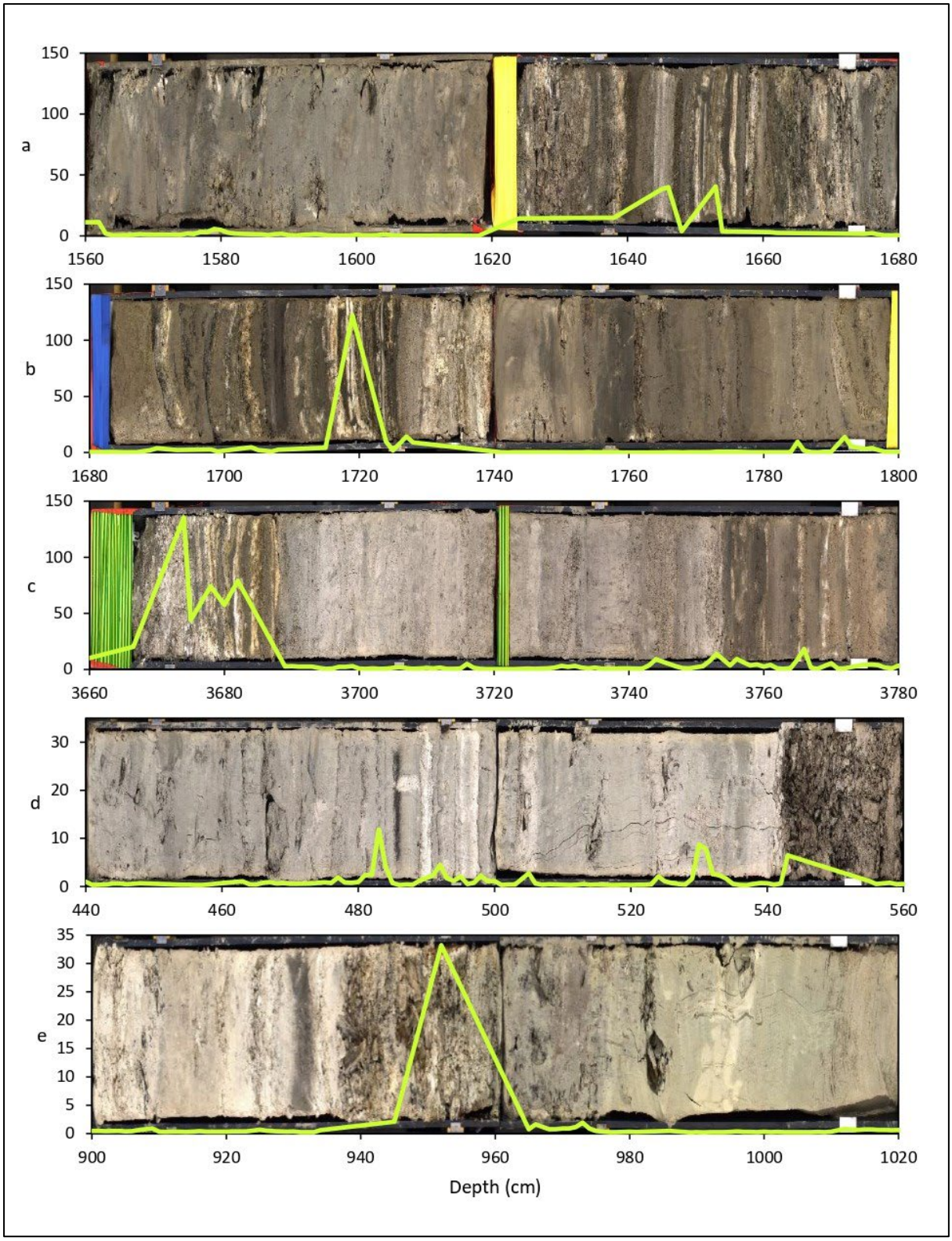

Figure 3.34. Fluctuations in S/Fe for the five representative intervals from Las Latas (a – c) and Alicante (d – e).

In Figure 3.35 and Figure 3.36, S and S/Fe are plotted on top of the stacked pictures of the Alicante and Las Latas cores and compared with the stratigraphy of these cores. In both cases, most of the evaporite layers are captured well by peaks in S and S/Fe. In the case of Alicante, additional peaks are present between 200 and 540 cm, which corresponds to the laminated interval (2.2.1, Figure 2.4). Likewise, the peaks around 2430 cm correspond to a laminated interval. The relationship between lamination and S and S/Fe peaks is also evident from the core pictures, which show an absence of peaks in the most homogeneous intervals, e.g. between 2200 and 2320 cm.

In the case of Las Latas, the relationship between individual evaporite layers and peaks in S and S/Fe is less easy to determine from Figure 3.36, because of the abundance of both evaporite laminae and peaks in some intervals. However, S and S/Fe show the same general pattern as the evaporite layers, i.e. the gradual decline in frequency from the bottom to the top of the core, and the occurrence in irregular bundles. The white evaporite layers give the intervals in which they occur a brighter appearance. Therefore, there is a visual negative correlation between dark layers and peaks in S and S/Fe.

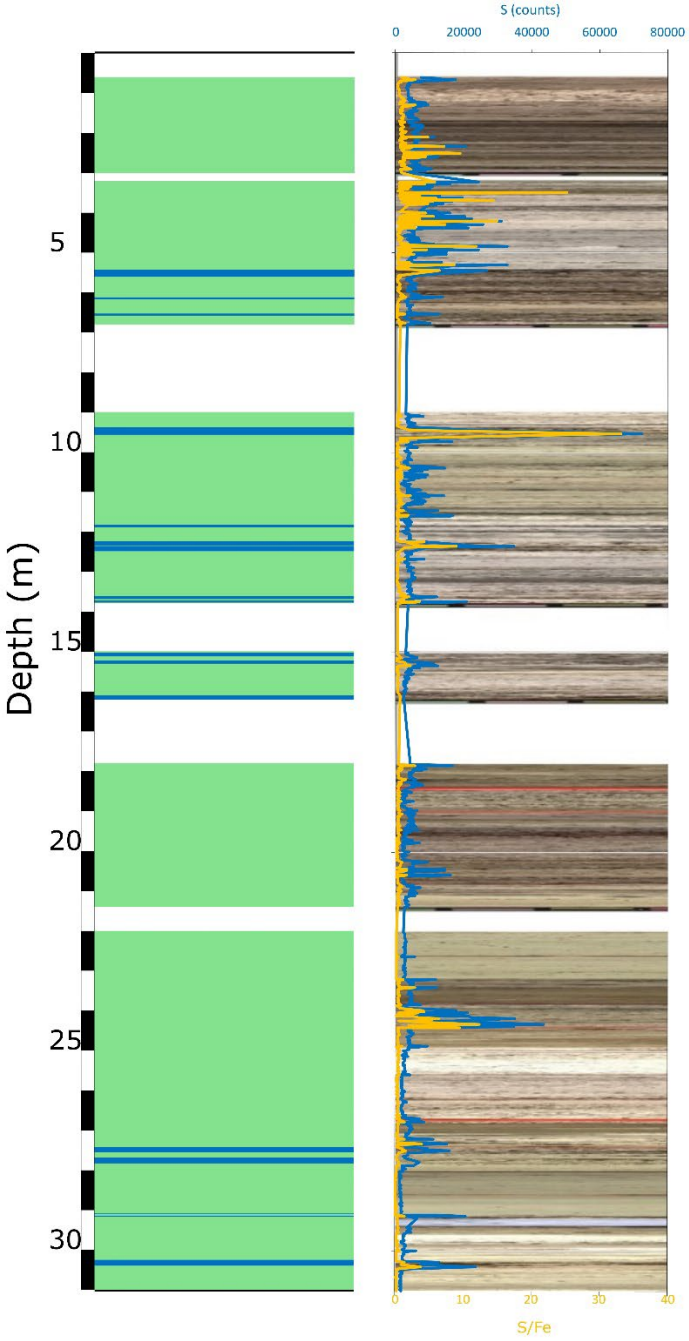

Figure 3.35. Stratigraphy of Salinas-3 (left) and S and S/Fe plotted on the stack of pictures from Salinas-3 (right).

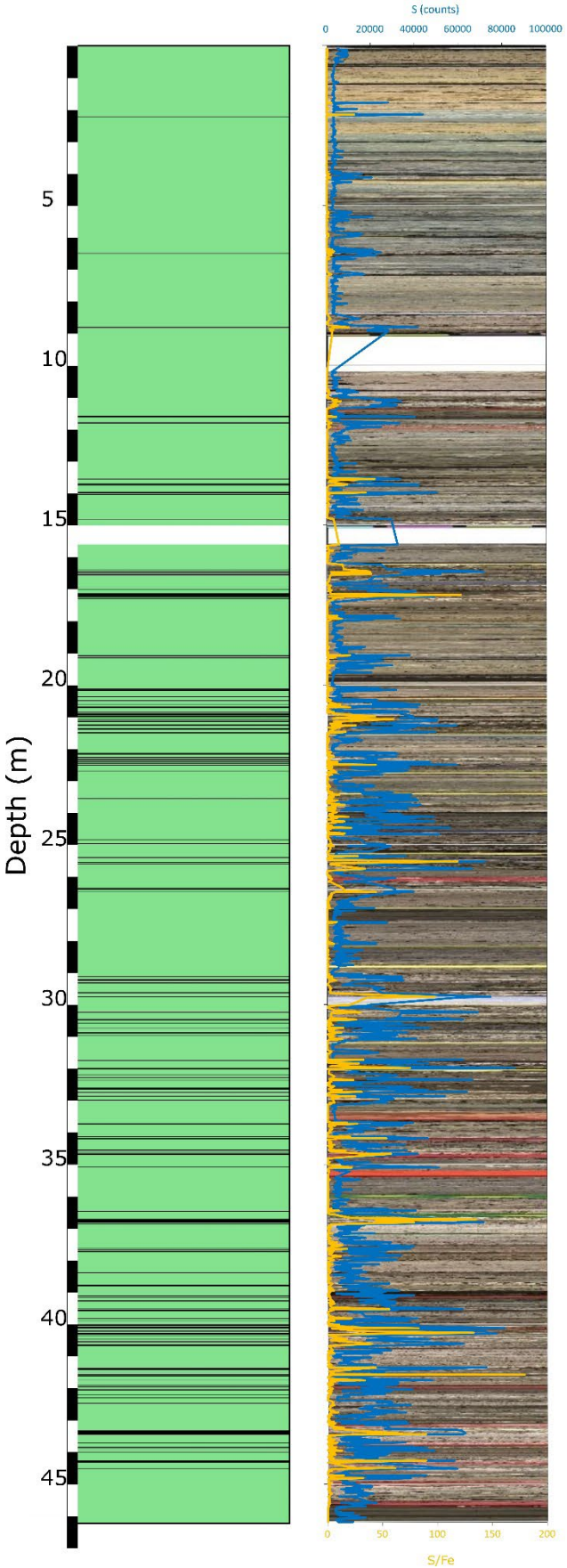

Figure 3.36. Stratigraphy of Las Latas-1 (left) and S and S/Fe plotted on the stack of pictures from Las Latas-1 (right).

3.4.2. Comparison between elements and element ratios

In Figures 3.37 to 3.40, the elements and element ratios are compared with each other and with the presence of evaporite layers. For Alicante, Figure 3.37 shows the fluctuations in twelve elements and Figure 3.38 the fluctuations in eight element ratios. Figure 3.39 shows the twelve elements for Las Latas and Figure 3.40 the element ratios for this core. The correlations between evaporite layers and the elements and element ratios that were analysed will be statistically determined in paragraph 4.1.1.

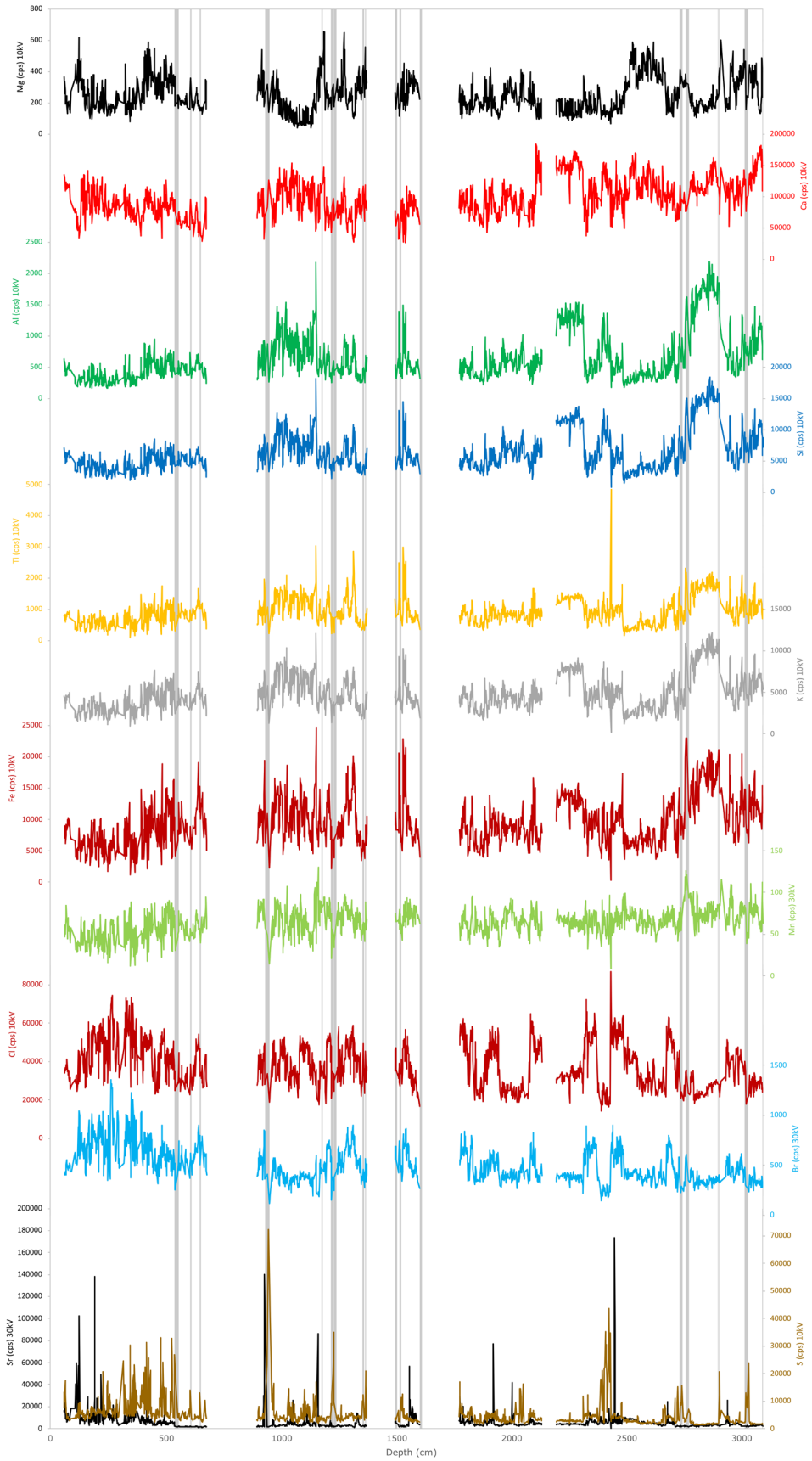

Figure 3.37. XRF measurements of twelve elements (Alicante). Shaded bars indicate selenite layers.

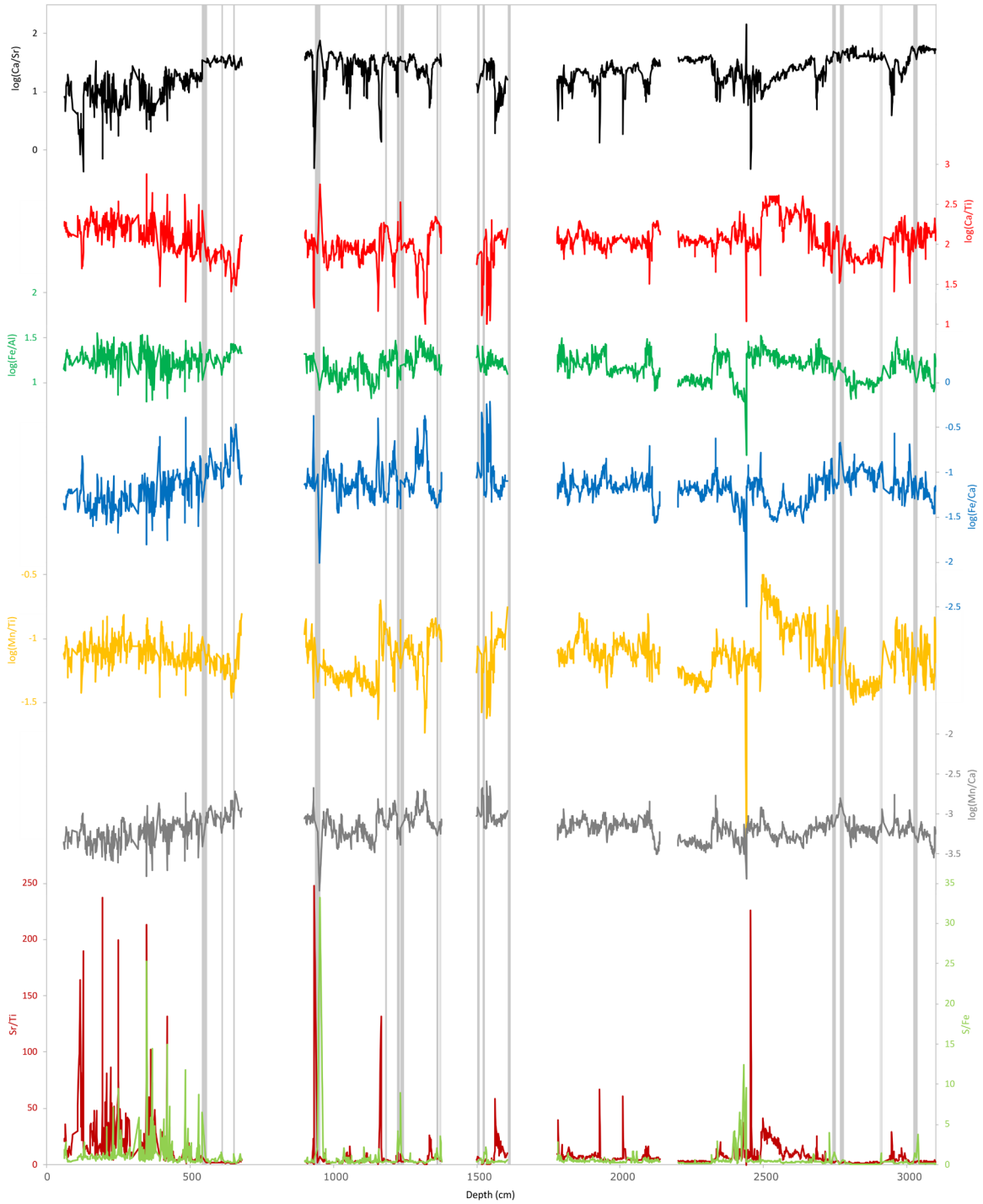

Figure 3.38. Eight element ratios (Alicante). Shaded bars indicate selenite layers.

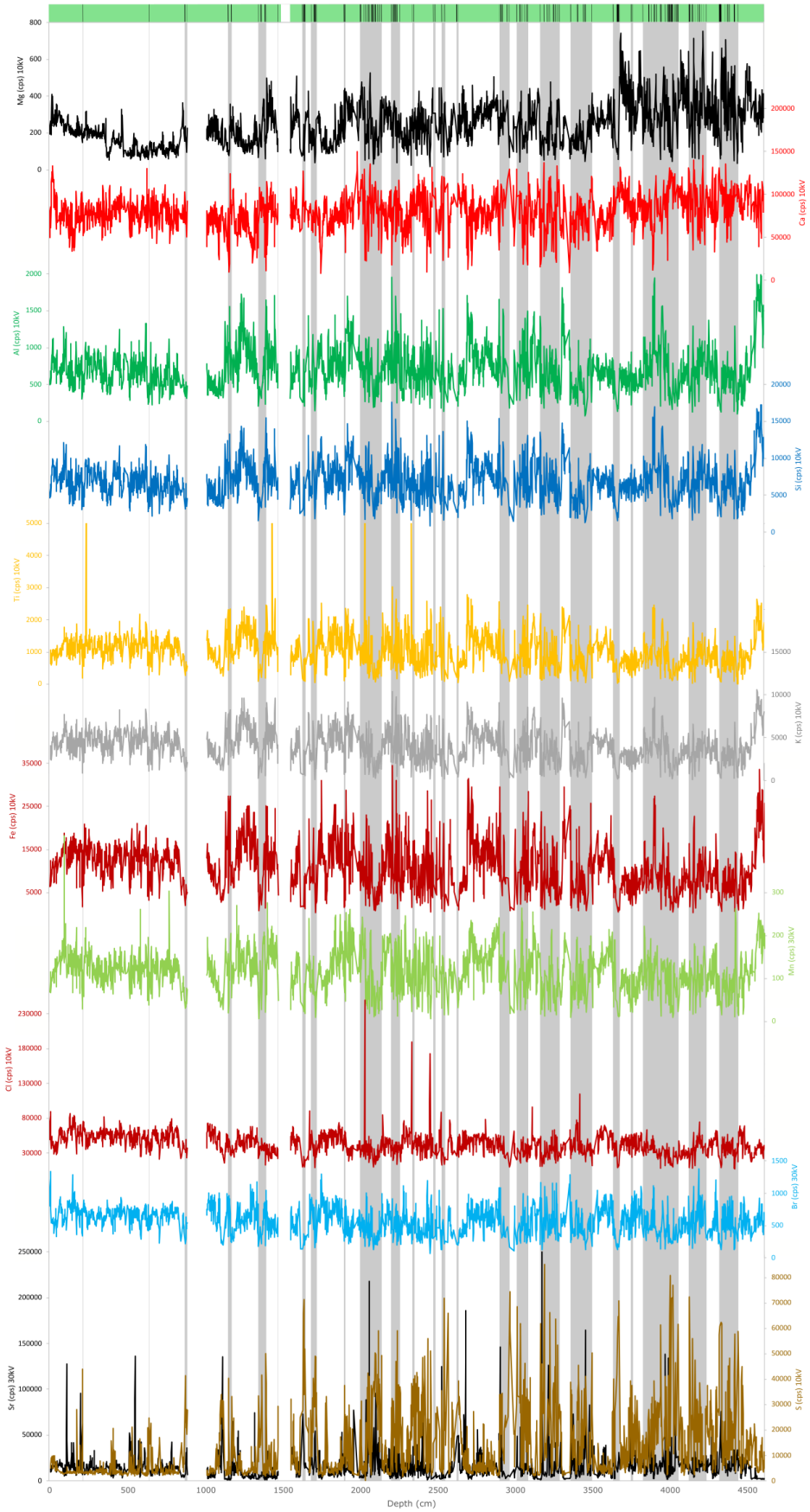

Figure 3.39. XRF measurements of twelve elements (Las Latas). Shaded bars indicate evaporite-rich intervals.

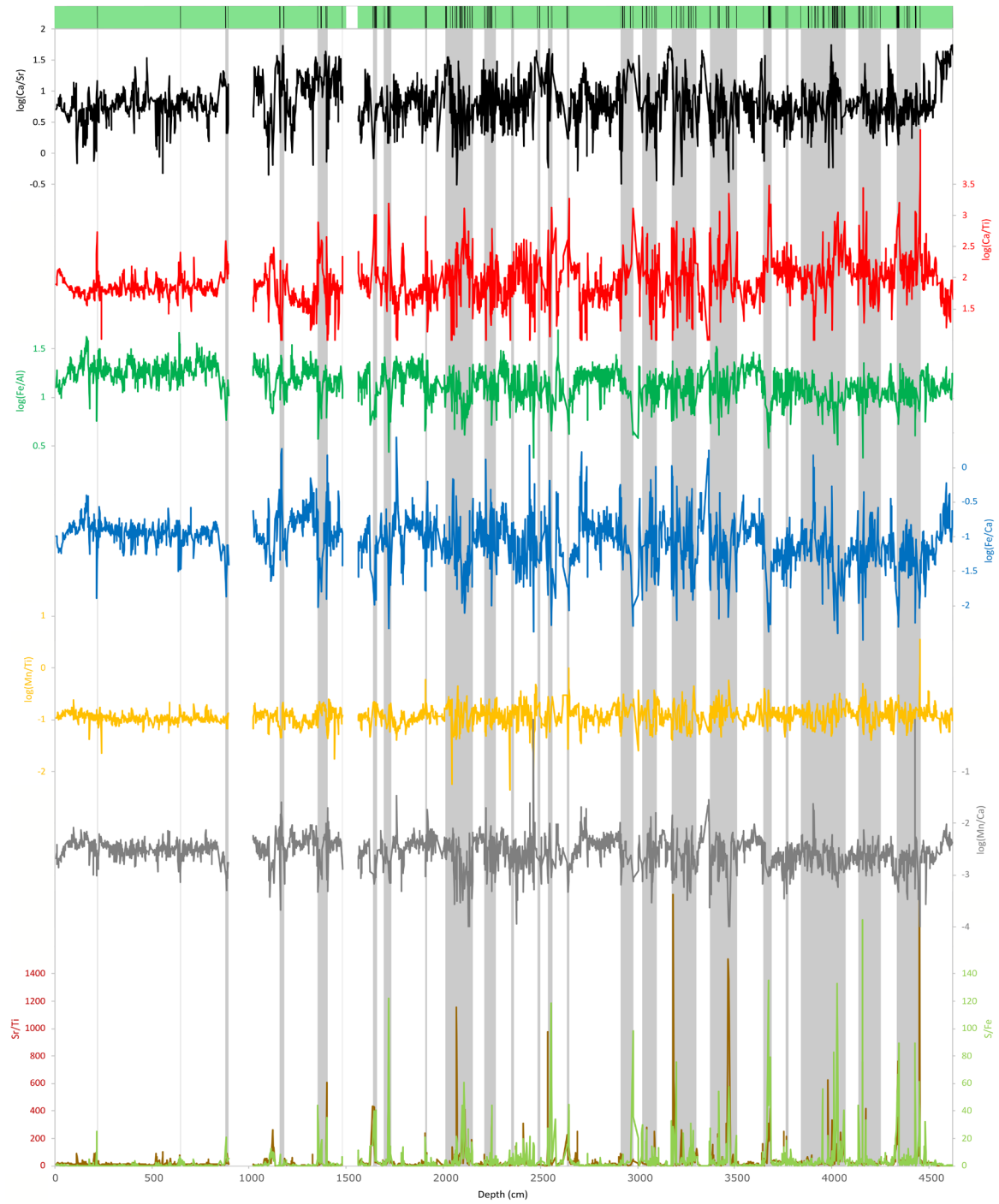

Figure 3.40. Eight element ratios (Las Latas). Shaded bars indicate evaporite-rich intervals.

3.4.3. Principal component analysis

Figure 3.41 shows the principal component analysis (PCA) of the XRF data from Alicante, with the elements included that are most meaningful for paleoenvironmental analysis. The first

component shows a clustering of S, Sr, Mg, Cl, Br and Ca on one side and K, Si, Al, Ti, Fe and Mn on the other side. The second component shows primarily an opposition between Ca on one side and Br and Cl on the other. The third component leads to a clustering of S and Sr one side and Mg, Mn and Ca on the other.

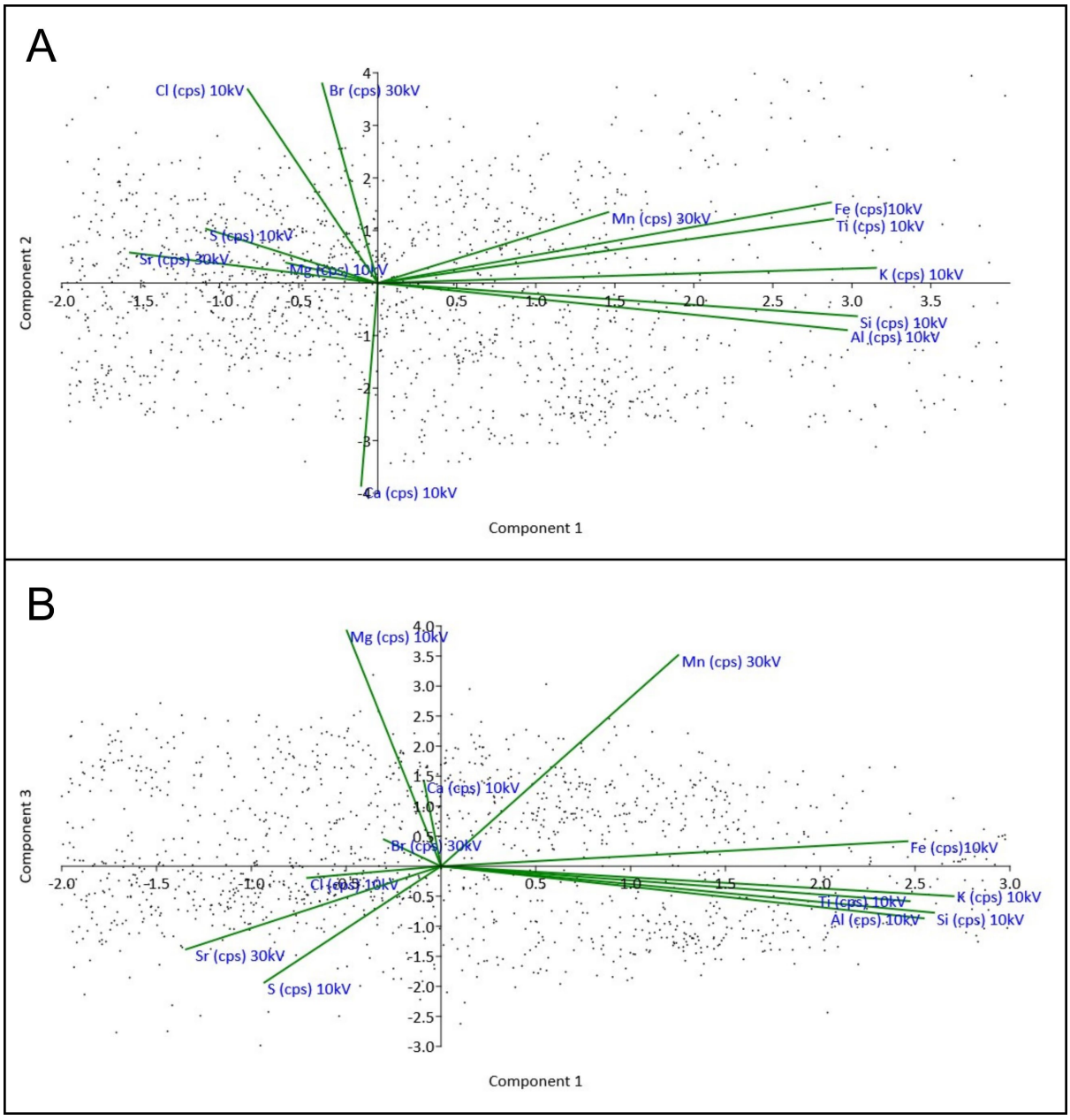

Figure 3.41. Principal component analysis of the XRF data from Alicante. (A) First and second component. (B) First and third component.

Figure 3.42 shows the PCA of Alicante a second time, but with the results of XRD analysis included. In this way, elements can be related to specific minerals. It is shown that dolomite

and Mg cluster on all three axes. However, other clear correlations between elements and minerals are absent, even between Si and quartz (SiO_2) and between S and gypsum ($CaSO_4 \bullet 2H_2O$).

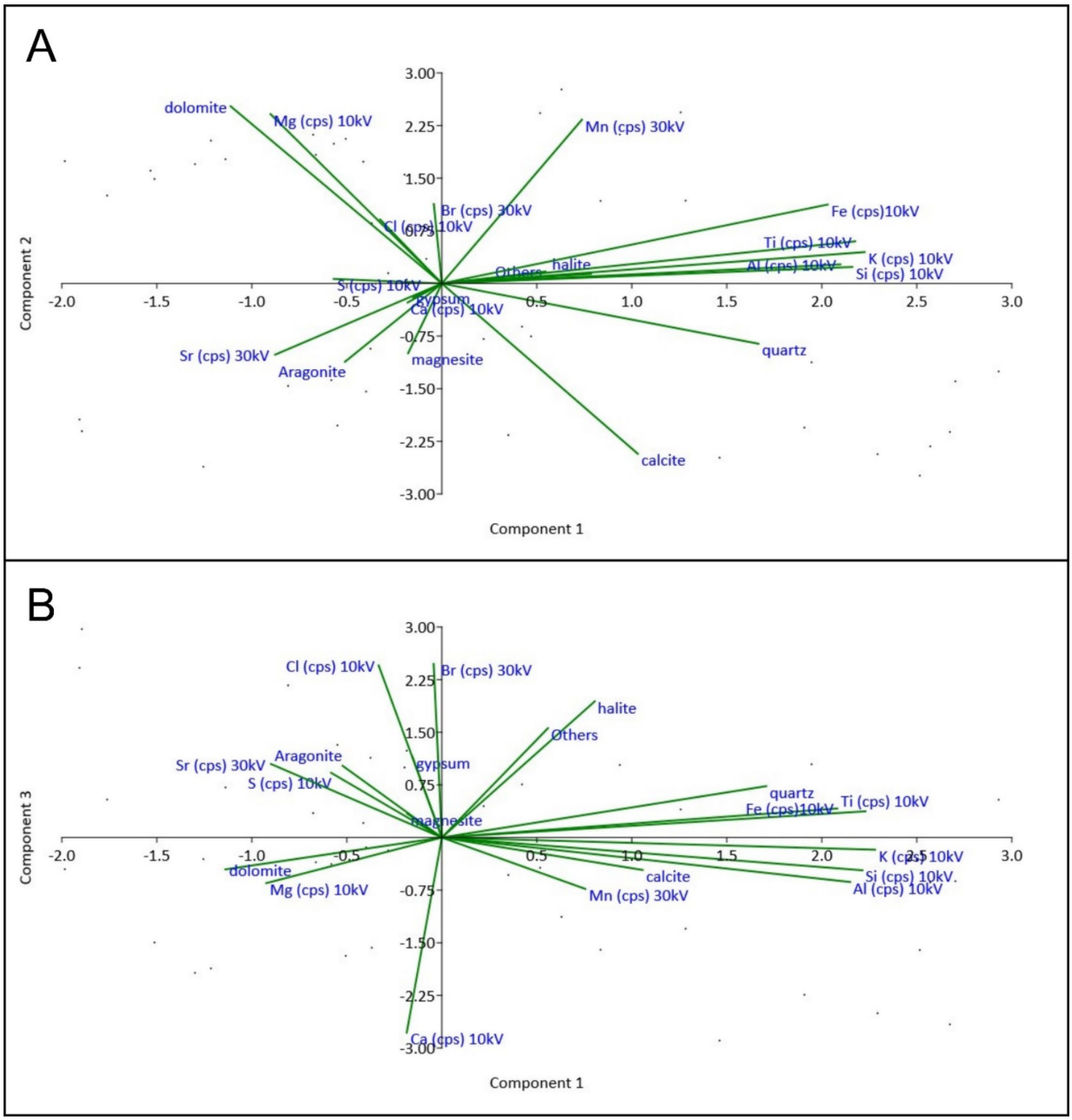

Figure 3.42. Principal component analysis of the XRF and XRD data from Alicante. (A) First and second component. (B) First and third component.

The PCA of Las Latas (Figure 3.43) shows in general the same pattern as in the case of Alicante, with S, Sr, Ca and Mg clustering on one side and most other elements on the other

side in the case of the first component, and a clustering of S and Sr versus Ca and Mg in the case of the third component.

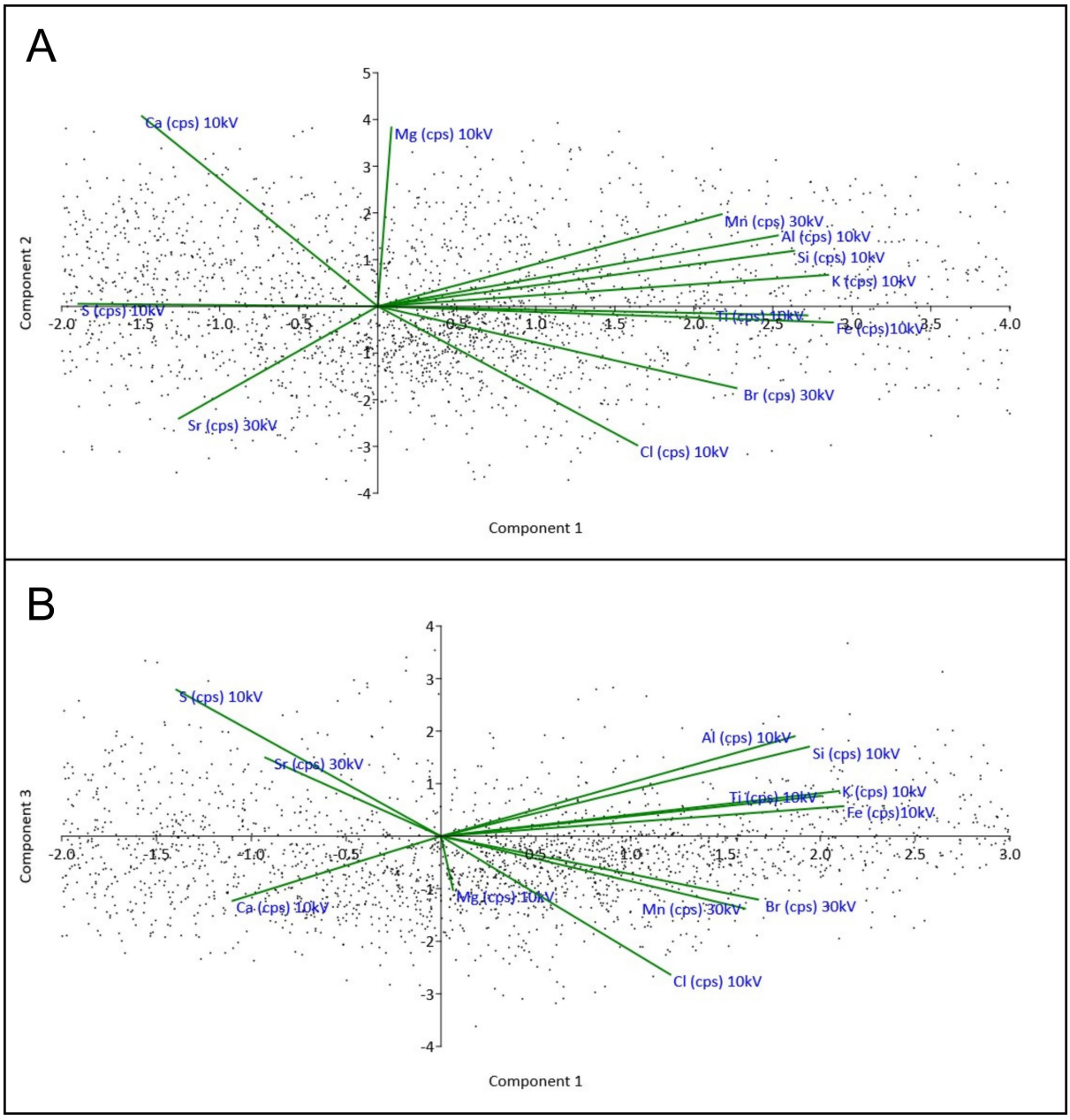

Figure 3.43. Principal component analysis of the XRF data from Las Latas. (A) First and second component. (B) First and third component.

3.5. Sulphur and oxygen isotope analysis

Table 3.6 and Figure 3.44 show the results of the sulphur and oxygen isotope analysis. For Alicante, the $\delta^{34}S$ ranges between 9.5 and 12.9 ‰ and the $\delta^{18}O$ between 18.4 and 22.2 ‰.

For Las Latas, the $\delta^{34}S$ ranges between 15.8 and 18.7 ‰ and the $\delta^{18}O$ between 21.3 and 23.9 ‰. This means that the $\delta^{34}S$ values of LFP are significantly higher than those of Alicante, whereas the $\delta^{18}O$ are mostly overlapping. The standard deviation of $\delta^{18}O$ was determined by measuring each sample twice. For $\delta^{34}S$, no sample-specific standard deviations were available, but the standard deviations of the standards that were included in the measurement were never larger than 0.1 ‰.

In Figure 3.44, the results are compared to the range of values of Triassic gypsum in the Betic Cordillera, which has $\delta^{34}S$ values between 12.5 and 16.6 ‰ and $\delta^{18}O$ values between 8.9 and 16.9 ‰ (Ortí et al., 2014b). The results which were obtained by Höbig et al. (2016) from Laguna de Fuente de Piedra are also shown for comparison. The locations of the cores from which these samples were derived are indicated in Figure 2.2A.

Table 3.6. Sulphur and oxygen isotopes of the samples from Alicante and Las Latas.

Sample	**$\delta^{34}S$ (‰)**	**$\delta^{18}O$ (‰)**	**$\delta^{18}O$ std. dev. (‰)**
1ALI	12.9	21.4	0.3
2ALI	9.6	19.7	0.2
3ALI	12.5	22.2	0.4
4ALI	9.5	18.4	0.1
5ALI	10.7	20.8	0.7
1LFP	15.8	21.3	0.3
2LFP	16.9	21.8	0.1
3LFP	16.5	22.7	0.5
4LFP	18.7	23.9	0.1
5LFP	16.1	21.5	0.2
6LFP	16.5	20.2	0.1
8LFP	16.7	22.5	0.2
9LFP	16.9	22.7	0.2

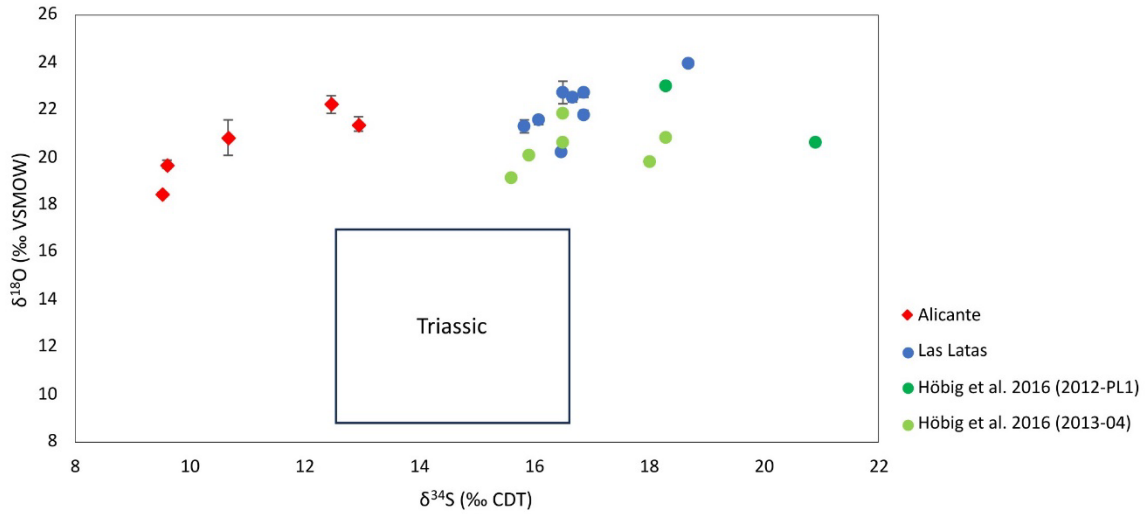

Figure 3.44. Sulphur and oxygen isotopes of the samples from Alicante (red diamonds) and Las Latas (blue circles). The black box indicates the range of isotope values in Triassic gypsum (Ortí et al., 2014a). The light and dark green circles are isotope measurements on samples from different cores from Laguna de Fuente de Piedra (Höbig et al., 2016).

4. Discussion

4.1. Paleoenvironmental conditions of evaporite deposition

4.1.1. Data quality and significance

Thin sections

The ten thin sections that were analysed (3.1) had enough quality to study the sedimentology of the samples in high detail. The gypsum crystals were well preserved and did not show signs of artificial degradation or recrystallization. Instead, the gypsum from Alicante and the gypsum from Las Latas were clearly different in nature, a difference which would have been smoothed out if the preparation of the thin sections had caused significant distortions.

Halite may have been more affected by the thin section preparation process. It was found in only one thin section (4LFP), although XRD analysis has shown that even in the carbonate intervals of both cores, between 5 and 10 % of the sediment consists of halite. Given the fact that the halite crystals that were observed were very small (<50 μm) and halite is easily degraded by both water and alcoholic liquids, it is possible that the absence of halite is the result of the thin section preparation process. Therefore, some sediment was taken from the cores to observe without any preparation under the microscope. In these sediment samples, more halite was present, but the shape and size of the crystals were similar to those observed in the thin section.

SEM-EDS

The results of SEM-EDS analysis (3.2) show clear differences between the spectra of gypsum, dolomitic sediment and the dark spots on the gypsum crystals. Even though the number of EDS counts is relatively low, the differences between the measured elements are significant, as is shown by the standard deviations in Table 3.1, 3.2 and 3.3. The absence of a peak in iron

in Figure 3.20 shows that the dark stripes are not the same as the iron oxides that were observed by Magee (1991). As discussed above (3.2), the spectrum is most consistent with glauberite ($Na_2Ca(SO_4)_2$). This interpretation could be tested further by analysing the thin section with cross polarized light microscopy (Galamay et al., 2023).

Elemental analysis

The significance of the ICP-OES results (3.3) can be determined on the basis of the standards that were included in the test (Table 3.5). The double measurement of standard 88b makes it possible to determine the precision outcomes. In Table 4.1, it is shown that the difference between the first and second measurement is never more than 1.1 % in the case of the major elements. The average difference is 0.28 ± 0.35 %. These deviations are so small that it is not possible to show them as error bars in Figure 3.31 and 3.32.

Table 4.1. Difference between the two measurements of standard 88b. Difference is calculated for the deviation of 88b_b from 88b_a.

Element	**88b_a**	**88b_b**	**% difference**
Mg	130229	130089	0.108
Ca	220331	220024	0.139
Si	642	635	1.090
Al	489	490	0.204
Fe	1800	1793	0.389
Mn	124	124	0
Sr	65	65	0

A second consideration regarding data quality concerns the procedure of the extraction of gypsum. Gypsum was separated from dolomite and siliciclastic material by dissolution (2.3.3). However, it is possible that other minerals, including dolomite, have been dissolved in this way as well. This is especially relevant for the concentrations of magnesium that were

measured in the samples. The Mg concentrations in all ten samples are very high compared to gypsum samples from other evaporite formations, in which the Mg concentration is often below 100 ppm (Zaheri & Rafiei, 2019). The Mg concentration ranges between 3,002 and 11,823 ppm in the samples from Alicante, and in the samples from Las Latas between 5,452 and 13,315 ppm.

For most of the samples, it can be assumed that both dolomite and gypsum were readily available in the powder to which MilliQ was added for dissolution. Given the much higher solubility of gypsum in pure water at ambient conditions (0.03305 mol/L versus 0.00042 mol/L for dolomite), maximal dissolution of both minerals would lead to 78 times more Ca^{2+} ions deriving from gypsum than from dolomite. The measured Ca concentration can therefore be used to determine the amount of Mg derived from dolomite, since Ca and Mg are present in dolomite in equal amounts, and XRD analyses of carbonate samples from the core have not shown significant amounts of other Mg-bearing minerals.

Table 4.2 shows the calculated amounts of Mg deriving from dissolved dolomite assuming maximal dissolution and compares these with the measured amount of Mg. In the case of 1ALI, 2 ALI, 3ALI and 2LFP, the calculations show that most of the Mg has derived from dolomite. When the calculated dissolved Mg is higher than the measured Mg, as is the case for 1ALI, this implies that no full dissolution of dolomite has taken place. In the case of 5ALI, 1LFP, 3LFP, 4LFP and 5LFP, dissolution of dolomite can explain less than half of the measured Mg. These calculations show that dissolution of dolomite cannot be the full explanation for the high Mg concentrations in the gypsum.

There are some additional potential sources of error which could not be quantified. Imperfect centrifugation could lead to the incorporation of insoluble material (including dolomite) in the samples. Previous analyses of dolomite samples suggested that the relatively high concentrations of Si might be the result of overlapping wavelengths (Zeina Naim, personal communication). This possibility should be the topic of further research.

Table 4.2. Calculation of percentages of Mg as measured by ICP-OES deriving from dolomite in the samples. Ca = Mg deriving from dolomite dissolution is calculated by assuming maximal dissolution of dolomite and gypsum and using the solubility ratio between the two minerals (1:78).

Sample	**Measured Ca (ppm)**	**Calculated Ca = Mg deriving from dolomite dissolution (ppm)**	**Measured Mg (ppm)**	**Percentage Mg deriving from dolomite dissolution**	**Corrected Mg (ppm) (Measured Mg – calculated Mg)**
1ALI	249667	3154.45	3002.21	105	-152.24
2ALI	223006	2817.60	4010.16	70.3	1193.56
3ALI	224574	2837.41	4493.61	63.1	1656.2
4ALI	45260.1	571.85	35243.7	1.6	34671.85
5ALI	170729	2157.10	11823.9	18.2	9666.8
1LFP	177886	2247.53	12937	17.4	10689.47
2LFP	229177	2895.57	5452.32	53.1	2556.75
3LFP	196991	2488.91	13315.3	18.7	10826.39
4LFP	219985	2779.43	7810.1	35.6	5030.67
5LFP	108734	1373.82	9856.25	13.9	1373.82

XRF analysis

For the XRF analysis (3.4), the significance of the correlation between evaporite layers on the one hand and the fluctuations in elements and element ratios on the other hand was determined with a Pearson correlation test. This test made it possible to determine the strength and direction of correlation. S and S/Fe were selected as proxies for the presence of evaporites.

Conform to standard practice (Mukaka, 2012), any correlation with a Pearson coefficient between -0.3 and 0.3 is regarded as negligible. The results are shown in Table 4.3 (for Alicante) and Table 4.4 (for Las Latas). Significant correlations are shaded red (if negative) or green (if positive).

Table 4.3. Pearson correlations of the analysed elements and element ratios versus S and S/Fe for Alicante.

Element or ratio	Pearson Correlation (S)	Pearson Correlation (S/Fe)
Mg (cps) 10kV	-0.028266572	-0.064246165
Ca (cps) 10kV	-0.150099818	-0.122846035
Al (cps) 10kV	-0.206152003	-0.221569218
Si (cps) 10kV	-0.221710603	-0.241457355
Ti (cps) 10kV	-0.253641502	-0.279474053
K (cps) 10kV	-0.262657089	-0.312478423
Fe (cps)10kV	-0.304884445	-0.371380381
Mn (cps) 30kV	-0.385060395	-0.437546519
Cl (cps) 10kV	0.126567195	0.020235891
Br (cps) 30kV	0.08999164	-0.013763899
Sr (cps) 30kV	0.120282987	0.133609242
S (cps) 10kV	1	0.820062193
log(Ca/Sr)	-0.26442021	-0.240345156
log(Ca/Ti)	0.186933059	0.297258424
log(Fe/Al)	-0.126847041	-0.199521487
log(Fe/Ca)	-0.22040812	-0.358266325
log(Mn/Ti)	0.031259956	0.077404093
log(Mn/Ca)	-0.237112193	-0.345461681
Sr/Ti	0.218357266	0.37097748
S/Fe	0.820062193	1

Table 4.4. Pearson correlations of the analysed elements and element ratios versus S and S/Fe for Las Latas.

Element or ratio	Pearson Correlation (S)	Pearson Correlation (S/Fe)
Mg (cps) 10kV	-0.088855601	-0.185551663
Ca (cps) 10kV	0.285068663	0.198709688
Al (cps) 10kV	-0.329033672	-0.321625506
Si (cps) 10kV	-0.385352075	-0.353487783
Ti (cps) 10kV	-0.538784214	-0.367015622
K (cps) 10kV	-0.585290421	-0.420939428
Fe (cps)10kV	-0.596983582	-0.398696817
Mn (cps) 30kV	-0.647936038	-0.418887295
Cl (cps) 10kV	-0.528605147	-0.35758347
Br (cps) 30kV	-0.599410346	-0.402224566
Sr (cps) 30kV	0.264605927	0.183905278
S (cps) 10kV	1	0.670682609
log(Ca/Sr)	-0.156127496	-0.077674384
log(Ca/Ti)	0.654938556	0.574143493
log(Fe/Al)	-0.724698601	-0.535506655
log(Fe/Ca)	-0.66427342	-0.565046788
log(Mn/Ti)	0.06366328	0.166518004
log(Mn/Ca)	-0.729167122	-0.459125738
Sr/Ti	0.374261695	0.517217347
S/Fe	0.671327973	1

The results of the Pearson correlation test show that many correlations between evaporite layers and elements and elements ratios are significant in the case of Las Latas, but insignificant in the case of Alicante. When S was used as a proxy for evaporite layers, only Fe and Mn showed significant correlations in additional to the trivial cases of S and S/Fe. These results may show that significant correlations are simply absent, but an alternative explanation is the fact that S and S/Fe are worse proxies for evaporite layers in the case of Alicante than in the case of Las Latas (3.4.1).

The PCA of the Alicante and Las Latas XRF data show generally the same results as the Pearson correlation test, with negative correlations between S on the one hand and most other elements except Ca, Mg and Sr on the other hand. In this way, the distinction between authigenic minerals (gypsum and dolomite) and clastic material (clay and sand) becomes visible. The inclusion of XRD data does not give better results. A possible explanation for this is the fact that the XRD data were all derived from carbonate samples; therefore, the mineralogical differences between carbonate and evaporite layers are not included in this analysis.

Sulphur and oxygen isotope analysis

The standard deviations that were measured for $\delta^{34}S$ and $\delta^{18}O$ (3.5) show that the differences between the results from Alicante, Las Latas and the literature data that were used for comparison are significant. The average standard deviation of the $\delta^{18}O$ is 0.26 ± 0.17 ‰. In the case of $\delta^{34}S$, the eight standard deviations that were measured for the standards were on average 0.038 ± 0.048 ‰. This is too small to be visible in Figure 3.44.

4.1.2. Data interpretation

Petrography

The dominant evaporite facies in the Alicante core is bottom-grown selenite, which is indicative of long-term, highly evaporative conditions during which dolomite formation almost stopped. 3ALI is the representative of this facies. The other four thin sections show that other occurrences of gypsum in the Alicante core are the result of diagenetic alteration of carbonate sediment, i.e., the precipitation of gypsum from interstitial brines. This means that the lake was not saline enough for evaporite precipitation to occur when the lake was filled with water.

In the case of 5ALI, the specific characteristics of the diagenetic gypsum crystals point to a pedogenic origin, which implies that the lake had desiccated. 5ALI (from 4.90 m depth comes from the section of the core above the upper selenite layer (at 5.40 m depth) in a laminated interval of the core. Therefore, this thin section indicates a shift from relatively deep water conditions (under which the selenite layers could have formed) to conditions in which the lake was regularly desiccated between 5.40 m and 4.90 m depth. Giralt et al. (1999) mention an abrupt shift towards wetter conditions around 3.50 m depth. This would place 4ALI (at 2.20 m depth) within the period in which the water level of the lake was more stable.

In contrast to the thin sections from Alicante, the thin sections from Las Latas show the presence of primary microcrystalline gypsum, whereas selenite is absent. The microcrystalline gypsum forms thin evaporite laminae that are separated by even thinner dolomite laminae. These gypsum-dolomite alterations are best interpreted as annual cycles, in which the dolomite lamina formed during the wet season in microbial mats, which were then gypsified during the dry season. This annual cyclicity corresponds well with the annual fluctuations in the water level of Laguna de Fuente de Piedra (Rodríguez-Rodríguez et al., 2016). Reverse grading shows that gypsum precipitation initially occurred in the water

column, after which during increased evaporative conditions bottom overgrowth occurred. The wavy character of many laminae is consistent with a microbial mat origin.

The dynamics behind the evaporite-dolomite associations are very different in Laguna de Salinas and Laguna de Fuente de Piedra. In Laguna de Fuente de Piedra, the water chemistry fluctuated yearly between conditions of relatively low salinity in which dolomite could form and conditions of high salinity under which evaporites could form. In Laguna de Salinas, on the other hand, high-salinity conditions remained constant for a much longer period and when the water level was high enough for selenite formation, whereas at other times, no evaporite laminae could form and the lake occasionally desiccated.

The presence of glauberite on top of a layer of massive gypsum in the thin section of 2ALI is best interpreted as a diagenetic alteration. Glauberite can be a primary precipitate, but is most often precipitated in interstitial waters (Ortí et al., 2002). The high concentration of sodium, magnesium and sulphate in the water of Laguna de Salinas make the secondary precipitation of glauberite a plausible scenario.

Evaporative conditions

The concentration of Mg and Sr in gypsum is positively correlated with the brine concentration and growth rate of the gypsum crystals (Kushnir, 1980). The relationship between Mg and Sr concentration and temperature is weaker and less well resolved (Kushnir, 1980; Rosell et al., 1998). Since growth rate is dependent on brine concentration, Mg and Sr concentrations are a good measure of evaporative conditions.

When Mg concentrations are corrected, the ICP-OES results show concentrations between 1194 and 10826 ppm with the exception of 1ALI, for which the corrected Mg concentration is negative (which implies incomplete gypsum dissolution) and 4ALI, which has a Mg concentration of 34672 ppm and will be discussed below. With these two samples excluded, the average Mg concentration in the samples from Alicante is 4172 ± 3890 ppm and the

average Mg concentration in the samples from Las Latas is 6095 ± 3986 ppm. Compared to the gypsum samples measured by Zaheri and Rafiei (2019), these values fall in the upper end of the spectrum of Mg concentrations in gypsum, which indicates that the gypsum in both lakes were formed under strong evaporative conditions. 3ALI, the selenite sample, has the lowest Mg concentration among the samples from Alicante, which indicate relatively weak evaporative conditions during the formation of selenite.

Except for 4ALI, which is in several respects an anomalous sample that will be discussed below and has a Sr concentration of 4821 ppm, the gypsum samples from Alicante have an average Sr concentration of 1150 ± 509 ppm. The only selenite sample, 3ALI, has a Sr concentration of 1376 ppm. Rosell et al. (1998) give as the range of Sr concentrations in selenite 1000 – 2600 ppm with increasing Sr concentrations when the salinity increases. The Alicante selenite falls within this range, slightly at the low salinity end of the spectrum.

The average corrected Mg and Sr concentrations in the samples from Las Latas are higher than the corresponding concentrations in the samples from Alicante, indicating stronger evaporative conditions (Kushnir, 1980). This corresponds to the fact that, at present, the climate around Laguna de Fuente de Piedra is warmer and more arid than in Alicante.

The XRF results point to evaporative conditions during gypsum formation as well. Ca/Ti is indicative of increased evaporative concentration (Davies et al., 2015), since Ti, as noted above, is indicative of increased runoff (Haberzettl et al., 2007). The positive correlation between log(Ca/Ti) and the Las Latas evaporite layers is consistent with this interpretation of the ratio.

Sr/Ti is listed by Davies et al. (2015) as an indicator of in-lake strontianite ($SrCO_3$) precipitation. However, the ICP-OES analysis has shown that gypsum samples from both Alicante and LFP have high Sr concentrations, in correspondence with gypsum samples from other areas that were formed under highly evaporative conditions. The incorporation of Sr in gypsum because of strong evaporative conditions is therefore a more plausible explanation

as the variation in Sr/Ti, since Sr/Ti is high in evaporite layers. Some of the Sr may be incorporated in celestine within the evaporite layers (Rosell et al., 1998).

Oxygenation

The concentrations of several elements in lake sediments are controlled by the redox conditions in the lake water. Under anoxic bottom water conditions, Mo is enriched in sediments whereas Mn and Fe are depleted (Morford & Emerson, 1999).

Although the ICP-OES results show measurable concentrations of Mo in only one sample (4ALI), the concentrations of Mn and Fe are much lower in the gypsum samples than in the dolomite samples that were studied in the same lakes. In the dolomite samples that were used to compare the results, the Mn concentration ranged between 104 and 607 ppm in the case of Alicante; the Fe concentration ranged between 219 and 3585 ppm in the case of Alicante. This suggests that bottom waters were less oxic during periods of gypsum precipitation than in the periods in which dolomite was formed.

The XRF data confirm this interpretation. Fe/Al is a ratio which is regarded as indicative of anoxic bottom waters in marine settings (Lyons & Severmann, 2006; Spofforth et al., 2008; Rothwell & Croudace, 2015). The log(Fe/Al) in the Las Latas core is relatively low in evaporite layers, which would then indicate relatively oxic conditions. However, the increase of Fe in the sediment is explained as the result of the formation of pyrite and other iron-bearing minerals (Lyons & Severmann, 2006), but these are absent in the cores studied in this thesis. In other cases, Fe(II) precipitates less readily than its oxidised form, Fe(III) (Jansen et al., 2003). Therefore, there is a positive correlation between Fe and oxygenation in the absence of pyrite.

Instead of log(Fe/Al), which was designed for siliciclastic marine settings, log(Fe/Ca) can be used as a more reliable indicator of water oxygenation. Like log(Fe/Al), log(Fe/Ca) is low in evaporite layers, which is shown by the negative correlation between log(Fe/Al) and log(Fe/Ca) on the one hand and S counts on the other in both lakes. There is also a negative

correlation between Fe counts and S counts in both lakes. This negative correlation rules out that pyrite precipitation played a significant role in the concentration of Fe in the lake sediments. As explained above, there is a negative positive between Fe and oxygenation, as the oxidized form of iron (Fe(III)) precipitates more easily. Therefore, the low Fe concentrations in the evaporite samples indicate that gypsum was formed when oxygen concentrations were low.

Mn/Ti is likewise used as an indicator of oxygenation of the water column (Davies et al., 2015). Since Mn is most easily precipitated in manganese oxides, low Mn values indicate anoxic conditions. Log(Mn/Ti) shows a negligible positive correlation with S counts and S/Fe in the case of LFP. However, as in the case of log(Fe/Al), this ratio has been designed for siliciclastic settings. Therefore, the ratio log(Mn/Ca) is more indicative of oxygenation. This ratio shows that the dark layers were formed during periods in which the water column was well oxygenated. Between log(Mn/Ca) and S/Fe, there is a negative correlation in both lakes. The data of both lake show a negative correlation between Mn counts and S counts and S/Fe as well. These results show that gypsum was formed during periods in which the lake water was relatively anoxic.

The precipitation of gypsum when bottom waters had low oxygen concentrations corresponds to modern hypersaline environments in which evaporite-dolomite associations are formed. The solubility of oxygen in water decreases with salinity (Sherwood et al., 1991), but additional factors can decrease the oxygen concentration even more.

In Lagoa Vermelha, the activity of sulphate-reducing bacteria leads to oxygen depletion at the bottom of the water column (van Lith et al., 2002). In the microbial mat that was studied by Vasconcelos et al. (2006), the upper layer of the mat contained photosynthetic bacteria (cyanobacteria), leading to high oxygen concentrations, but below the mat, oxygen is consumed by sulphate-reducing bacteria. In other hypersaline lakes and lagoons, stratification originates from fresh-water input which leads to a low-salinity lid on top of the

saline lake water, leading to bottom water anoxia (Sonnenfeld et al., 1977; Petrash et al., 2012).

On the basis of the thin section analysis, it was concluded that the microcrystalline evaporite laminae from Las Latas were formed during the dry season, whereas the selenite layers from Alicante were formed during long-term stable conditions. Therefore, it is improbable in both cases that the oxygen depletion during gypsum formation was the result of a stratification that originated from the input of fresh water. A more likely interpretation is that, as in the case of Lagoa Vermelha, microbial activity leads to oxygen consumption; under low salinity conditions, when dolomite is formed, this consumption is compensated by the production of oxygen by photosynthetic bacteria. But when the salinity becomes higher, oxygen production by photosynthetic bacteria decreases and bottom waters become anoxic. This can explain the difference between Mn and Fe concentrations in dolomite, which is formed in the initial stage when photosynthetic bacteria still thrive and produce oxygen, and gypsum, which is formed under highly evaporative conditions under which oxygen production has stopped.

The samples from Alicante have lower concentrations of Mn and Fe than the samples from Las Latas. In several samples, the concentration of Mn or Fe was below the detection limit. In the case of the selenite sample 3ALI, both Mn and Fe were too low in concentration to be measured. This suggests that anoxic conditions were even stronger in Laguna de Salinas than in Laguna de Fuente de Piedra. This conforms with the hypothesis that the selenite layers from Alicante were formed under more stable conditions than the microcrystalline gypsum layers from Las Latas, leading to stagnant and oxygen-depleted water. The diagenetic gypsum of Alicante likewise formed in this stagnant water.

Siliciclastic input

The incorporation of Si and Al, elements which are most common in siliclastic minerals and absent in evaporite minerals (Warren, 2016, p. 3), is a measure of siliciclastic input. The concentration of Si and Al in the gypsum samples were both lower than the concentration of these elements in dolomite. In Alicante, the Al concentration in gypsum ranged from below detection limit to 82 ppm, whereas the Al concentration in dolomite ranged from 295 to 758 ppm; the Si concentration in gypsum ranged from 181 ppm to 329 ppm, whereas the Si concentration in dolomite ranged from 498 ppm to 2117 ppm.

Compared to Las Latas, the gypsum samples from Alicante have on average higher Al concentrations but lower Si concentrations. This indicates that in Laguna de Salinas, the relative proportion of quartz input is higher than in Laguna de Fuente de Piedra, whereas in Laguna de Fuente de Piedra, the relative proportion of clay input is higher than in Laguna de Salinas. There are several potential causes for this difference; it can be a reflection of differences in the regional geology of the basins of the two lakes, or the fact that the location of the Las Latas core was farther from the shore than the Alicante core.

The negative correlation between evaporite layers in the Las Latas core and both Al and Si as is shown in the XRF data can be explained by the fact that these elements are indicative of the presence of siliciclastic sediment (Davies et al., 2015). Since siliciclastic sediment is brought into the lake by runoff, the presence of this type of sediment is correlated with runoff and therefore with the wet season. The negative correlation therefore confirms the hypothesis that evaporite layers were formed during the dry season. The negative correlation with K, which is a constituent of feldspar, may be explained in this way as well.

Ti is likewise related to increased runoff and clastic sediment input (Haberzettl et al., 2007; Davies et al., 2015). The relatively low Ti counts in evaporite intervals indicate that these originated during dry periods with little runoff and little clastic sediment input. The

high Ti counts in the organic-rich dark layers indicate that increased runoff led to more organic activity.

The higher siliciclastic input during the formation of dolomite corresponds with the model in which dolomite was formed during the wet season, when runoff was relatively high, which would have led to relatively high siliciclastic input.

Biological activity

Ca/Sr has been used to distinguish between biogenic carbonate on the one hand and non-biogenic carbonate and dolomite on the other (Hodell et al., 2008). However, within evaporite layers, both Ca and Sr will be mostly present in gypsum. Therefore, log(Ca/Sr) cannot be used in the same way as in Hodell et al. (2008).

Br counts have been used as a proxy for marine biological activity (Ziegler et al., 2008; Davies et al., 2015). Since this proxy is based on the fact that bromine is incorporated in organic matter under saline conditions (Ziegler et al., 2008), this proxy can work for salt lakes as well. The negative correlation between Br and S and S/Fe in the case of Las Latas indicates reduced biological activity during the formation of evaporites. This is consistent with the interpretation that gypsum formed when microbial activity in the lakes reduced.

Outliers

Among the samples from Alicante, 4ALI is an outlier in several respects; likewise, 4LFP is an outlier in several respects among the samples from Las Latas (3.3, Figure 3.32). 4ALI has concentrations of Mg and Ca in almost equal proportions, which implies that the soluble mineral(s) in the sample cannot be pure gypsum. However, the sample also differs from the dolomite samples by showing much lower Fe and Mn concentrations and much higher Sr concentrations (Figure 3.31). Without more advanced mineralogical analytic techniques such as XRD, it is not possible to determine which other minerals are present in 4ALI.

An additional characteristic of 4ALI is a measurable concentration of Zn and a high concentration of Mo (Table 3.4). Just as Fe and Mn are depleted from sediments under anoxic conditions, Zn and Mo are enriched in sediments (Calvert & Pedersen, 1993). Therefore, the ICP-OES data indicate that 4ALI was formed under the most anoxic conditions among the samples from Alicante and Las Latas. According to Giralt et al. (1999), the interval in which 4ALI occurs was formed when the water level of Laguna de Salinas increased and became more stable. The presence of stagnant waters corresponds with the indications of anoxic conditions.

4LFP shows higher Fe and Mn concentrations and lower Sr concentrations than the other samples from Las Latas. In light of the paleoenvironmental interpretation given to these elements above, this indicates that 4LFP was deposited under more oxic and less evaporative conditions than the other samples. This corresponds to the fact that 4LFP derives from a section of the Las Latas core in which evaporite layers are relatively infrequent (Figure 2.6).

Oxygen isotopes

The $\delta^{18}O$ values of the gypsum samples of Alicante and Las Latas fall in the same range (20.51 ± 1.32 ‰ and 22.08 ± 1.06 ‰, respectively). These values are much heavier than the range of oxygen isotope values in Triassic gypsum of the Betic Cordillera, $\delta^{18}O$ values between 8.9 and 16.9 ‰ (Ortí et al., 2014b). Isotope results of a more recent study show a wider range of results, but a $\delta^{18}O$ of above 20 ‰ has been measured only once out of 376 samples, in a region which is not close either to Laguna de Fuente de Piedra or Alicante (Ortí et al., 2022).

An enrichment of $\delta^{18}O$ relative to the gypsum source can be explained in two ways. First of all, there is an exchange between the isotopic signature of dissolved sulphate. Therefore, the isotopic signature of $\delta^{18}O$ in gypsum can reflect the isotopic composition of the water in which the gypsum was formed. In a highly evaporative environment, the $\delta^{18}O$ of water will

become heavier, as ^{16}O is favoured during evaporation. The heavy $\delta^{18}O$ values of the gypsum samples is therefore consistent with an evaporitic environment.

In addition, the activity of sulphate-reducing bacteria can remove ^{16}O from the sulphate reservoir as well (Fritz et al., 1989; Wankel et al., 2014; Pellerin et al., 2020). Therefore, heavy $\delta^{18}O$ values can also point to microbial activity. In the case of Alicante and LFP, both processes, i.e. evaporation and sulphate reduction, probably played a role. The role of evaporation is substantiated by the fact that gypsum, as an evaporite mineral, requires an evaporitic environment. The role of sulphate-reducing bacteria is substantiated by the role these organisms play in the formation of dolomite (Vasconcelos et al., 1995).

Sulphur isotopes

The $\delta^{34}S$ values of Alicante and Las Latas are dissimilar. The average value of the Alicante samples is 11.04 ± 1.42 ‰, whereas the average value of the Las Latas samples is 16.74 ± 0.81 ‰. The sulphur isotopes of Las Latas are therefore much heavier than those of Alicante. Compared to the sulphur isotopes in Triassic gypsum of the Betic Cordillera, which range between 12.5 and 16.6 ‰ (Ortí et al., 2014b), the Alicante values are lower and the Las Latas values are higher.

The heavy $\delta^{34}S$ values of Las Latas can be explained by the activity of sulphate-reducing bacteria. These bacteria favour ^{32}S over ^{34}S during sulphate reduction, leading to enrichment of ^{34}S in the residual sulphate (Sim et al., 2011). As in the case of the heavy $\delta^{18}O$ values that were found, the presence of sulphate-reducing bacteria is consistent with an environment in which dolomite has been formed.

The light $\delta^{34}S$ values of Alicante are more difficult to explain. There are two possible explanations for these light values. First, it is possible that there is a second source of sulphur besides Triassic gypsum. This second source, with light $\delta^{34}S$, would have been incorporated in the gypsum of Alicante, which resulted in light $\delta^{34}S$ values of the gypsum. The second

explanation is that the sediment of Alicante contains other sulphur-bearing minerals besides gypsum.

Two minerals with light $\delta^{34}S$ which are most common are native sulphur and pyrite. Although other minerals cannot be excluded, it will be evaluated which contribution these two minerals could have paid to the sulphur isotopes of the Alicante samples.

Native sulphur with very light $\delta^{34}S$ (from −17.1 to −3.7 ‰) is found in evaporite deposits in Southeastern Spain close to Alicante (Lindtke et al., 2011). The $\delta^{34}S$ of pyrite can be as low as −44‰ (Pasquier et al., 2017). Based on these data, mass balance equations (MBEs) can be used to determine the approximate contribution of native sulphur that is needed for such light $\delta^{34}S$. Table 4.5 shows the $\delta^{34}S$ values that are used for these equations.

Table 4.5. Values used for mass balance equations.

Source	**Lowest $\delta^{34}S$ (‰)**	**$^{34}S/^{32}S$**	**Average $\delta^{34}S$ (‰)**	**$^{34}S/^{32}S$**	**Highest $\delta^{34}S$ (‰)**	**$^{34}S/^{32}S$**
Native sulphur*	−17.1	0.04344	−11.5	0.04369	−3.7	0.04404
Triassic gypsum**	12.5	0.04475	14.9	0.04486	16.6	0.04493
Alicante gypsum	9.5	0.04462	11.0	0.04469	12.9	0.04477

* (Lindtke et al., 2011)
** (Ortí et al., 2014b)

All MBEs have the following general form:

$$(1)\ X_S = \frac{f_A - f_T}{f_S - f_T} \times 100\%$$

In which X_s is the fraction of sulphur deriving from another source than Triassic gypsum in percent, f_A the $^{34}S/^{32}S$ in the Alicante samples, f_T the $^{34}S/^{32}S$ in Triassic gypsum, and f_S the $^{34}S/^{32}S$ in the second source beside Triassic gypsum.

For the Alicante gypsum, both the average and lowest $^{34}S/^{32}S$ is taken into consideration. For the Triassic gypsum and the native sulphur, the lowest, average and highest $^{34}S/^{32}S$ are used in the MBEs. For pyrite, only the lowest value (−44‰) is used. Table 4.6 shows the percentages of sulphur not deriving from Triassic gypsum in each case.

Table 4.6. Percentage of sulphur from another source than Triassic gypsum in different scenarios.

Scenario	**Percentage of sulphur from other source (Alicante average (11.0‰))**	**Percentage of sulphur from other source (Alicante lowest value (9.5‰))**
Lowest native sulphur + lowest Triassic gypsum	4.58	9.92
Average native sulphur + average Triassic gypsum	14.53	20.51
Highest native sulphur + highest Triassic gypsum	26.97	34.83
Pyrite + lowest Triassic gypsum	2.40	5.21
Pyrite + average Triassic gypsum	6.52	9.21
Pyrite + highest Triassic gypsum	8.96	11.58

The results show that, for the average of all Alicante samples, between 2.40 and 26.97 percent of all sulphur has been derived from another source than Triassic gypsum. In the case of the lowest $\delta^{34}S$ that was measured (4ALI), the contribution was between 5.21 and 34.82 percent.

Since gypsum deposits can contain native sulphur and Triassic gypsum deposits are abundantly present in the surrounding of Alicante, it is possible that native sulphur in these deposits was the source of isotopically light sulphur. Lindtke et al. (2011) do not give a quantitative estimate of the amount of native sulphur present in the samples that they studied, although they call the native sulphur “abundant”. Native sulphur is present in many other gypsum deposits (Dessau et al., 1962; Ortí et al., 2010), but it is not known whether this

is the case in the gypsum deposits near Alicante. There are no mentions of the presence of pyrite in the basin of Laguna de Salinas in the literature.

Given the low concentrations of iron in all Alicante samples (3.3) and the negative correlation between Fe and S (4.1.1), it is unlikely that pyrite is present in the sediment. Pyrite, native sulphur or other sulphur-bearing minerals have not been found in the XRD analyses of dolomite. Therefore, the first explanation, that there has been a second source of sulphur besides Triassic gypsum, seems more likely. However, since XRD analyses were performed on samples from the carbonate intervals of the cores, more XRD analyses on gypsum-bearing intervals of the Alicante core could establish the origin of the light $\delta^{34}S$ of the gypsum samples with more certainty.

4.2. Chronological framework

4.2.1. Age model quality

As has been noted above (2.3.6), the age models of both cores have significant limitations. In both cases, data points had to be excluded as being the result of reworking, but no sedimentological grounds to determine which samples showed reworking were available. In the case of Alicante, the age model of the lowest 41.5 percent of the core relies on extrapolation from the lowest data point, and in the case of Las Latas, the age model has largely been obtained from a different core without the possibility of stratigraphic correlation.

Despite these limitations, the age models give a general indication of the depth-age relationship in the cores. The sedimentation rate remains relatively constant in the upper part of the Alicante core (Figure 2.12), which makes it improbable that the depth-age relationship deviates very strongly from the extrapolation to the bottom part. In a similar way, it is

improbable that the stratigraphy of the Las Latas core deviates very strongly from the stratigraphy of 2013-04, as the cores are about 600 m apart.

4.2.2. Paleoclimatic conditions of evaporite deposition

The periods of evaporite deposition in Laguna de Salinas and Laguna de Fuente de Piedra can be compared to the general paleoclimatic changes that have been reconstructed for this period. Three paleoclimatic records have been selected for comparison to the Alicante and Las Latas data. First, the $\delta^{18}O$ record of the Greenland ice core NGRIP has been selected is representative for general climatic fluctuations in the Northern Hemisphere (Andersen et al., 2004). Second, a sea surface temperature (SST) alkenone record from the Alboran Sea has been selected as a representation of temperature changes in southern Spain (Martrat et al., 2004; Figure 2.1B). Third, a quantitative reconstruction of mean annual precipitation (MAP) on the basis of pollen data from Laguna de Padul has been selected to represent precipitation changes in southern Spain (Camuera et al., 2022; Figure 2.1B). The locations of the latter two record lie geographically between Laguna de Salinas and Laguna de Fuente de Piedra, although slightly closer to Laguna de Fuente de Piedra.

Figure 4.1 shows the three paleoclimatic records, as well as the S record of the XRF data of both cores and the intervals with evaporite layers.

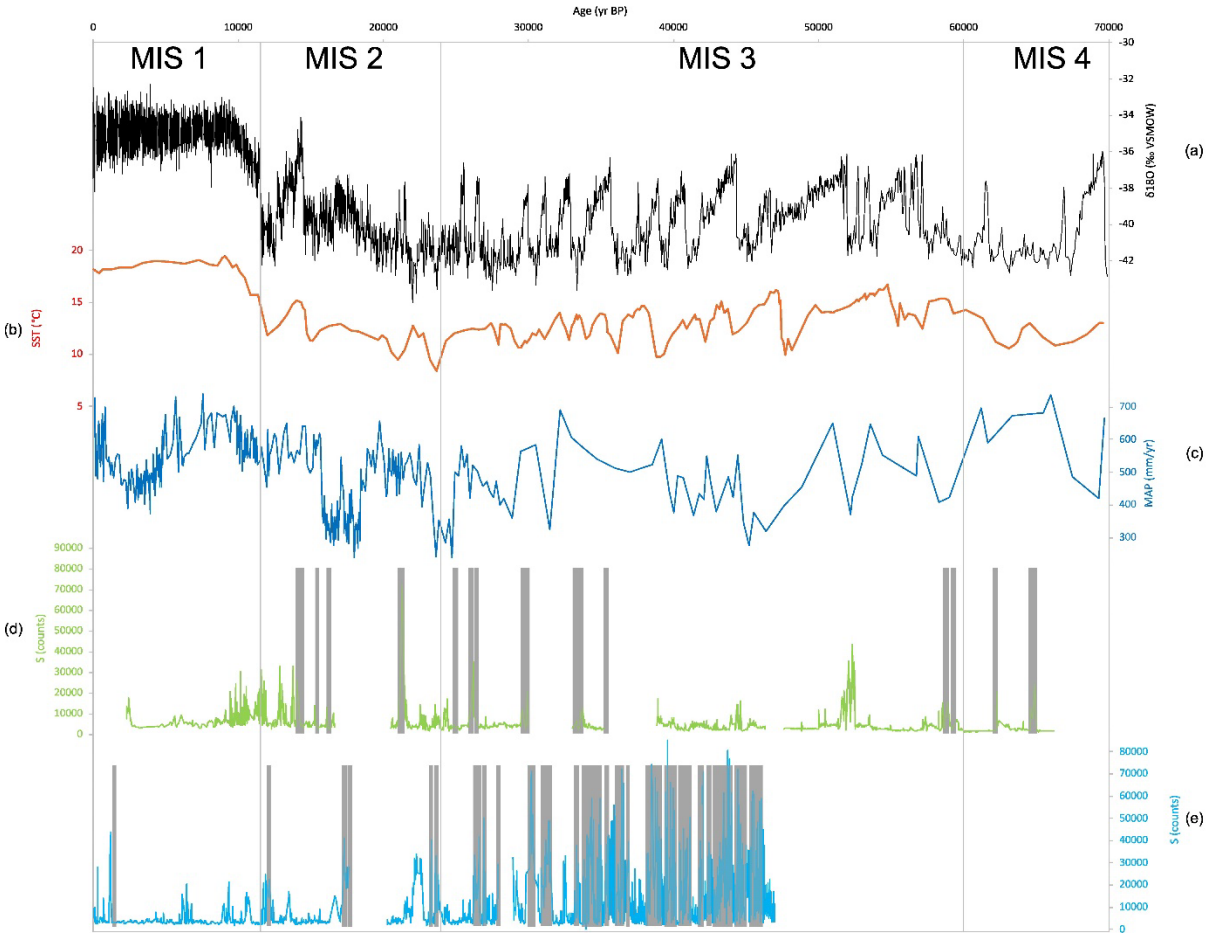

Figure 4.1. (a) $\delta^{18}O$ record from NGRIP (Andersen et al., 2004); (b) SST record from the Alboran Sea (Martrat et al., 2004); (c) MAP record from Laguna de Padul (Camuera et al., 2022); (d) S counts/s from the Alicante core; grey bars indicate the presence of selenite layers; (e) S counts/s from the Las Latas core; grey bars indicate intervals with (clusters of) evaporite laminae. The graph is divided into marine isotope stages (MIS 1-4) (Lisiecki & Raymo, 2005).

To determine the correlation between evaporite deposition and the three paleoclimatic records, a Pearson correlation test was performed. In order to do this, the intervals of the Alicante and Las Latas core for which XRF data were available were linearly interpolated such that dataset was evenly spaced in intervals of 10 yr. The paleoclimatic datasets were interpolated in the same way. Table 4.7 shows the resulting correlations.

Table 4.7. Pearson correlations of the sulphur counts from Alicante and Las Latas versus three paleoclimatic records.

Element	**Pearson Correlation (δ18O)**	**Pearson Correlation (SST)**	**Pearson Correlation (MAP)**
S (Alicante)	0.06030228	0.015327518	-0.029508578
S (Las Latas)	-0.259838977	-0.305524051	-0.239798301

In the case of Alicante, the Pearson correlations give no definitive answer to the relationship between evaporite deposition and paleoclimatic conditions. However, in the case of Las Latas, the Pearson correlations seem to imply a negative correlation between evaporite deposition and $\delta^{18}O$, SST and MAP. This implies that evaporite deposition was highest during cold and dry periods.

Figure 4.1 shows that most evaporite intervals in the Las Latas core were formed during the last two stages of the last glacial, whereas evaporite layers are mostly absent in the Holocene. The 'bundles' of evaporite layers may correspond to the particular strong Dansgaard-Oeschger cycles during MIS 3. However, this can only be established when a more accurate age model is available.

Although the Pearson correlation is inconclusive in the case of the Alicante core, Figure 4.1 shows some general trends which relate the deposition of selenite layers to paleoclimatic conditions. As in the case of the Las Latas core, selenite layers are absent in the Holocene part of the core. The laminated interval between 1.90 and 5.00 m marks the Pleistocene-Holocene transition. Within the first part of MIS 3, there is an absence of selenite layers. Given the chronological uncertainties, the selenite layers in the bottom part of the core may have been formed during MIS 4. This suggests that the selenite layers were formed during the two coldest periods within the timeframe covered by the core (MIS 2 and 4). The absence of this negative correlation between evaporite formation and temperature in the Pearson correlation (Table 4.7) can be explained by the fact that S counts/s is a less strong indicator of evaporite layers for Alicante than for Las Latas (3.4.1).

The negative correlation between evaporite deposition and temperature shows that high temperatures were unnecessary for strong evaporative conditions. The wet conditions during interglacials and interstadials (Camuera et al., 2022) inhibited evaporite deposition and stimulated the formation of dolomite. During the drier periods of the last glacial, the salinity of the lake waters increased and gypsum was formed.

The same conclusion was reached for Laguna de Salinas by Giralt et al. (1999) and Burjachs et al. (2016) on the basis of a comparison between mineralogical and palynological data from the core that they studied.

Höbig et al. (2016), in their study of the 2013-04 core from Laguna de Fuente de Piedra, correlated gypsum-rich intervals to wet, high-water periods. However, the gypsum in those gypsum-rich intervals is detrital, and Höbig et al. (2016) interpreted this as the result of the transport of gypsum that were eroded from the lake margin. Therefore, their interpretation correlates well with the conclusion drawn for the Las Latas core: during dry periods, primary gypsum precipitated to form the evaporite laminae of the Las Latas core; during wet periods, similar gypsum layers were eroded and deposited as detrital gypsum in the 2013-04 core.

5. Conclusion

5.1. Synthesis

On the basis of the interpretations discussed above, the following synthesis can be made which describes the paleoenvironmental conditions under which evaporite layers were deposited in the two lakes.

Water level

Selenite layers in the Alicante core were formed under stable water conditions, in which large gypsum crystals could grow over a period of multiple years. Diagenetic gypsum, which formed in the laminated interval above 5.00 m, formed during desiccation events and shows characteristics of pedogenic gypsum. Whether the water level during the formation of selenite layers was higher or lower than during the formation of dolomite layers cannot be established.

In the Las Latas core, evaporite laminae were formed under dynamic conditions in which dolomite formation and gypsum precipitation alternated in seasonal cycles. The formation of gypsified microbial mats is generally associated with shallow-water conditions. The general absence of normal grading (except for one lamina in 5LFP) indicates that the lake desiccated after the period of gypsum deposition. The gypsum laminae were therefore deposited in very shallow water.

Evaporative conditions

During periods of evaporite formation, runoff to the lakes was relatively low, which led to relatively high salinities. In correlation with this, the input of siliciclastic sediment was low as well.

Biological activity

The biological activity during the formation of evaporites was in both lakes lower than during the formation of dolomite. In both lakes, the dolomite is of microbial origin; in the case of Alicante, the dolomitic sediment contains foraminifera and sponge spicules.

The gypsum laminae of the Las Latas core were formed by the gypsification of microbial mats which thrived during the wet season. The activity of sulphate-reducing bacteria in Laguna de Fuente de Piedra is evident from the high $\delta^{34}S$ and $\delta^{18}O$. The latter can also be the result of highly evaporitic conditions.

Oxygenation

The decrease in activity of photosynthetic bacteria, combined with low oxygen solubility in saline water and the oxygen consumption by sulphate-reducing bacteria, led to anoxic conditions during the formation of gypsum. In the deeper water of Laguna de Salinas, bottom waters were less oxic than in Laguna de Fuente de Piedra, both during the formation of selenite as well as during the formation of diagenetic gypsum.

Sulphur origin

The sulphur in the gypsum from Alicante has derived not only from Triassic gypsum, but also from a sulphur source with very light $\delta^{34}S$. Native sulphur, or else pyrite, is the most likely source that has contributed to the sulphur in Laguna de Salinas.

Chronology

Evaporite formation occurred mostly during the last glacial period. In the Holocene and during warmer periods in the Late Pleistocene, evaporite formation was strongly reduced in both lakes. This correlation is probably caused by the drier conditions during cold periods.

5.2. General conclusion

The evaporite-dolomite associations of Laguna de Salinas and Laguna de Fuente de Piedra shed light on conditions under which evaporite precipitation interrupted the formation of dolomite. Even though the mode of evaporite formation is different in both lakes – selenite layers in Laguna de Salinas and annual gypsum-dolomite couplets in Laguna de Fuente de Piedra –, the conditions under which the evaporites formed, were generally the same. During dry and cold periods, evaporative conditions in the lake increased, biological activity decreased, anoxia developed and gypsum was precipitated.

These findings contribute to our understanding of dolomite formation by microbial mediation. They show that microbial activity which led to the formation of dolomite under relatively warm and humid conditions was greatly reduced when the water became too saline during cold and dry periods, leading to a strong reduction in oxygen concentration in the water.

5.3. Suggestions for further research

For a better understanding of the data of both cores, a better age model is needed by which changes in mineralogy can be directly correlated to shifts in paleoclimate. The radiocarbon dates of Höbig et al. (2016) show that many samples are reworked, which means that a large amount of age measurements is needed to obtain an accurate age model.

Only one selenite sample has been analysed for this thesis. To make the interpretation of the selenite layers more robust, more samples are needed. In this way, difference between the average selenite and average diagenetic gypsum could be determined, leading to a better understanding of the environmental conditions in which they were formed.

Mineralogical analysis, such as XRD, could provide more certainty about the white veins in the sample 4ALI, which is an outlier among the samples from Alicante. A better understanding of this sample could provide more insight into the mineralogical and climatic shift that was reconstructed by Giralt et al. (1999).

The regional geology of the basin of Laguna de Salinas could be studied to determine the source of isotopically light sulphur in the lake.

Aside from dolomite and evaporites, both cores also contain other carbonate minerals, such as calcite and aragonite. These minerals were probably formed under even more humid conditions than the formation of dolomite (Giralt et al., 1999). The combination of the research of this thesis and the research on the carbonate intervals of the cores could therefore establish the boundary conditions under which dolomite formation could occur, with both the lower limits (below which evaporite precipitation occurred) and the upper limits (above which calcite or aragonite were formed.

Acknowledgements

Several people have greatly helped me during this Master thesis project which I want to thank. I want to thank Mónica Sanchez Román and Mariette Wolthers for their supervision of the project, the fruitful discussions of the data and their comments on the first version of this thesis. Zeina Naim and Guolai Li assisted during the practical work and have provided much of the additional information which they had obtained and was helpful for this thesis. Zeina also commented on the first version of the thesis. Additional help was provided by Camila Areias de Oliveira, Jeroen van der Lubbe and Roel van Elsas. I want to thank Luis Gibert (University of Barcelona) for the measurement of the sulphur and oxygen isotopes and the provision of helpful information, and Sander Huisman (Petrographica Westerbork) for the preparation of the thin sections.

References

Andersen, K. K., Azuma, N., Barnola, J.-M., Bigler, M., Biscaye, P., Caillon, N., Chappellaz, J., Clausen, H. B., Dahl-Jensen, D., Fischer, H., Flückiger, J., Fritzsche, D., Fujii, Y., Goto-Azuma, K., Grønvold, K., Gundestrup, N. S., Hansson, M., Huber, C., Hvidberg, C. S., … North Greenland Ice Core Project members. (2004). High-resolution record of Northern Hemisphere climate extending into the last interglacial period. *Nature*, *431*(7005), Article 7005.

Aref, M. A. M., & Taj, R. J. A. (2013). Recent analog of gypsified microbial laminites and stromatolites in solar salt works and the Miocene gypsum deposits of Saudi Arabia and Egypt. *Arabian Journal of Geosciences*, *6*(11), 4257–4269.

Aref, M. A. M., Taj, R. J. A., & Mannaa, A. A. (2020). Sedimentological implications of microbial mats, gypsum, and halite in Dhahban solar saltwork, Red Sea coast, Saudi Arabia. *Facies,* 66(2), 1–18.

Artieda, O. (2013). Morphology and micro-fabrics of weathering features on gyprock exposures in a semiarid environment (Ebro Tertiary Basin, NE Spain). *Geomorphology*, *196*, 198–210.

Arvidson, R. S., & MacKenzie, F. T. (1997). Tentative kinetic model for dolomite precipitation rate and its application to dolomite distribution. *Aquatic Geochemistry*, *2*(3), 273–298.

Bąbel, M. (1999). Facies and depositional environments of the Nida Gypsum deposits (Middle Miocene, Carpathian Foredeep, southern Poland). *Geological Quarterly*, *43*(4), Article 4.

Bąbel, M. (2004). Models for evaporite, selenite and gypsum microbialite deposition in ancient saline basins. *Acta Geologica Polonica*, *54*, 219–249.

Baker, P. A., & Kastner, M. (1981). Constraints on the Formation of Sedimentary Dolomite. *Science*, *213*(4504), 214–216.

Bischof, G. (1859). *Elements of Chemical and Physical Geology*. Cavendish Society.

Bontognali, T. R. R., Vasconcelos, C., Warthmann, R. J., Bernasconi, S. M., Dupraz, C., Strohmenger, C. J., & McKENZIE, J. A. (2010). Dolomite formation within microbial mats in the coastal sabkha of Abu Dhabi (United Arab Emirates). *Sedimentology*, *57*(3), 824–844.

Brady, P. V., Krumhansl, J. L., & Papenguth, H. W. (1996). Surface complexation clues to dolomite growth. *Geochimica et Cosmochimica Acta*, *60*(4), 727–731.

Burjachs, F., Jones, S. E., Giralt, S., & Fernández-López de Pablo, J. (2016). Lateglacial to Early Holocene recursive aridity events in the SE Mediterranean Iberian Peninsula: The Salines playa lake case study. *Quaternary International*, *403*, 187–200.

Calvert, S. E., & Pedersen, T. F. (1993). Geochemistry of Recent oxic and anoxic marine sediments: Implications for the geological record. *Marine Geology*, *113*(1), 67–88.

Camuera, J., Ramos-Román, M. J., Jiménez-Moreno, G., García-Alix, A., Ilvonen, L., Ruha, L., Gil-Romera, G., González-Sampériz, P., & Seppä, H. (2022). Past 200 kyr hydroclimate variability in the western Mediterranean and its connection to the African Humid Periods. *Scientific Reports*, *12*(1), Article 1.

Chilingar, G. V. (1956). Relationship Between Ca/Mg Ratio and Geologic Age. *AAPG Bulletin*, *40*(9), 2256–2266.

Cody, R. D. (1979). Lenticular gypsum; occurrences in nature, and experimental determinations of effects of soluble green plant material on its formation. *Journal of Sedimentary Research*, *49*(3), 1015–1028.

Cody, R. D., & Cody, A. M. (1988). Gypsum nucleation and crystal morphology in analog saline terrestrial environments. *Journal of Sedimentary Research*, *58*(2), 247–255.

Daly, R. A. (1909). First calcareous fossils and the evolution of the limestones. *GSA Bulletin*, *20*(1), 153–170.

Davies, S. J., Lamb, H. F., & Roberts, S. J. (2015). Micro-XRF Core Scanning in Palaeolimnology: Recent Developments. In I. W. Croudace & R. G. Rothwell (Eds.), *Micro-XRF Studies of Sediment Cores: Applications of a non-destructive tool for the environmental sciences* (pp. 189–226). Springer Netherlands.

Dessau, G., Jensen, M. L., & Nakai, N. (1962). Geology and isotopic studies of Sicilian sulfur deposits. *Economic Geology*, *57*(3), 410–438.

Fairbridge, R. W. (1957). The dolomite question. In *Regional Aspects of Carbonate Deposition* (pp. 125–178).

Folk, R. L. (1993). SEM imaging of bacteria and nannobacteria in carbonate sediments and rocks. *Journal of Sedimentary Research*, *63*(5), 990–999.

Fritz, P., Basharmal, G. M., Drimmie, R. J., Ibsen, J., & Qureshi, R. M. (1989). Oxygen isotope exchange between sulphate and water during bacterial reduction of sulphate. *Chemical Geology: Isotope Geoscience Section*, *79*(2), 99–105.

Galamay, A. R., Karakaya, M. Ç., Bukowski, K., Karakaya, & Yaremchuk, Y. (2023). Geochemistry of Brine and Paleoclimate Reconstruction during Sedimentation of Messinian Salt in the Tuz Gölü Basin (Türkiye): Insights from the Study of Fluid Inclusions. *Minerals,* 13, 171.

Gibert, L., Ortí, F., & Rosell, L. (2007). Plio-Pleistocene lacustrine evaporites of the Baza Basin (Betic Chain, SE Spain). *Sedimentary Geology*, *200*(1), 89–116.

Giralt, S. (1998). *El registre dels llacs salins con arxius paleoclimátics: Salines (Alacant) i Gallocanta (Aragó)*. [Doctoral Thesis, Universitat de Barcelona].

Giralt, S., Burjachs, F., Roca, J. R., & Julia, R. (1999). Late Glacial to Early Holocene environmental adjustment in the Mediterranean semi-arid zone of the Salines playa-lake (Alacant, Spain). *Journal of Paleolimnology*, *21*(4), 449–460.

Girela, L. L., & Martos, M. R. (1998). La laguna de Fuente de Piedra (Málaga), un área endorreica de interés ecológico ligada al karst yesífero-salino. In J. J. Durán & J. López Martínez, *Karst en Andalucía* (pp. 165–172). Instituto Tecnológico Geominero de España.

Given, R. K., & Wilkinson, B. H. (1987). Dolomite abundance and stratigraphic age; constraints on rates and mechanisms of Phanerozoic dolostone formation. *Journal of Sedimentary Research*, *57*(6), 1068–1078.

Haberzettl, T., Corbella, H., Fey, M., Janssen, S., Lücke, A., Mayr, C., Ohlendorf, C., Schäbitz, F., Schleser, G. H., Wille, M., Wulf, S., & Zolitschka, B. (2007). Lateglacial and Holocene wet—dry cycles in southern Patagonia: Chronology, sedimentology and geochemistry of a lacustrine record from Laguna Potrok Aike, Argentina. *The Holocene*, *17*(3), 297–310.

Hardie, L. A., Lowenstein, T., & Spencer, R. (1985). The problem of distinguishing between primary and secondary features in evaporites. *Sixth International Symposium on Salt*, 1, 11-39.

Heredia, J., Araguás-Araguás, L., & Ruiz, J.M. (2004). Use of Environmental Tracers to Characterize a Complex Hydrogeological System under Variable Density Conditions: A Case of the Subsurface Brine of Fuente de Piedra (SW Spain). *Cartagena,* 18, 679–692.

Heredia, J., García de Domingo, A., Ruiz, J. M., & Araguás-Araguás, L. (2010). Fuente de Piedra Lagoon (Málaga, Spain): A Deep Karstic Flow Discharge Point of a Regional Hydrogeological System. In B. Andreo, F. Carrasco, J. J. Durán, & J. W. LaMoreaux (Eds.), *Advances in Research in Karst Media* (pp. 231–236). Springer.

Höbig, N., Mediavilla, R., Gibert, L., Santisteban, J. I., Cendón, D. I., Ibáñez, J., & Reicherter, K. (2016). Palaeohydrological evolution and implications for palaeoclimate since the Late Glacial at Laguna de Fuente de Piedra, southern Spain. *Quaternary International*, *407*, 29–46.

Hodell, D. A., Channell, J. E. T., Curtis, J. H., Romero, O. E., & Röhl, U. (2008). Onset of "Hudson Strait" Heinrich events in the eastern North Atlantic at the end of the middle Pleistocene transition (~640 ka)? *Paleoceanography*, *23*(4).

Holland, H. D., & Zimmermann, H. (2000). The Dolomite Problem Revisited. *International Geology Review*, *42*(6), 481–490.

Jansen, B., Nierop, K. G. J., & Verstraten, J. M. (2003). Mobility of Fe(II), Fe(III) and Al in acidic forest soils mediated by dissolved organic matter: Influence of solution pH and metal/organic carbon ratios. *Geoderma*, *113*(3), 323–340.

Kim, J., Kimura, Y., Puchala, B., Yamazaki, T., Becker, U., & Sun, W. (2023). Dissolution enables dolomite crystal growth near ambient conditions. *Science*, *382*(6673), 915–920.

Kohfahl, C., Rodriguez, M., Fenk, C., Menz, C., Benavente, J., Hubberten, H., Meyer, H., Paul, L., Knappe, A., López-Geta, J. A., & Pekdeger, A. (2008). Characterising flow regime and interrelation between surface-water and ground-water in the Fuente de Piedra salt lake basin by means of stable isotopes, hydrogeochemical and hydraulic data. *Journal of Hydrology*, *351*(1), 170–187.

Kushnir, J. (1980). The coprecipitation of strontium, magnesium, sodium, potassium and chloride ions with gypsum. An experimental study. *Geochimica et Cosmochimica Acta*, *44*(10), 1471–1482.

Land, L. S. (1967). Diagenesis of skeletal carbonates. *Journal of Sedimentary Research*, *37*(3), 914–930.

Land, L. S. (1998). Failure to Precipitate Dolomite at 25 °C fromDilute Solution Despite 1000-Fold Oversaturation after32 Years. *Aquatic Geochemistry*, *4*(3), 361–368.

Last, W. M. (1990). Lacustrine dolomite—An overview of modern, Holocene, and Pleistocene occurrences. *Earth-Science Reviews*, *27*(3), 221–263.

Li, J., Li, M., Fang, X., Wang, Z., Zhang, W., & Yang, Y. (2017). Variation of gypsum morphology along deep core SG-1, western Qaidam Basin (northeastern Tibetan Plateau) and its implication to depositional environments. *Quaternary International*, *430*, 71–81.

Li, M., Wignall, P. B., Dai, X., Hu, M., & Song, H. (2021). Phanerozoic variation in dolomite abundance linked to oceanic anoxia. *Geology*, *49*(6), 698–702.

Lindtke, J., Ziegenbalg, S. B., Brunner, B., Rouchy, J. M., Pierre, C., & Peckmann, J. (2011). Authigenesis of native sulphur and dolomite in a lacustrine evaporitic setting (Hellín basin, Late Miocene, SE Spain). *Geological Magazine*, *148*(4), 655–669.

Lisiecki, L. E., & Raymo, M. E. (2005). A Pliocene-Pleistocene stack of 57 globally distributed benthic δ18O records. *Paleoceanography*, *20*(1).

Lougheed, B. C., & Obrochta, S. P. (2019). A Rapid, Deterministic Age-Depth Modeling Routine for Geological Sequences With Inherent Depth Uncertainty. *Paleoceanography and Paleoclimatology*, *34*(1), 122–133.

Lyons, T. W., & Severmann, S. (2006). A critical look at iron paleoredox proxies: New insights from modern euxinic marine basins. *Geochimica et Cosmochimica Acta*, *70*(23), 5698–5722.

Magee, J. W. (1991). Late quaternary lacustrine, groundwater, aeolian and pedogenic gypsum in the Prungle Lakes, southeastern Australia. *Palaeogeography, Palaeoclimatology, Palaeoecology*, *84*(1), 3–42.

Martrat, B., Grimalt, J. O., Lopez-Martinez, C., Cacho, I., Sierro, F. J., Flores, J. A., Zahn, R., Canals, M., Curtis, J. H., & Hodell, D. A. (2004). Abrupt Temperature Changes in the Western Mediterranean over the Past 250,000 Years. *Science*, *306*(5702), 1762–1765.

Mawson, D. (1929). Some South Australian Algal Limestones In Process of Formation. *Quarterly Journal of the Geological Society of London*, *85*(1–4), 613–620.

McKenzie, J. A., & Vasconcelos, C. (2009). Dolomite Mountains and the origin of the dolomite rock of which they mainly consist: Historical developments and new perspectives. *Sedimentology*, *56*(1), 205–219.

McMahon, S., van Smeerdijk Hood, A., & McIlroy, D. (2017). The origin and occurrence of subaqueous sedimentary cracks. *Geological Society, London, Special Publications*, *448*(1), 285–309.

Medlin, W. L. (1959). The preparation of synthetic dolomite. *American Mineralogist*, *44*(9–10), 979–986.

Mees, F., Casteñeda, C., Herrero, J., & Van Ranst, E. (2012). The Nature and Significance of Variations In Gypsum Crystal Morphology In Dry Lake Basins. *Journal of Sedimentary Research*, *82*(1), 37–52.

Miao, Z., Zhang, K., Zhang, P., Zhang, Q., Liu, H., Liu, N., Zhang, S., Teng, J., Li, B., Fang, Z., Yu, J., & Yu, J. (2023). Multiple proxies demonstrate the mechanism of dolomitization variations during global warming periods. *Geosystems and Geoenvironment*, *2*(4), 100187.

Morford, J. L., & Emerson, S. (1999). The geochemistry of redox sensitive trace metals in sediments. *Geochimica et Cosmochimica Acta*, *63*(11), 1735–1750.

Mukaka, M. M. (2012). Statistics corner: A guide to appropriate use of correlation coefficient in medical research. *Malawi Medical Journal: The Journal of Medical Association of Malawi*, *24*(3), 69–71.

Nascimento, G. S., Eglinton, T. I., Haghipour, N., Albuquerque, A. L., Bahniuk, A., McKenzie, J. A., & Vasconcelos, C. (2019). Oceanographic and sedimentological influences on carbonate geochemistry and mineralogy in hypersaline coastal lagoons, Rio de Janeiro state, Brazil. *Limnology and Oceanography*, *64*(6), 2605–2620.

Ortí, F., Gündogan, I., & Helvaci, C. (2002). Sodium sulphate deposits of Neogene age: The Kirmir Formation, Beypazari Basin, Turkey. *Sedimentary Geology*, *146*(3), 305–333.

Ortí, F., Rosell, L., & Anadón, P. (2010). Diagenetic gypsum related to sulfur deposits in evaporites (Libros Gypsum, Miocene, NE Spain). *Sedimentary Geology*, *228*(3), 304–318.

Ortí, F., Rosell, L., Gibert, L., Moragas, M., Playà, E., Inglès, M., Rouchy, J. M., Calvo, J. P., & Gimeno, D. (2014a). Evaporite sedimentation in a tectonically active basin: The lacustrine Las Minas Gypsum unit (Late Tortonian, SE Spain). *Sedimentary Geology*, *311*, 17–42.

Ortí, F., Pérez-López, A., García-Veigas, J., Rosell, L., Cendón, D. I., & Pérez-Valera, F. (2014b). Sulfate isotope compositions ($\delta^{34}S$, $\delta^{18}O$) and strontium isotopic ratios (87Sr/86Sr) of Triassic evaporites in the Betic Cordillera (SE Spain). *Revista de la Sociedad Geológica de España 27* (1), 79–89.

Ortí, F., Pérez-López, A., Pérez-Valera, F., & Benedicto, C. (2022). Isotope composition (δ34S, δ18O) of the Middle Triassic-Early Jurassic sulfates in eastern Iberia. *Sedimentary Geology*, *431*, 106104.

Pasquier, V., Sansjofre, P., Rabineau, M., Revillon, S., Houghton, J., & Fike, D. A. (2017). Pyrite sulfur isotopes reveal glacial–interglacial environmental changes. *Proceedings of the National Academy of Sciences*, *114*(23), 5941–5945.

Pedrera, A., Martos-Rosillo, S., Galindo-Zaldívar, J., Rodríguez-Rodríguez, M., Benavente, J., Martín-Rodríguez, J. F., & Zúñiga-López, M. I. (2016). Unravelling aquifer-wetland interaction using CSAMT and gravity methods: The Mollina-Camorra aquifer and the Fuente de Piedra playa-lake, southern Spain. *Journal of Applied Geophysics*, *129*, 17–27.

Pellerin, A., Antler, G., Marietou, A., Turchyn, A. V., & Jørgensen, B. B. (2020). The effect of temperature on sulfur and oxygen isotope fractionation by sulfate reducing bacteria (Desulfococcus multivorans). *FEMS Microbiology Letters*, *367*(9), fnaa061.

Pepiol-Salom, E., Batlle-Sales, J., & Bordás-Valls, V. (1999). Geostatistic study of salt distribution in "laguna de Salinas". Alicante. Spain. In J. Gómez-Hernández, A. Soares, & R. Froidevaux (Eds.), *geoENV II — Geostatistics for Environmental Applications* (pp. 441–452). Springer Netherlands.

Petrash, D. A., Gingras, M. K., Lalonde, S. V., Orange, F., Pecoits, E., & Konhauser, K. O. (2012). Dynamic controls on accretion and lithification of modern gypsum-dominated thrombolites, Los Roques, Venezuela. *Sedimentary Geology*, *245–246*, 29–47.

Petrash, D. A., Bialik, O. M., Bontognali, T. R. R., Vasconcelos, C., Roberts, J. A., McKenzie, J. A., & Konhauser, K. O. (2017). Microbially catalyzed dolomite formation: From near-surface to burial. *Earth-Science Reviews*, *171*, 558–582.

Poch, R. M., Artieda, O., & Lebedeva, M. (2018). Chapter 10—Gypsic Features. In G. Stoops, V. Marcelino, & F. Mees (Eds.), *Interpretation of Micromorphological Features of Soils and Regoliths (Second Edition)* (pp. 259–287). Elsevier.

Rodríguez-Rodríguez, M., Benavente Herrera, J., & Moral Martos, F. (2005). High Density Groundwater Flow, Major-ion Chemistry and Field Experiments in a Closed Basin: Fuente de Piedra Playa Lake (Spain). *American Journal of Environmental Sciences*, *1*(2), 164–171.

Rodríguez-Rodríguez, M., Martos-Rosillo, S., & Pedrera, A. (2016). Hydrogeological behaviour of the Fuente-de-Piedra playa lake and tectonic origin of its basin (Malaga, southern Spain). *Journal of Hydrology*, *543*, 462–476.

Rosell, L., Orti, F., Kasprzyk, A., Playa, E., & Peryt, T. M. (1998). Strontium Geochemistry of Miocene Primary Gypsum: Messinian of Southeastern Spain and Sicily and Badenian of Poland. *Journal of Sedimentary Research*, *68*(1).

Rothwell, R. G., & Croudace, I. w. (2015). Twenty Years of XRF Core Scanning Marine Sediments: What Do Geochemical Proxies Tell Us? In I. W. Croudace & R. G. Rothwell (Eds.), *Micro-XRF Studies of Sediment Cores: Applications of a non-destructive tool for the environmental sciences* (pp. 25–102). Springer Netherlands.

Sánchez-Román, M., Vasconcelos, C., Schmid, T., Dittrich, M., McKenzie, J. A., Zenobi, R., & Rivadeneyra, M. A. (2008). Aerobic microbial dolomite at the nanometer scale: Implications for the geologic record. *Geology*, *36*(11), 879–882.

Sánchez-Román, M., Vasconcelos, C., Warthmann, R., Rivadeneyra, M., & McKenzie, J. A. (2009). Microbial Dolomite Precipitation under Aerobic Conditions: Results from Brejo do Espinho Lagoon (Brazil) and Culture Experiments. In *Perspectives in Carbonate Geology* (pp. 167–178). John Wiley & Sons, Ltd.

Schmoker, J. W., Krystinik, K. B., & Halley, R. B. (1985). Selected Characteristics of Limestone and Dolomite Reservoirs in the United States. *AAPG Bulletin*, *69*(5), 733–741.

Sherwood, J. e., Stagnitti, F., Kokkinn, M. J., & Williams, W. D. (1991). Dissolved oxygen concentrations in hypersaline waters. *Limnology and Oceanography*, *36*(2), 235–250.

Sibley, D. F., Nordeng, S. H., & Borkowski, M. L. (1994). Dolomitization kinetics of hydrothermal bombs and natural settings. *Journal of Sedimentary Research*, *64*(3a), 630–637.

Sim, M. S., Bosak, T., & Ono, S. (2011). Large Sulfur Isotope Fractionation Does Not Require Disproportionation. *Science*, *333*(6038), 74–77.

Sonnenfeld, P., Hudec, P. P., Turek, A., & Boon, J. A. (1977). Base-Metal Concentration in a Density-Stratified Evaporite Pan. In J. H. Fisher, *Reefs and Evaporites—Concepts and Depositional Models* (pp. 181–187). American Association of Petroleum Geologists.

Spofforth, D. J. A., Pälike, H., & Green, D. (2008). Paleogene record of elemental concentrations in sediments from the Arctic Ocean obtained by XRF analyses. *Paleoceanography*, *23*(1).

van Lith, Y., Vasconcelos, C., Warthmann, R., Martins, J. C. F., & McKenzie, J. A. (2002). Bacterial sulfate reduction and salinity: Two controls on dolomite precipitation in Lagoa Vermelha and Brejo do Espinho (Brazil). *Hydrobiologia*, *485*(1), 35–49.

Van Tuyl, F. M. (1916). The Origin of Dolomite. *Iowa Geological Survey Annual Report*, *25*(1), 251–422.

Vasconcelos, C. (1994). *Modern dolomite precipitation and diagenesis in a coastal mixed water system, (Lagoa Vermelha, Brazil): A microbial model for dolomite formation under anoxic conditions* [Doctoral Thesis, ETH Zurich].

Vasconcelos, C., McKenzie, J. A., Bernasconi, S., Grujic, D., & Tiens, A. J. (1995). Microbial mediation as a possible mechanism for natural dolomite formation at low temperatures. *Nature*, *377*(6546), Article 6546.

Vasconcelos, C., & McKenzie, J. A. (1997). Microbial mediation of modern dolomite precipitation and diagenesis under anoxic conditions (Lagoa Vermelha, Rio de Janeiro, Brazil). *Journal of Sedimentary Research*, *67*(3), 378–390.

Vasconcelos, C., Warthmann, R., McKenzie, J. A., Visscher, P. T., Bittermann, A. G., & van Lith, Y. (2006). Lithifying microbial mats in Lagoa Vermelha, Brazil: Modern Precambrian relics? *Sedimentary Geology*, *185*(3), 175–183.

Wang, X. (2021). Equilibrium between dolomitization and dedolomitization of a global set of surface water samples: A new theoretical insight on the dolomite inorganic formation mechanism. *Marine Chemistry*, *235*, 104017.

Wankel, S. D., Bradley, A. S., Eldridge, D. L., & Johnston, D. T. (2014). Determination and application of the equilibrium oxygen isotope effect between water and sulfite. *Geochimica et Cosmochimica Acta*, *125*, 694–711.

Warren, J. K. (1991). Chapter 2 Sulfate Dominated Sea-Marginal and Platform Evaporative Settings: Sabkhas and Salinas, Mudflats and Salterns. In J. L. Melvin (Ed.), *Developments in Sedimentology* (Vol. 50, pp. 69–187). Elsevier.

Warren, J. K. (2000). Dolomite: Occurrence, evolution and economically important associations. *Earth-Science Reviews*, *52*(1), 1–81.

Warren, J. K. (2016). *Evaporites: A Geological Compendium*. Springer International Publishing.

Warthmann, R., van Lith, Y., Vasconcelos, C., McKenzie, J. A., & Karpoff, A. M. (2000). Bacterially induced dolomite precipitation in anoxic culture experiments. *Geology*, *28*(12), 1091–1094.

Wright, D. T. (1999). The role of sulphate-reducing bacteria and cyanobacteria in dolomite formation in distal ephemeral lakes of the Coorong region, South Australia. *Sedimentary Geology*, *126*(1), 147–157.

Zaheri, M., & Rafiei, B. (2019). Facies analysis, petrography and geochemistry of the Neogene gypsum deposits in the Eshtehard area, Alborz Province, Iran. *Geopersia*, *Online First*.

Ziegler, M., Jilbert, T., de Lange, G. J., Lourens, L. J., & Reichart, G.-J. (2008). Bromine counts from XRF scanning as an estimate of the marine organic carbon content of sediment cores. *Geochemistry, Geophysics, Geosystems*, *9*(5).